

In compliance with the
Canadian Privacy Legislation
some supporting forms
may have been removed from
this dissertation.

While these forms may be included
in the document page count,
their removal does not represent
any loss of content from the dissertation.

**VERIFICATION OF IMRT BEAM DELIVERY
WITH A FERROUS SULFATE GEL DOSIMETER AND MRI**

by

MARYLÈNE BRODEUR

Medical Physics Unit
McGill University, Montreal

February 2003

A thesis submitted to the
Faculty of Graduate Studies and Research
in partial fulfilment of the requirements
of the degree of Master of Science



National Library
of Canada

Bibliothèque nationale
du Canada

Acquisitions and
Bibliographic Services

Acquisitons et
services bibliographiques

395 Wellington Street
Ottawa ON K1A 0N4
Canada

395, rue Wellington
Ottawa ON K1A 0N4
Canada

Your file *Votre référence*

ISBN: 0-612-88166-0

Our file *Notre référence*

ISBN: 0-612-88166-0

The author has granted a non-exclusive licence allowing the National Library of Canada to reproduce, loan, distribute or sell copies of this thesis in microform, paper or electronic formats.

L'auteur a accordé une licence non exclusive permettant à la Bibliothèque nationale du Canada de reproduire, prêter, distribuer ou vendre des copies de cette thèse sous la forme de microfiche/film, de reproduction sur papier ou sur format électronique.

The author retains ownership of the copyright in this thesis. Neither the thesis nor substantial extracts from it may be printed or otherwise reproduced without the author's permission.

L'auteur conserve la propriété du droit d'auteur qui protège cette thèse. Ni la thèse ni des extraits substantiels de celle-ci ne doivent être imprimés ou autrement reproduits sans son autorisation.

Canada

Abstract

Intensity modulated photon beam radiation therapy often results in dynamically delivered beams with small field sizes and steep dose gradients. This defines a need for an integrating, tissue-equivalent, high resolution dosimeter. 3D ferrous sulfate gel based dosimetry involves the use of magnetic resonance (MR) images of radiosensitive paramagnetic gels. The goal of this work is to create a patient specific quality assurance (QA) procedure that links measured dosimetric information to clinical goals.

The gel dosimeter system is tested through a set of simple experiments which characterize and confirm the system as a valid QA tool for conformal and intensity modulated radiation therapy.

For this work, dynamic photon beams are created on a commercially available inverse treatment planning system and the treatment is delivered to a gel filled acrylic mold. Software has been developed to quantify dose from the QA MR images, and to register this information to the planning computed tomography (CT) scan. The software displays the measured dose on the planning CT, and calculates dose-volume histograms for the registered measured data and contoured patient structures. This work reveals good agreement between planned and measured dose distributions, with less than 5% difference in the mean doses of the contoured patient structures.

Résumé

La radiothérapie par modulation d'intensité (IMRT) implique souvent des petits champs avec d'importants gradients de dose. Ceci définit le besoin d'un dosimètre à haute résolution, intégrateur et tissu équivalent. La lecture par résonance magnétique du gel dosimétrique à base de sulfate ferreux, qui est radiosensible et paramagnétique, permet une dosimétrie en 3D. Le but de ce travail est de créer une procédure d'assurance qualité (QA) spécifique au patient, afin de relier l'information dosimétrique mesurée aux buts cliniques.

Une série d'expériences simples permettent de caractériser le gel dosimétrique et de confirmer sa validité en tant qu'outil d'assurance qualité pour la radiothérapie conforme et la radiothérapie par modulation d'intensité.

Des champs dynamiques sont créés par un système commercialisé de planification inverse et le traitement est administré au gel contenu dans un moule en acrylique. Un logiciel a été développé afin de recalculer les images de résonance magnétique du QA aux images tomographiques (CT) de planification. Le logiciel affiche la dose mesurée sur le CT de planification et calcule les histogrammes dose-volume pour la dose mesurée et les structures segmentées (contours) du patient. Ce travail révèle une bonne concordance entre les distributions de dose planifiées et mesurées, avec moins de 5% d'écart pour les doses moyennes des structures segmentées.

Acknowledgements

The research for this thesis was performed under the auspices of the Medical Physics Unit of McGill University, at the Departments of Medical Physics, Radiation Oncology, and Diagnostic Radiology of the McGill University Health Center, at the Montreal General Hospital. I am grateful to the Centre Hospitalier de Trois-Rivières for providing funding for this research.

I would like to thank my research supervisor William Parker for his guidance and patience during the course of my studies. His humour, good nature and encouragement assured me a pleasant stay at McGill. I am also very grateful to Dr. Ervin Podgorsak for his patience, support and timely encouragements throughout the long and sinuous road towards my M.Sc. degree.

The completion of this thesis would not have been possible without invaluable discussions with Dr. Yanic Bercier, Philippe Bélanger, Dr. François DeBlois, Dr. Jan Seuntjens, Dr. Dimitre Hristov, Michael Evans and Joe Larkin, all of whom I thank for sharing their technical expertise. I would like to thank Dr. Joseph Hornak, for granting me permission to use some of his MRI figures. I would also like to thank Dr. Wieslaw Wierzbicki, Jean-René Tremblay, Louis Surprenant and the rest of the radiation oncology team at the Hôpital Maisonneuve-Rosemont for their help with certain aspects of the project and for so warmly welcoming me as a new colleague. Additionally, a special thank you goes to my classmates, especially Marie-Laure Camborde, Peter Petric, Deborah Hodefi and Kamen Paskalev for their help, support, encouragement and friendship. Last but not least, of course, I must thank my parents, Joan and Michel, my sister Marie-Chantal, my grandmother Nana and my good friends Julie and Félix for motivating me and providing me with the inspiration to pursue my dreams.

Table of Contents

ABSTRACT	I
RÉSUMÉ.....	II
ACKNOWLEDGEMENTS.....	III
TABLE OF CONTENTS.....	IV
LIST OF FIGURES	VII
LIST OF TABLES	X
PREFACE	XI
1 INTRODUCTION.....	1
1.1 IMAGING OF DOSE DISTRIBUTIONS USING GEL DOSIMETRY AND MRI	1
1.1.1 <i>Development of ferrous sulphate gel dosimetry</i>	2
1.1.2 <i>Applications of the Fricke-gel dosimeter</i>	6
1.2 TREATMENT PLANNING IN RADIATION THERAPY	8
1.2.1 <i>Intensity modulated radiation therapy (IMRT)</i>	11
1.2.2 <i>Inverse treatment planning</i>	11
1.2.3 <i>Dosimetry and quality assurance for IMRT</i>	13
1.3 GOALS OF THIS THESIS.....	14
2 THE FRICKE-GEL DOSIMETER.....	15
2.1 CHEMICAL DOSIMETRY.....	15
2.2 THE FRICKE SOLUTION DOSIMETER	16
2.3 THE FRICKE-GEL DOSIMETER	16
2.4 RADIATION CHEMISTRY OF THE FRICKE-GEL DOSIMETER	17
2.4.1 <i>The initiation stage</i>	17
2.4.2 <i>The propagation stage</i>	18
2.4.3 <i>The termination stage</i>	18
2.5 GENERAL CHARACTERISTICS OF THE FRICKE-GEL DOSIMETER	21
2.5.1 <i>Absoluteness</i>	21
2.5.2 <i>Precision and Accuracy</i>	21

2.5.3	<i>Dose sensitivity, range and saturation</i>	22
2.5.4	<i>Irradiation configuration factors</i>	23
2.5.5	<i>Stability</i>	23
3	MAGNETIC RESONANCE IMAGING	24
3.1	DEVELOPMENT OF MAGNETIC RESONANCE IMAGING	24
3.2	BASIC NUCLEAR MAGNETIC RESONANCE	25
3.2.1	<i>Nuclear spin</i>	25
3.2.2	<i>Net magnetization and Larmor precession</i>	26
3.2.3	<i>Excitation pulses and magnetization recovery</i>	27
3.2.4	<i>Relaxation</i>	29
3.2.5	<i>Pulse sequence in MRI</i>	31
3.3	MAGNETIC RESONANCE IMAGING	34
3.3.1	<i>2D Image acquisition and reconstruction</i>	34
3.3.2	<i>Multislice spin echo imaging</i>	36
3.3.3	<i>Fast spin echo imaging</i>	37
3.3.4	<i>Weighted images (proton density, T_1, T_2)</i>	38
3.3.5	<i>Two-point-ratio calculation of T_1 relaxation time</i>	39
3.3.6	<i>Noise and the signal-to-noise ratio (SNR)</i>	40
3.4	MRI INSTRUMENTATION	41
3.4.1	<i>Magnet</i>	41
3.4.2	<i>Magnetic-field gradient coils</i>	42
3.4.3	<i>Radiofrequency system</i>	42
3.4.4	<i>Transmit and receiver coils</i>	43
3.4.5	<i>Computer system</i>	43
4	METHODS AND MATERIALS	44
4.1	GENERAL EXPERIMENTAL PROCEDURES	44
4.1.1	<i>Preparation of the gel</i>	44
4.1.2	<i>Selection of phantoms</i>	45
4.1.3	<i>CT imaging and treatment planning</i>	46
4.1.4	<i>Linac irradiation</i>	47

4.1.5	<i>MR scanning</i>	48
4.1.6	<i>Data analysis and relative dose distributions</i>	49
4.1.7	<i>Registration and fusion</i>	50
4.1.8	<i>Dose-volume histograms</i>	50
4.2	EXPERIMENTS.....	50
4.2.1	<i>Vials</i>	50
4.2.2	<i>Open and wedged beam PDDs and profiles</i>	52
4.2.3	<i>Forward-planned box phantom</i>	52
4.2.4	<i>Forward-planned head phantom</i>	54
4.2.5	<i>Helios IMRT inverse-planned head phantom</i>	56
4.2.6	<i>Corvus IMRT inverse-planned head phantom</i>	56
5	RESULTS AND DISCUSSION	59
5.1	VALIDATION OF THE GEL DOSIMETER.....	59
5.1.1	<i>Characteristics of the gel dosimeter</i>	59
5.1.2	<i>Percent depth doses and profiles</i>	63
5.2	3D DOSE DISTRIBUTIONS AND DOSE VOLUME HISTOGRAMS.....	67
5.2.1	<i>Forward-planned box phantom</i>	67
5.2.2	<i>Forward-planned head phantom</i>	75
5.2.3	<i>Helios IMRT inverse-planned head phantom</i>	84
5.2.4	<i>Corvus IMRT inverse-planned head phantom</i>	91
6	CONCLUSIONS	97
	REFERENCES	102

List of Figures

Figure 1.1: BEV and DRR of the anterior field of a lung tumor case.	10
Figure 2.1: Initiation stage.	18
Figure 2.2: Propagation stage (1 st mechanism).	19
Figure 2.3: Propagation stage (2 nd mechanism).	19
Figure 2.4: Termination stage (main mechanism).	20
Figure 2.5: Termination stage (minor mechanism).	20
Figure 3.1: Nucleus precessing around magnetic field B_0	27
Figure 3.2: M_{xy} decay and M_z recovery after excitation.	28
Figure 3.3: Free induction decay (FID) in the space, time and frequency domains.	30
Figure 3.4: Longitudinal relaxation.	31
Figure 3.5: Transverse relaxation.	32
Figure 3.6: Saturation recovery sequence.	32
Figure 3.7: Spin echo sequence.	34
Figure 3.8: Slice selection by a magnetic field gradient.	35
Figure 3.9: k -space and corresponding axial MR image of brain.	37
Figure 3.10: Fast spin-echo sequence with four echoes and corresponding k -space.	38
Figure 3.11: Calculated signal vs. dose curves for various imaging parameters.	40
Figure 3.12: GE Signa MRI scanner with 1.5 T field.	42
Figure 3.13: MRI head coil with birdcage geometry.	43
Figure 4.1: Vials, box phantom and head phantom.	46
Figure 4.2: Linac setup of box phantom.	48
Figure 4.3: Diagram showing the irradiation setup of the vials.	51
Figure 4.4: Diagram showing the irradiation setup for the PDDs and profiles.	53
Figure 4.5: 3D treatment plan for the forward-planned box phantom.	54
Figure 4.6: Head phantom CT and user-defined planning contours.	55
Figure 4.7: 3D treatment plan for the forward-planned head phantom.	55
Figure 4.8: 3D treatment plan for the Helios IMRT inverse-planned head phantom.	57

Figure 4.9: Corvus BEV of anterior field with insert showing all field directions (yellow) in axial plane.	58
Figure 5.1: Raw MR images of the irradiated vials.	60
Figure 5.2: Calculated R_1 images of the irradiated vials.	60
Figure 5.3: Raw MR signal intensity and R_1 values as a function of dose.	61
Figure 5.4: Central axis R_1 images of the 10x10 cm ² open and 60° wedged beams.	63
Figure 5.5: Percent Depth Dose (PDD) graph of a 10x10 cm ² open beam.	64
Figure 5.6: Percent Depth Dose (PDD) graph of a 60° wedge 10x10 cm ² beam.	64
Figure 5.7: Profiles at 1.5 cm and 9.5 cm of the open beam.	66
Figure 5.8: Profiles at 1.5 cm and 9.5 cm for the 60° wedge beam.	66
Figure 5.9: Forward-planned box phantom contours on TPS dose at isocenter.	68
Figure 5.10: Forward-planned box phantom contours on gel dose at isocenter.	69
Figure 5.11: Forward-planned box phantom TPS isodoses on CT and contours.	70
Figure 5.12: Forward-planned box phantom gel isodoses on CT and contours.	70
Figure 5.13: Percentage dose difference map at the isocenter of the box phantom.	71
Figure 5.14: Mid-coronal slice showing misalignment of the box in the z-axis.	72
Figure 5.15: Forward-planned box phantom cumulative DVHs.	75
Figure 5.16: Forward-planned box phantom differential DVHs.	76
Figure 5.17: Image fusion verification for forward-planned head phantom.	77
Figure 5.18: Forward-planned head phantom contours on TPS dose at isocenter.	78
Figure 5.19: Forward-planned head phantom contours on gel dose at isocenter.	78
Figure 5.20: Forward-planned head phantom TPS isodoses on CT and contours.	79
Figure 5.21: Forward-planned head phantom gel isodoses on CT and contours.	79
Figure 5.22: Percentage dose difference map at the isocenter of the head phantom.	80
Figure 5.23: Forward-planned head phantom cumulative DVHs.	82
Figure 5.24: Forward-planned head phantom differential DVHs.	83
Figure 5.25: Helios IMRT contours superimposed over the TPS dose at isocenter.	84
Figure 5.26: Helios IMRT contours superimposed over the gel dose at isocenter.	85
Figure 5.27: Helios IMRT percentage dose difference map at the isocenter.	85
Figure 5.28: Sagittal views of (a) TPS and (b) gel dose distributions.	86
Figure 5.29: Helios IMRT TPS isodoses superimposed on CT and contours.	87

Figure 5.30: Helios IMRT gel isodoses superimposed on CT and contours.....87
Figure 5.31: Helios IMRT inverse-planned head phantom cumulative DVHs.....89
Figure 5.32: Helios IMRT inverse-planned head phantom differential DVHs.....90
Figure 5.33: Axial image of Corvus IMRT inverse-planned head phantom.....91
Figure 5.34: Sagittal image of Corvus IMRT inverse-planned head phantom.92
Figure 5.35: Corvus IMRT planning contours and gel dose on CT at the isocenter.....93
Figure 5.36: (a) MR isodoses and (b) Corvus isodoses on CT image with contours.....94
Figure 5.37: Corvus IMRT inverse-planned head phantom cumulative DVHs.....96
Figure 5.38: Corvus IMRT inverse-planned head phantom differential DVHs.....96

List of Tables

Table 4.1: Radiological properties of water, Fricke-gel and PMMA.	45
Table 4.2: Gel dosimeter MRI scanning parameters.	49
Table 4.3: Forward-planned box phantom treatment parameters.	53
Table 4.4: Forward-planned head phantom treatment parameters.	55
Table 4.5: Helios IMRT inverse-planned head phantom treatment parameters.	56
Table 4.6: Corvus IMRT inverse-planned head phantom treatment parameters.	58
Table 5.1: Raw MR signal, R_1 and measured dose for various irradiation doses.	61
Table 5.2: MR statistics and gel dosimeter characteristics at 0 and 20 Gy.	62
Table 5.3: Statistics of the open and wedged beam PDDs.	65
Table 5.4: Statistics of the open and wedged beam profiles.	67
Table 5.5: Forward-planned box phantom contour statistics.	73
Table 5.6: Number of pixels and volume of each contour in the box phantom.	74
Table 5.7: Forward-planned head phantom statistics.	81
Table 5.8: Helios IMRT inverse-planned head phantom statistics.	88
Table 5.9: Corvus IMRT inverse-planned head phantom statistics.	95

Preface

Cancer is the leading cause of premature death in Canada. According to the National Cancer Institute of Canada¹, an estimated 136 900 new cases of cancer will be diagnosed in 2002 and 66 200 deaths will result from this disease. Based on current incidence rates, it is estimated that 38% of women and 41% of men will develop cancer during their lifetimes, while the lifetime probability of dying from cancer is 23% for women and 27% for men. The main treatment modalities for cancer patients are surgery, radiation therapy and chemotherapy. In Canada, approximately 50% of those diagnosed with cancer are offered radiation therapy, alone, or in combination with another modality.

Radiation therapy generally aims to obtain local control of the disease by delivering a precise dose of ionizing radiation to the tumor. Conventional radiation therapy relies on the use of diagnostic quality X-ray (simulation) films of the patient's anatomy for the creation of a treatment plan. Generally, these films depict only bony anatomy, and therefore the localisation of disease by this method is imprecise, leading to large treatment margins and irradiation of healthy tissues. Conformal therapy, made possible by improvements in treatment planning and delivery, also tries to minimize the damage to the surrounding healthy tissue by shaping the radiation beams. The goal of intensity modulated radiation therapy (IMRT) is to deliver a uniform dose to the tumor with tight margins around the target, in order to increase local control of the disease while reducing secondary effects. The intensity modulations of the IMRT beams are obtained by the superposition of a large number of small fields. Validating the dosimetry of these numerous small beams with steep dose gradients requires an integrating, tissue-equivalent, high resolution, and anthropomorphic dosimeter. The use of a ferrous sulphate gel dosimeter in a patient specific quality assurance procedure resolves these issues.

The major goal of this thesis is to demonstrate the use of a ferrous sulphate gelatin dosimeter in the quality assurance of intensity modulated radiation therapy. For this, dose-volume histograms (DVH) obtained from the dose distribution measured in the gel

dosimeter will be compared to the DVHs calculated by a commercially available treatment planning system. This thesis also provides a general overview of the use of gel-based ferrous sulphate dosimeters for the MR imaging of 3D dose distributions. Chapter 1 contains a literature review in the field of dose distribution imaging using gel dosimetry and MRI, and a review of treatment planning in radiation therapy, focusing on intensity modulated radiation therapy (IMRT) and inverse treatment planning. Chapter 2 presents radiation chemistry and general characteristics of the Fricke-gel dosimeter. Magnetic resonance imaging is reviewed in Chapter 3, which covers the basic theory, techniques for the measurements of relaxation parameters and MRI instrumentation. Chapter 4 covers the methods and materials used in the experiments throughout this thesis, describing the procedures from the extraction of dose information from MR images of irradiated gel phantoms to the production of measured dose-volume histograms. The results are presented and discussed in Chapter 5. First, general characteristics of the gel dosimeter are obtained and the gel dosimeter is compared with an ion chamber dosimeter. Four experiments are then used to illustrate the usefulness of the gel dosimeter in verifying 3D dose distributions. The first consists of a forward-planned box phantom to test the overall process leading to the production of the statistics and dose-volume histograms (DVH) for the 3D volume. The second forward-planned experiment more specifically validates the image fusion for the irregularly shaped head phantom. The third and fourth experiments involve inverse-planned IMRT dose distributions. The third plan has an annular shaped dose distribution and it tests the ability of the gel dosimeter to deal with irregularly shaped steep dose gradients. The last experiment simulates all steps required to validate an actual IMRT case, using a probable treatment plan and the Rando phantom as a mock patient. That chapter concludes with a discussion of dose discrepancies found in the buildup region and in the beam penumbra. The final chapter summarizes the results and discusses possibilities for future work in the field.

Chapter One

1 Introduction

This chapter will first review the literature pertaining to the ferrous sulphate gelatin dosimetry technique, also called Fricke-gel dosimetry. Intensity modulated radiation therapy and inverse treatment planning are then introduced to the reader, with emphasis on quality assurance. Finally, the aims and goals of this thesis will be explained in greater detail.

1.1 Imaging of dose distributions using gel dosimetry and MRI

In 1984, Gore *et al.*² were the first to venture in the field of gel dosimetry. The authors showed that the changes in irradiated Fricke solution, usually detected by spectrophotometry, could also be detected by nuclear magnetic resonance (NMR) when using a 20 MHz NMR spectrometer. The ferric (Fe^{3+}) ions created by the irradiation of the ferrous (Fe^{2+}) ions in the Fricke solution caused a change in the relaxation properties of the solution. It was shown that the spin-lattice relaxation rate (R_1) of the irradiated dosimeter was linearly proportional to dose in the range of 2.5 to 41 Gray (Gy). Later that year³, the authors demonstrated that spatial dose distributions could also be preserved when the ions were locked in a gelatin matrix and the gel was imaged using an MRI scanner. Since then, many researchers have studied this technique and its applications.

1.1.1 Development of ferrous sulphate gel dosimetry

Olsson⁴ and his Swedish group (1989) presented a basic study of two Fricke gels, one using gelatin, and the other agarose. The authors showed that the dose response (R_1 vs. dose) of both gels was linear in the 0 to 40 Gy range and that they had a similar minimum detectable dose of about 1 Gy. In both cases, the sensitivity of the gel (slope of measured R_1 vs. dose) was greater than that of Fricke solution, two-fold greater for gelatin gel and four-fold greater for agarose. The dose-response of the gels was also found to be independent of dose-rate in the range used by radiation therapy accelerators. In 1990, Olsson⁵ went on to perform 3D dose distribution measurements of ^{60}Co beams, and linac produced photon and electron beams using the agarose based gel. Depth dose curves and profiles were shown to agree with diode measurements. The overall uncertainty, combining both the gel dosimeter and the MR imaging technique uncertainties, was initially estimated to be up to 20%.

A year later, Hazle *et al.*⁶ examined the characteristics of the Fricke-gel dosimeter. The authors irradiated vials to different doses (0 to 150 Gy) with different ferrous ion concentrations (0.1 to 2.0 mM). For all experiments, the dosimeter response was shown to be approximately linear in the 0 to 50 Gy range. The sensitivity of the dosimeter for the 0.5 to 2.0 mM concentrations was constant at $0.0423 \text{ s}^{-1}\text{Gy}^{-1}$. They also obtained a reproducibility (standard deviation of a large group of repetitive measurements) of 5% in the 20 to 50 Gy range and 10% in the 5 to 10 Gy dose range. The dose uncertainty estimates varied between 5%, for the 20 to 35 Gy range, and approximately 10% at 5 Gy. They concluded that their dosimetric system could determine absorbed doses in the 20 to 50 Gy range, with 5% accuracy.

A Yale University group⁷ led by Schulz also carried out such a study for the agarose gel. They showed the requirement for oxygen saturation (for maximum sensitivity) and also examined the effect of ferric ion diffusion on the dose distribution. The authors found that the agarose gel dosimeter offered the best results when it was saturated in oxygen, had a low pH and was irradiated and measured on the same day as preparation.

Keller⁸ studied the spontaneous oxidation and the effects of oxygen depletion in the Fricke-gel dosimeter. He found that the spin-lattice relaxation rate of the Fricke-gel decayed at a much faster rate than for the Fricke solution. For an irradiated gel, he found that the spontaneous oxidation occurrence decreased with increasing dose, as fewer ferrous ions are left in the gel, and that to minimize the effects of spontaneous oxidation, the gel should be imaged as soon as possible after irradiation. The author also showed that the dose dependent saturation of the gel, which starts at around 40 Gy and is complete at 130 Gy, is attributed to the depletion of oxygen in the system. Duzenli⁹ also showed that if the oxygen within the gelatin system is not uniformly distributed, the dose response throughout the phantom will be inhomogeneous. In particular, this effect is noticeable when a surface of the gel is exposed to air. Maryanski *et al.*¹⁰ noticed that plastic walls (e.g. Lucite®) were permeable to atmospheric oxygen.

Another effect that limits the experiment time is the diffusion of the ferric ions in the dosimeter gel. Olsson *et al.*¹¹ investigated this in 1992, using agarose gel. They measured the diffusion coefficient and studied how it distorted the MR images of the gel as time passed. The authors found that the diffusion was not significant when the imaging was completed within two hours of the start of the irradiation, but for cases with steep dose gradients, that time should be reduced. In some studies, the effect of chelating agents, such as xylenol orange, was examined and they showed a decrease in ferric ion diffusion¹², but also reduced the sensitivity of the gel.

In 1998, Bäck *et al.*¹³ presented their improvements on the MR-imaged gel dosimeter, dubbed FeMRI. They used an agarose gel in a large cylindrical phantom, an optimised MRI acquisition sequence, and subtracted the background (pre-irradiated image) from the irradiated image to remove magnetic field inhomogeneities which distort MR images. Depth dose curves and dose profiles obtained with the gel dosimeter were shown to agree with diode measurements for both a 10 MeV electron beam and a 5 MV photon beam. They found that the doses measured beyond shallow depths were within 2% of the doses obtained by a 3D water phantom scanning system using both a diode detector and a plane-parallel ionisation chamber. The authors also found a very good agreement (less than 1%) with Monte Carlo calculations for the electron beam measurements.

Chan and Ayyangar¹⁴ verified the water equivalence of FeMRI gels (agarose, gelatin and xylenol orange gel). They used the Integrated Tiger Series Monte Carlo codes (version 3.0, Sandia National Laboratories and National Institute of Standards and Technology). They showed that the depth dose curves, both on and off axis, the transverse profiles, and the photon and electron energy deposition were close to that in water. The doses calculated in gel were within 2% of those calculated in water. They concluded that the gels were water-equivalent for the usual radiation therapy photon energies (6 to 15 MV) and electron energies (5 to 20 MeV).

Kron *et al.*¹⁵ showed the soft tissue equivalence of the gels by calculating electron densities and effective atomic numbers and comparing them to actual CT data. The effective atomic number (Z_{eff}) of the Hazle⁶ gelatin gel was 7.56, while the relative electron density (ρ_e^w) was 1.004. The gelatin gel density at 24°C was reported to be 1.005 g/cm. Agarose gel was also found to be tissue-equivalent for a wide range of radiation energies (1.4 mm to 7.5 mm Al HVL photons, and 12 MeV electrons), making it interesting for the investigation of low energy radiation, such as superficial x-rays and brachytherapy sources.

The density of the Fricke-gel dosimeter can also be made similar to other anatomical tissues. By adding strontium to agarose gel, a bone-equivalent gel was produced by Kron¹⁵. Olberg¹⁶ on the other hand, whipped some gelatin gel into a foam to mimic lung tissue and placed it between slabs of regular soft-tissue-equivalent gel. Thin mylar films kept the gels separate. The Hounsfield number of this low-density gel (-600 HU) was comparable to normal human lung (-770 HU to -875 HU). The measured dose distribution was similar to that obtained by using other dosimeters with phantoms containing lung tissue.

The relationship between spin-spin relaxation rates ($1/T_2 = R_2$) and dose has been investigated by Duzenli *et al.*⁹. The authors found that the R_2 sensitivity was marginally higher than the R_1 sensitivity, and as the image acquisition time needed for R_2 is significantly longer than for R_1 , this increase in sensitivity may be counterbalanced by an increase in diffusion due to the longer imaging time.

Another method of obtaining dose information from MR images of gel dosimeters is the use of a calibration curve. Parker¹⁷ used six vials irradiated at known doses to create a calibration curve relating the dose to the MR intensity directly. Background images of the gel dosimeter were subtracted from the post-irradiation images and each pixel value was matched to a dose using the calibration curve. The vials were filled with Fricke-gel from the same batch as for the experiment phantom, and the vials were MR scanned in the same configuration as the gel dosimeter. Oldham¹⁸ used a different approach to improve calibration accuracy by matching a great number of points from a gel phantom percent depth dose curve (PDD) to the depth dose curve measured with an ion chamber.

Some of the work in the field has been carried out using polymer gels. In this case, the irradiation causes the polymerisation and cross-linking of acrylic monomers that are distributed in a gel matrix containing either agarose (BANANA gel, Maryanski¹⁹), or gelatin (BANG gel, Maryanski¹⁰). The main advantage of polymer gels is that the dose spatial distribution remains stable and can therefore be imaged long after irradiation. The irradiation also causes a visual change in the gel, where the irradiated portions become opaque. This allows for qualitative visual inspection of the irradiation field, and also for quantitative optical density measurements, in addition to MR measurements. The main drawback to the polymer gel is its complex preparation. The gel must be prepared and kept in a strict oxygen-free environment, even during irradiation, requiring elaborate equipment and the use of toxic chemicals. The dose response for polymer gels starts to saturate after 10 Gy¹⁸.

Two new types of Fricke gels with low diffusion rates were recently developed by Chu *et al.*²⁰. In addition to ferrous sulphate and sulphuric acid, they both contain 20% per weight polyvinyl alcohol (PVA) and xylene orange. Storing the newly prepared gel at -20°C for the gelation process leads to an opaque cryogel that may be read by MR. Since it is flexible and stable at room temperature, it can be used as a radiosensitive bolus that changes from orange to brown with irradiation. Storing the newly prepared gel at 5°C for the gelation process leads to a transparent hydrogel that can be read either by MR or by optical spectrophotometry.

1.1.2 Applications of the Fricke-gel dosimeter

MR-imaged ferrous sulphate gel dosimetry has been used to verify dose distribution calculations and beam parameters of simple irradiation configurations. In 1995, Bengtsson *et al.*²¹ used a Fricke-gel dosimeter to investigate dynamic wedge angles and beam profiles. The wedge angles (15°, 30°, 45° and 60°) agreed with film measurements and treatment planning calculations. The dose profile measurements were in good agreement with those made with a diode array. For large wedge angles, the gel dose at the field edge was about 5% lower than expected and this was attributed to diffusion and noise-filtering of the MRI data.

In 1998, Bäck *et al.*¹³ compared the dose distributions extracted from an agarose gel dosimeter to the dose distribution calculated by a commercially available treatment planning system (TPS). The authors examined simple beam configurations. The FeMRI and the TPS data agreed very well for the 10 MeV electron beam, with differences up to 3% at shallow depths, and 5% in the penumbra region. The authors explained this by the way the TPS deals with the lateral scatter of the electrons that are outside the primary beam. For a 5 MV photon beam, the FeMRI system was in good agreement with the TPS data, except in the build-up region (less than 4% difference), where the gel dosimeter seemed to measure a dose lower than the dose measured with other dosimetric systems.

The gel dosimeter has been shown to be a tissue-equivalent integrating dosimeter that can be molded to reproduce the shape of any body part. It was not long before researchers created gel phantoms to verify complex treatment plans and conformal radiation therapy. Guo *et al.*²² used an agarose gel dosimeter in 1995 to evaluate the accuracy of Gamma Knife radiosurgery. The cylindrical phantom was fixed to a stereotactic frame and irradiated to a maximum dose of 15 Gy, using 4 mm collimation. Using center of mass calculations, the radiation isocenter and the frame center were found to be within 0.12 mm and 0.43 mm in terms of physical distance in two trials, which is well within the mechanical accuracy of the Gamma Knife (0.5 mm).

In 1994, Parker¹⁷ studied dose distributions in multi-catheter brachytherapy using a high dose-rate ¹⁹²Ir source and Fricke-gel dosimetry. The dose distributions obtained via

calculated relaxation rates and also by a calibration curve, showed a good agreement with the expected dose distributions generated from a computerized treatment plan. FeMRI was also used by Knutsen *et al.*²³ to determine dose distributions in intracavitary brachytherapy of cervical cancer. Fricke-gel was poured around a cervix ring applicator. The dose distribution was delivered with a high dose-rate ¹⁹²Ir remote afterloader, using clinical treatment parameters. The accuracy of the gel was found to be the same as for TLDs. Isodoses curves from the gel agreed with those of the treatment planning within ± 2 mm and were superimposed on MR images of the actual patient. More recently, McJury *et al.*²⁴ used a polyacrylamide gel dosimeter to measure the dose distribution around a high dose-rate ¹⁹²Ir source.

In 1995, Chan and Ayyangar²⁵ used a head phantom to verify 3D conformal radiotherapy. The human skull covered with wax was filled with Fricke-gel and the spherical target volume defined within was irradiated with five non-coplanar photon beams delivering 25 Gy to the target. Relative dose values were extracted from the 7 mm thick MRI slices. The maximum difference in dose between the gel and the treatment planning system was 5.1%. A comparison of the cumulative dose area histograms for the planned target showed a good agreement, and they attributed the discrepancies to positional uncertainty.

In 1997, Johansson *et al.*²⁶ used pixel-by-pixel comparison and dose area histograms to compare dose distributions measured by agarose gel dosimetry to the treatment planning system calculated distributions. This was done for a breast cancer treatment and a urinary bladder cancer treatment. A combination of photons and electrons was used in the first case and one dorsal and two lateral isocentric photon beams were used in the second. A single 15 mm thick slice was acquired with the MR, and R_1 images were calculated using a two-point evaluation technique and the background subtraction method. An image of the planned dose distribution minus the gel dose distribution showed the deviation, which was on average 0.6% for the bladder case, but went up to 4% in the breast cancer case, due to increased uncertainty in beam abutment regions. The authors estimated the precision of the technique to be about 1.5%.

With the advent of 3D CT based conformal radiotherapy and IMRT, unique problems exist for dosimetry measurements and quality assurance (QA). The next section discusses the evolution of treatment planning in radiotherapy and some modern QA issues.

1.2 Treatment planning in radiation therapy

In modern radiation therapy, treatments are planned to deliver a uniform dose across the diseased tissue while minimizing the dose to the healthy tissue²⁷. In fact, most dose prescriptions are limited by the tolerance doses of critical structures near the target.

At first, treatment planning was crude and the treatment setup consisted of clinical palpation and visually aiming at the disease, until the development of simulators. Conventional radiotherapy simulators are isocentric units, offering the same degrees of freedom as a linear accelerator in terms of treatment geometry, but have a diagnostic quality X-ray tube as the radiation source. The X-rays images produced show bony structures in the treatment area and offer little soft tissue information. Using these bony landmarks, the beam geometry and the field shape are determined, and a lead wire impression of the patient contour may be hand-drawn on paper and then manually digitized. The patient is represented by this one central plane containing the contour and the beam central axis. The planning system assumes that all the other parallel patient planes are identical to this cross-section, and no heterogeneity corrections for tissue density are possible. Treatment planning using this technique was laborious and error prone, and large fields with wide margins led to minimal sparing of healthy tissue.

A major innovation in radiation therapy treatment planning was the implementation of computed tomography (CT) scanners. In the original method, CT data was used in conjunction with simulator information. Patient contours and target location were obtained from cross-section images with excellent soft tissue contrast, and they were extrapolated to the simulator radiographs. This process allowed for a better determination of beam geometry and field shaping, as well as for multi-planar 2D treatment planning. Dose distributions were calculated in all the planes, one plane at a time, not taking into effect the shape of the patient contour beyond the calculated slice.

True 3D treatment planning began with the advent of more powerful computers and the development of more elaborate treatment planning algorithms. Using the patient CT data, treatment volumes and critical organs were delineated directly on the CT data. The International Commission on Radiation Units and Measurements (ICRU²⁸) defined new volumes to suit 3D treatment planning. Gross tumor volume (GTV) was defined as the palpable or visible malignant growth, clinical target volume (CTV) included the GTV and microscopic extensions of the growth, and the planning target volume (PTV) added a margin to the CTV, to account for treatment uncertainties such as organ motion and patient positioning error. Volumetric 3D dose calculation took into account the 3 dimensions of the beam divergence and could correct for the tissue heterogeneities. The treatment plans were also evaluated in 3D, using dose-volume histograms (DVH) and dose displays in the axial, coronal and sagittal planes. Dose distributions could also be visualized in 3D and superimposed on the patient CT dataset. In fact, CT based planning has become routine practice, and dedicated CT scanners for use in radiotherapy treatment planning, namely CT-simulators, have been developed.

The CT-simulator is a dedicated CT scanner for radiation therapy. It uses axial, sagittal and coronal lasers to align the patient in the treatment position and allows for the definition of a reference isocenter. It has a flat top couch, similar to the flat tabletops of the treatment machines. The large bore allows the CT scanning of the patient with the required treatment positioning and immobilization accessories. Reference fiducial marks are put on the patient at the time of the CT and define the origin of the planning reference frame. Contours for the various structures are drawn on CT images and the target isocenter location is determined in the reference frame. Using a computer model of a radiotherapy machine and the CT images of the patient, the orientation and field shape of the beams are determined in virtual space. This virtual simulation allows for the conventional simulator to be removed, and the patient simulation time is reduced. Virtual simulator software generates images of the patient, based solely on the CT data. Beam's eye views (BEV) are planar projections of beam geometry and outlined contours onto a virtual film plane. Digitally reconstructed radiographs (DRR) are synthetic x-rays created by projecting a virtual X-ray source with the proper divergence through the CT data and performing line integrals of the attenuation coefficients of the virtual patient with the results projected on

the desired film plane. The resulting digital image replaces the simulator film and can easily be compared to portal images verifying patient alignment on the treatment machine, either digitally or with printed films. Figure 1.1 shows a BEV of the GTV, CTV, PTV and field shape for the anterior field of a lung tumor case, superimposed on a DRR of the patient.

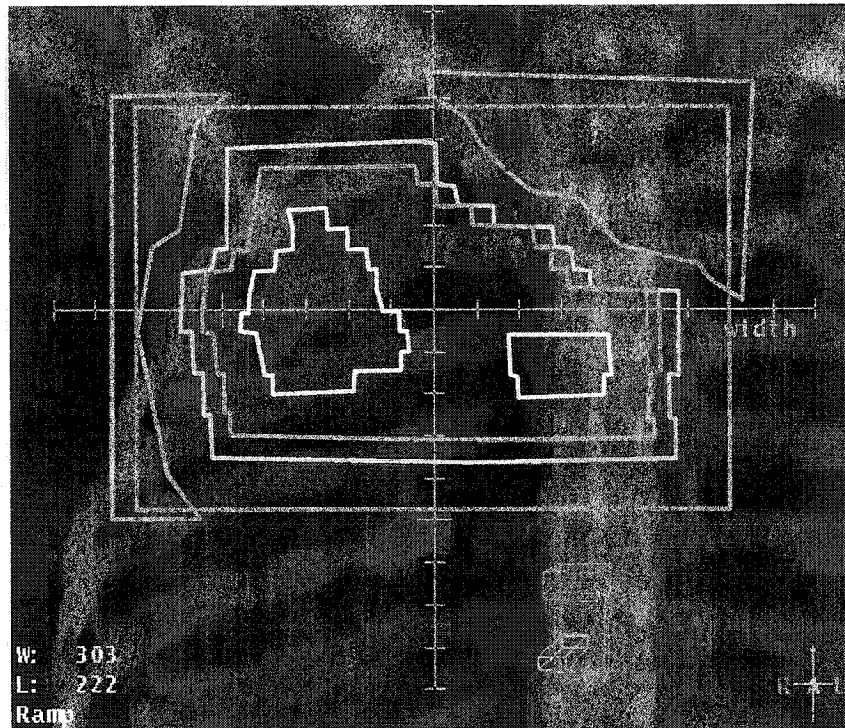


Figure 1.1: BEV and DRR of the anterior field of a lung tumor case.

The GTVs (white), CTV (orange), PTV (yellow), field size (green) and custom blocks (blue) for this beam's eye view are superimposed on the radiograph digitally reconstructed from the patient axial CT slices.

For treatment, the patient is aligned on the treatment machine isocenter with the reference fiducial marks and then moved by the predetermined offset required to place the target isocenter at the treatment machine isocenter. Virtual simulation facilitates the use and positioning of a large number of beams, which may be needed in 3D conformal radiation therapy. Multiple beams are set and custom-shaped individually following the geometrical 2D projection of the target²⁹ in order for the 3D dose distribution to conform as well as possible to the target volume. The beam orientations are also selected to minimise the overlap of beams in normal tissue³⁰.

Although 3D conformal radiation therapy is effective, it is limited to targets with a relatively simple shape in which critical organs are not in the way. The next step takes us to intensity modulated radiation therapy (IMRT), which can geometrically conform a uniform high dose to the target, while respecting the low dose constraints of the surrounding critical structures.

1.2.1 Intensity modulated radiation therapy (IMRT)

IMRT is a beam delivery modality that allows for the spatial and temporal modulation of beam intensity during patient treatment. Each beam is divided into hundreds of beamlets, which all have different intensities. The combination of multiple intensity modulated beams will lead to a dose distribution that is as uniform as possible over the target volume and has a sharp dose drop-off at its edge to protect the surrounding healthy tissue³¹.

Intensity-modulated radiation treatments are most often delivered using a multileaf collimator (MLC). This mechanical beam shaping device consists of two banks of thin vertical plates that can be independently placed so their inside edges define an irregular field shape. Commercially available MLCs have between 50 to 120 leaf pairs with a leaf thickness of 0.5 or 1 cm. The MLC can be located below the two sets of collimator jaws or can replace one set. The planning system transforms the calculated beam intensity distribution into a deliverable set of leaf sequences, using the characteristics of the selected MLC. The user can choose to deliver the planned dose with moving leaves (dynamic MLC) or with the step-and-shoot technique, where the intensity modulation is obtained by the summation of different fixed, automatically delivered MLC fields. IMRT can be forward-planned (manually) on a conventional 3D treatment planning system, or inverse-planned on dedicated systems.

1.2.2 Inverse treatment planning

In forward planning, such as 3D conformal therapy, most of the work is done by the dosimetrist. The beam directions, beam weights, field shapes, wedges etc. must be all specified. The dose distributions are then calculated by the treatment planning system, and

are individually evaluated. Improvements to the plan are made by manually changing the beam parameters and the process is repeated until an acceptable plan is obtained³².

IMRT fields are divided into a number of beamlets, each with its own optimal intensity. For a large number of beamlets, it is impossible to manually adjust each beamlet weight in order to obtain the desired dose distribution. In inverse treatment planning, the desired dose distribution parameters are defined *a priori*, and the treatment planning system works iteratively to find the intensity modulation that leads to this result³². Of course, there is some forward planning involved, for instance the number of beams and their orientation must be defined before the inverse treatment planning can take place.

In the inverse planning process, an optimization routine is used to reach the desired objectives³³. In most cases, the dosimetric and clinical objectives consist of minimum and maximum doses and dose-volume constraints for the target and the critical organs involved³¹. They are stated mathematically in the form of an objective (or cost) function. With an initial set of beamlet intensities, a dose is calculated for every voxel of the patient's 3D data set. Points in the body receiving doses that do not respect the pre-determined constraints add a certain penalty and increase the objective function score. The computer uses an iterative process to find the beamlet intensity distribution that minimises the objective function. Each iteration is composed of a small beamlet weight variation, the recalculation of the dose distribution and finally the objective function score calculation. These iterations take place until there is no improvement to the treatment plan that is then assumed to be optimal. This gradient technique, though very fast, has the disadvantage of assuming the presence of only one objective function minimum. Stochastic optimization techniques, such as simulated annealing, move randomly across the objective function in order to find which of the possible multiple minima is the global minimum. When the optimal plan is reached and accepted, the treatment planning system will then transform the intensity modulated beams into a deliverable set of MLC leaf sequences.

1.2.3 Dosimetry and quality assurance for IMRT

The IMRT treatment plans are easily evaluated using 2D and 3D dose displays and dose-volume histograms, much like conventional plans. It is however much more difficult to evaluate their actual delivery. Unlike conventional treatments, where the monitor units (MU) are recalculated by hand to make sure the prescribed dose is respected, an independent manual check proves to be impossible in the case of the complex intensity-modulated beams. One must therefore trust an independent software verification for the MU calculation, or physically measure the dose distributions before the first treatment³¹.

IMRT quality assurance (QA) may involve the dosimetric measurements of each dynamic beam or of the complete treatment plan. Radiographic film, placed in solid water phantoms, can be used to verify each beam, however, this only provides dose information in one plane, at a given depth. Some electronic portal imaging devices (EPIDs) can be used to verify a dynamic beam before the treatment and also during the patient treatment and compare it to a portal dose image constructed by the treatment planning system. EPIDS however lack contrast in high energy photon beams³⁴, and only give 2D information³¹.

Thermoluminescent dosimeters (TLDs) and diodes can both be used in a phantom or on the patient skin, but they only provide point information³⁴. Ion chambers can be very accurate, but are useful only in a phantom at a single point.

IMRT allows for tighter margins around the target volume. This means that both the MLC leaves and the patient must be accurately positioned. The QA for the MLC requires frequent checks to make sure the leaves move to the designated position, for step-and-shoot techniques, and that their speed and position are accurate in the case of dynamic delivery techniques. The best QA tool for IMRT would be a 3D integrating dosimeter with a spatial resolution similar to the MLC dose delivery resolution. The Fricke-gel dosimeter has these characteristics.

1.3 Goals of this thesis

The main objective of this work is to show the potential usefulness of the Fricke-gel dosimeter as a quality assurance tool to verify IMRT treatments produced by inverse treatment planning. The specific goals of this thesis are:

- 1) To obtain a working 3D integrating dosimeter, that can be satisfactorily compared to other dosimetric tools.
- 2) To measure relative 3D dose distributions for complex beams, such as the ones found in IMRT and created by inverse treatment planning.
- 3) To measure dose-volume histograms for specific cases in the gel dosimeter, by combining CT anatomical information with MR measured data.
- 4) To show the potential of the gel dosimeter as a practical quality assurance tool for IMRT and inverse planning.

Chapter Two

2 The Fricke-gel dosimeter

The Fricke-gel dosimeter takes its name from the incorporation of a ferrous sulphate solution, similar to the well-known standard Fricke solution, into a gelatin matrix to preserve the spatial distribution of the radiation-induced transformations. This chapter features a brief overview of the general chemical dosimetry of both the Fricke solution dosimeter and the Fricke-gel dosimeter. A short discussion on the general characteristics of the Fricke-gel dosimeter concludes this section.

2.1 Chemical dosimetry

Ionising radiation deposits energy in the media it encounters. The amount of energy absorbed (Joule) by unit mass (kilogram) of medium is called absorbed dose, and its SI unit is the Gray (Gy), where

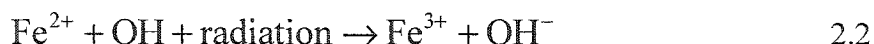
$$1 \text{ Gy} = 1 \text{ J/kg} \quad 2.1$$

For some types of media, radiation will induce chemical changes that can be measured and related to the absorbed dose, leading to chemical dosimetry. The irradiated medium, which is the chemical dosimeter, can have a gaseous, liquid or solid state and can be molded into various phantom shapes. Its chemical composition, density and atomic structure can also be varied to mimic various biological materials³⁵. The radiation chemical

yield, termed G-value, is the amount of chemical product produced per unit energy absorbed. It is most often referred to as the number of ions produced per 100 eV of energy absorbed³⁶, although its official SI unit is mol/Joule.

2.2 The Fricke solution dosimeter

Fricke solution is the most widely known and used chemical dosimeter. It is based on the radiation induced oxidation of an aerated ferric sulphate solution³⁷. The simplified basic reaction can be written as:



The ferric (Fe^{3+}) ion concentration of the solution, produced by the oxidation of the ferrous (Fe^{2+}) ions, is measured spectrophotometrically at the ferric ion absorption peak of 304 nm³⁸. It can also be measured by nuclear magnetic resonance methods such as analytical NMR and MRI^{2,39}.

The standard aqueous Fricke solution consists of 1 mM of ferrous sulphate (FeSO_4) or ferrous ammonium sulphate ($\text{Fe}(\text{NH}_4)(\text{SO}_4)_2$) added to a 0.8 M sulphuric acid (H_2SO_4) solution³⁵. The addition of 1 mM of NaCl to the mixture reduces the unpredictable sensitivity-enhancing effect of organic impurities in the system³⁵. The solution must be saturated in oxygen in order to obtain a G-value of 15.5 ± 1.0 ions / 100 eV. The solution concentrations are chosen to create a medium that is close to being tissue-equivalent. This chemical dosimeter has a linear dose range from 40 to 400 Gy⁴⁰, although changing the concentrations of its constituents can extend this range. The addition of organic agents, such as benzoic acid (a eye and skin irritant food preservative) leads to an increase in the dosimeter sensitivity⁴¹. The Fricke solution can be used as an absolute dosimeter and can measure doses with an accuracy better than 1%⁴⁰.

2.3 The Fricke-gel dosimeter

One of the disadvantages of the Fricke solution is that it does not preserve spatial dose information. To spatially stabilize the ferrous and ferric ions, the solution may be

incorporated into a gel matrix made of gelatin or agarose. This process will preserve the dose distribution across the dosimeter, and the resulting spatial dose distribution can be determined by MRI. The addition of a known concentration of this organic "impurity" approximately doubles the radiation sensitivity of the dosimeter.⁴

The Fricke-gel dosimeter used in this thesis is composed of 5% gelatin by weight, 1 mM ferrous ions, 1 mM NaCl and 0.05 M sulphuric acid in distilled water. This composition is consistent with the gel compositions used by Olsson⁴ and Hazle⁶ in their work.

2.4 Radiation chemistry of the Fricke-gel dosimeter

The radiation chemistry of gel dosimeters is well known⁸. The reactions governing them can be divided into three stages: the initiation stage (water radiolysis), the propagation stage (ferric ion production chain reactions) and the termination stage.

2.4.1 The initiation stage

In dilute solutions, the dominant interaction of the radiation photons is with the water molecules. These water molecules are ionised and eject electrons, which cause further ionisations and excitations in the medium. This initial step is followed by the slowing down of the resulting electron, which is surrounded by water molecules to become a hydrated or aqueous electron.

The presence of sulfuric acid in the mix leads to a low pH (around 1.5) consistent with the presence of hydrogen ions. These ions react with the hydrated electron to produce hydrogen radicals ($\bullet\text{H}$). The remaining positive water ion (H_2O^+) reacts with other water molecules to form a hydronium ion (H_3O^+) and a hydroxyl radical ($\bullet\text{OH}$). The gelatin macromolecule (RH) is able to react with both hydroxyl and hydrogen radicals. This creates organic radicals ($\bullet\text{R}$), water and hydrogen. Figure 2.1 illustrates the initiation stage process.

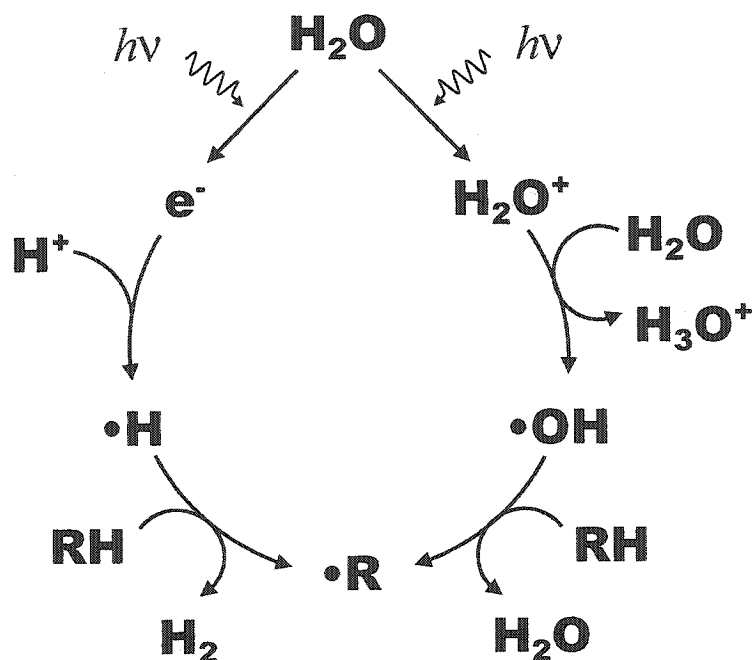


Figure 2.1: Initiation stage.

The interaction of radiation with a water molecule leads to organic ($\bullet\text{R}$), hydroxyl ($\bullet\text{OH}$) and hydrogen ($\bullet\text{H}$) radicals.

2.4.2 The propagation stage

Two separate reaction mechanisms are responsible for the oxidation of the ferrous ions into ferric ions. The reactions of the first propagation mechanism (Figure 2.2) rely only on interactions between the water radiolysis products and the ferrous ions, and yield two ferric ions per ionized water molecule. The second propagation mechanism (Figure 2.3) occurs in the presence of the gel macromolecule and of oxygen. These support a chain reaction that also generates two ferric ions per reaction cycle.

2.4.3 The termination stage

Competing reactions are responsible for terminating the chain reaction. Coupled with the creation of the reduced (RX) and oxidized (ROH) forms of the gel macromolecule, the elimination of the radicals ($\bullet\text{R}$, $\bullet\text{RO}_2$, $\bullet\text{RO}$ and $\bullet\text{OH}$) slows down the termination process and eventually ends the chain reaction. Some ferric ions are also produced at this stage, which is presented in Figure 2.4.

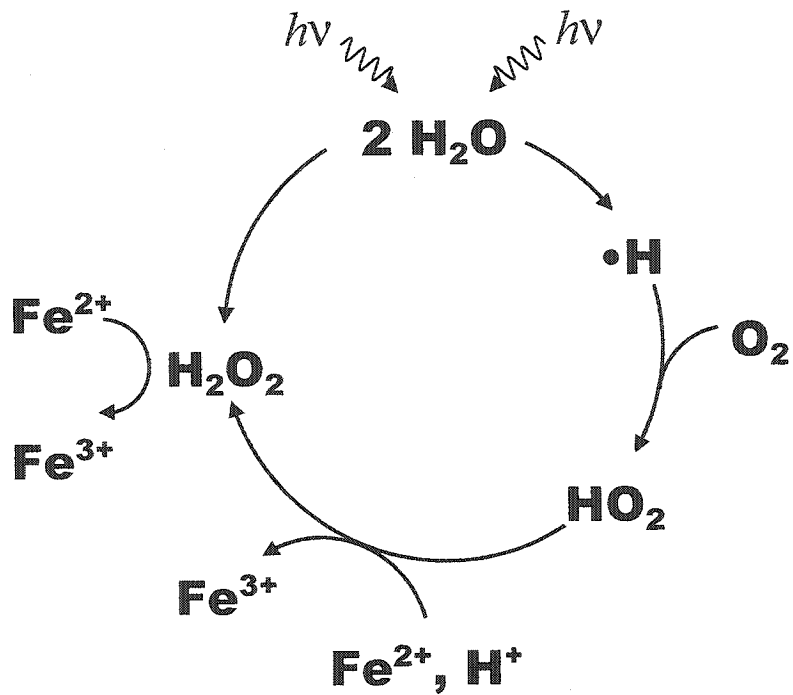


Figure 2.2: Propagation stage (1st mechanism).
 Two ferric ions are produced by the interaction of the radiation-ionized water molecule with ferrous ions.

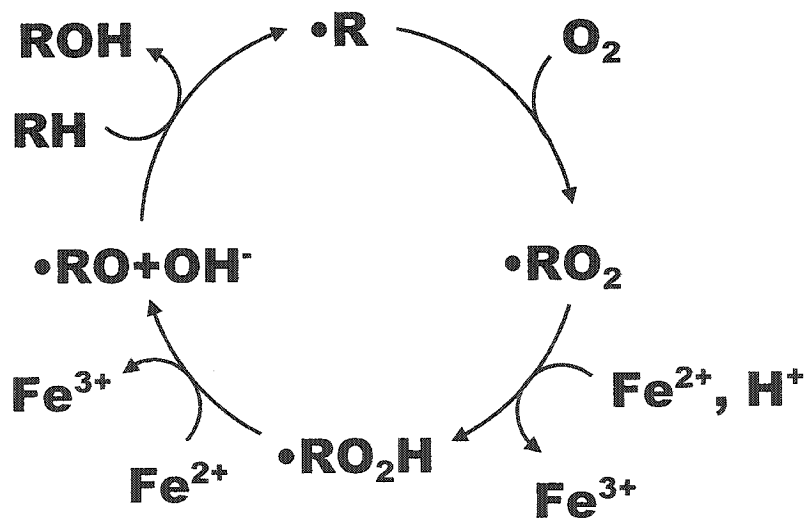


Figure 2.3: Propagation stage (2nd mechanism).
 The chain reaction between the organic radical and oxygen yields two ferric ions per reaction cycle.

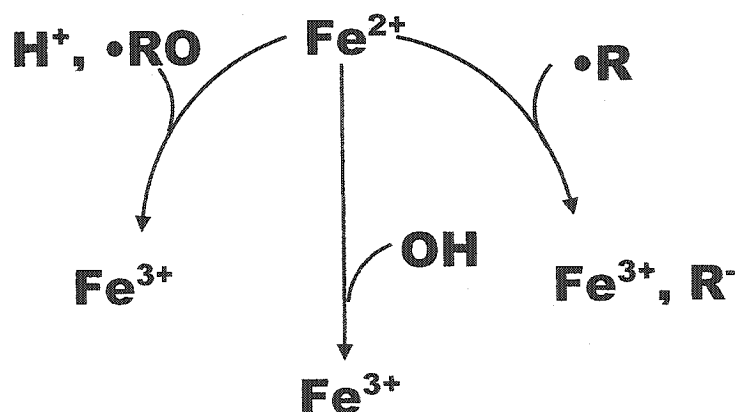


Figure 2.4: Termination stage (main mechanism).

The chain reaction in Figure 2.3 is slowed down and stopped by the elimination of the organic radicals. This step also yields ferric ions.

The conversion of Fe^{3+} ions back into Fe^{2+} , as shown in Figure 2.5, may be significant for very high concentrations of Fe^{3+} ions, and lead to a reduction of the chemical yield of the system. This effect is however negligible at the ferric ion concentrations encountered in this thesis.

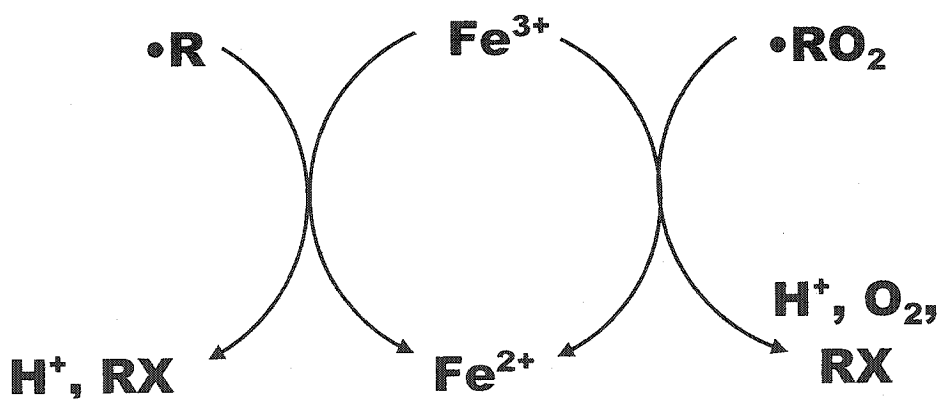


Figure 2.5: Termination stage (minor mechanism).

The elimination of organic radicals can also revert ferric ions to the ferrous state. This effect is negligible at the ferric ion concentrations encountered in this thesis.

The ferric ions that are generated at many points along the production path lead to an increased G-value for the gel dosimeter as compared to the G-value of the standard Fricke solution dosimeter.

2.5 General characteristics of the Fricke-gel dosimeter

The principal characteristics of a dosimeter are absoluteness, precision, accuracy, sensitivity, dose range, dose-rate range, energy dependence, stability and configuration.

2.5.1 Absoluteness

Fricke solution is considered an absolute dosimeter when absorption spectroscopy or titration measures the Fe^{3+} concentration directly. To preserve 3D spatial distribution, this solution is incorporated in a gel. A magnetic resonance imaging scanner can be used to measure the magnetic perturbations (increased spin-lattice relaxation rate) caused by the presence of Fe^{3+} ions and map out their distribution. Since the raw MR image intensity is not linear with dose, a calibration curve using vials irradiated at known doses is required to obtain dose values from the gel dosimeter. However, the dose is proportional to the longitudinal relaxation rate (R_1), which is calculated pixel by pixel from two images with different scan parameters. The R_1 map can then be renormalized to a point where the expected dose is known. In this case, the gel becomes a relative dosimeter.

2.5.2 Precision and Accuracy

Precision refers to the reproducibility of dosimeter measurements. The precision of a set of measurements, also called uncertainty, is associated with a small standard deviation³⁵ and it excludes systematic deviations. The precision of the gel dosimeter depends on a high signal-to-noise ratio of the MR intensities and also on a small MR voxel size. Improving one of these factors is usually detrimental to the other, so great care is necessary in order to obtain images with adequate precision. The chapter on MR imaging will explore this in greater detail. Accuracy is related to the closeness of the measurement to the true value. It reflects the collective effect of both systematic and random errors. According to Attix³⁵, "In experiments that are limited to relative measurements, only the precision, not the accuracy, is important."

According to ICRU Report 42⁴², in order to be a useful quality assurance tool, the gel dosimeter must be able to detect differences of 2% in dose, or 2 mm positional error. The

precision of the gel dosimeter has improved noticeably over the years. Olsson⁵ obtained in 1990 an overall uncertainty of 20% using agarose gel. In 1991, Hazle⁶ observed the reproducibility of a gelatin dosimeter to be 5% in the 20 to 35 Gy dose range, and about 10% at 5 Gy. In 1995, Chan²⁵ compared the dose-response curve of five batches of the gelatin dosimeter and the reproducibility was found to be within 2%. The uncertainty in individual experiments was within 5%. Using agarose, Johansson²⁶ observed a precision around 1.5%, while Back⁴³ calculated the expanded uncertainty (95% confidence) of 15 mm slices to be 1.6% at high doses (≥ 30 Gy) and 3.3% at zero dose.

2.5.3 Dose sensitivity, range and saturation

The important parameters relating to dose range are dose sensitivity, minimum detectable dose, upper range limit and saturation. The sensitivity of a measuring device describes the variation of the response to the variation of the stimuli. The larger the sensitivity, the easier it is to discern between two input levels that might be close. The sensitivity of a dosimeter can be defined as the slope of the signal vs. dose curve. When the sensitivity is constant over the useful range of values, the measuring device is said to have a linear response. In the case of the gel dosimeter, since the information extracted from the MR images is a relaxation rate (s^{-1}), the dose sensitivity is given in $s^{-1}Gy^{-1}$.

For a gel containing 5% gelatin by weight, Hazle⁶ measured a sensitivity of $0.0423 s^{-1} Gy^{-1}$. Olsson⁵ showed that an increase in concentration of gelatin leads to a decrease in sensitivity. To ensure a properly working dosimeter, the sensitivity of the gel and the dose range should preferably be verified for each prepared batch of gel.

According to Olsson⁴, the Fricke-gel dosimeter shows a linear dose response in the 0 to 40 Gy interval. In 1991, Hazle⁶ verified the linear relation using irradiated phantoms at different doses and found a useful interval of 0 to 50 Gy. Beyond the upper limit of the linear range, there is a decrease in dose sensitivity ending in saturation.

The minimum detectable dose is defined as the absorbed dose corresponding to three times the standard deviation above the background⁴⁴, using the standard deviation of a large

number of measurements (or pixels) at zero dose. The minimum detectable dose for Fricke-gel is approximately 1 Gy^{4,45}.

2.5.4 Irradiation configuration factors

In the dose-rate range used by medical linear accelerators, Olsson⁴ found no significant absorbed dose-rate dependence of the ferrous sulphate gels. The gel dosimeter was found to be water-equivalent¹⁴ and therefore soft-tissue-equivalent¹⁵ in the usual radiation therapy photon and electron energy ranges since it has similar values for effective atomic number (Z_{eff}) and electron density (ρ_e). Since the gel itself is water-equivalent, the molding wall material should also be as close to water-equivalent as possible. In this thesis, the gel phantom molds are made of acrylic, which is frequently used as dosimetric phantom material⁴⁶. Furthermore, the American Association of Physicists in Medicine's Radiation Therapy Task Group 21 has stated that replacement corrections are not required if low density thin phantom walls are used for Fricke ferrous-sulphate dosimeters⁴⁷. The phantoms are in the shape of a square box or a molded head phantom.

2.5.5 Stability

Concerning the gel dosimeter, two factors influence the stability with time. First, a slow oxidation of ferrous ions to ferric ions reduces the sensitivity of the gel when too much time passes between preparation and the experiment. Secondly, both the ferrous and ferric ions diffuse after irradiation, leading to a degradation of the dose distribution with time, especially where large dose gradients are found. To minimize the first effect, the gel should be used as soon as prepared, but enough time must be given for the gelatin to solidify in order to minimize the diffusion. Also, to minimize the diffusion, it is imperative to complete the post-irradiation imaging of the gel within 2 hours¹¹. The percentage of gelatin can be increased from 5% to 7.5% to reduce diffusion²⁵, but this also decreases the sensitivity of the gel⁵.

Having discussed the background of the Fricke-gel dosimeter, the process of measuring dose with this dosimeter must be covered. The next chapter explains how the MR signal is produced in the gel and how a spatial distribution can be obtained with MRI.

Chapter Three

3 Magnetic Resonance Imaging

Magnetic resonance imaging (MRI) uses magnetic fields, radio signals, and computers to obtain detailed anatomic information. Liquids and tissues with varying water concentrations and fat contents can be discriminated by magnetic resonance imaging. MRI is therefore able to differentiate between various soft tissues. The presence of paramagnetic ions in the medium also affects the magnetic characteristics of the hydrogen nuclei⁴⁸. In Fricke-gel dosimetry, MRI is used to map ferrous and ferric ion distributions within the dosimetric gel by taking advantage of their different paramagnetic properties².

This chapter presents a brief history of MRI and an overview of the basic concepts of magnetic resonance imaging. It also introduces the reader to the MR imaging process and to the instrumentation specific to this technique.

3.1 Development of magnetic resonance imaging

In 1946, Bloch⁴⁹ and Purcell⁵⁰ independently discovered nuclear magnetic resonance (NMR) for which they later shared a Nobel Prize. A few years later, researchers using proton NMR investigated the water content of potatoes and maple wood⁵¹ as well as human and mammalian tissue samples⁵². Prior to 1973, NMR spectroscopy was used to investigate the chemical properties and composition of samples such as animal proteins, tissues and

organs. This was made possible by a phenomenon known as chemical shift, where the electron cloud surrounding a molecule in a given chemical environment influences the resonant frequency of the nuclei.

In 1972, Damadian⁵³ filed a patent in the United States for a clinical NMR body scanning technique. Interestingly, the patent title was "*Apparatus and method for detecting cancer in tissue*". In 1973, Lauterbur⁵⁴, and Mansfield and Grannell⁵⁵ used magnetic field gradients to artificially shift the resonant frequencies in order to probe the spatial distribution of nuclei, and thus obtained the first images from small objects. The first image of a live human finger was presented by Mansfield and Maudsley⁵⁶ in 1976 and the first whole body image was published a year later by Damadian⁵⁷. The first commercial NMR scanner became available in 1978. The ability of MR to discriminate between various soft tissues led to the demonstration of abnormal human pathology by Hawkes⁵⁸ in 1980. As the technique became more widespread and clinically implemented to diagnose disease, the word "nuclear" was dropped to prevent false concerns in the public. The following section explains why and how the nucleus of the atom shows resonance.

3.2 Basic nuclear magnetic resonance

Most atoms possess a nucleus that behaves like a tiny magnet with a north pole and a south pole. When placed in an external magnetic field, the magnetic moments of the nuclei align with the field direction. A specifically tuned radiofrequency pulse will excite these moments and tip them to a given angle. The magnetic moments of the nuclei will combine to create a net magnetisation that is no longer parallel to the external magnetic field. The decay of this magnetisation, as the tipped nuclei return in time to their equilibrium state, creates a decaying induced current in the MR receiver coil. This is the magnetic resonance signal, and is termed free induction decay (FID).

3.2.1 Nuclear spin

Nuclei with an odd number of protons and/or an odd number of neutrons possess spin angular momentum, S , a property responsible for nuclear magnetic resonance. Examples of

these nuclei are ^1H , ^{31}P , and ^{23}Na , although clinical MRI almost exclusively probes the hydrogen protons (^1H) found in the body's water. A spinning nucleus, which can be considered a charged sphere, is like a small magnet spinning about its long axis, as seen in Figure 3.1. It induces a current loop, which creates the magnetic dipole moment, μ

$$\mu = \gamma S = \gamma \frac{h}{2\pi} I \quad 3.1$$

where I is the spin operator in quantum mechanics, h is Planck's constant, and γ is the gyromagnetic ratio of the nucleus, which will be seen in the next section. The magnetic dipole moment is a vector that has the same direction as the rotation axis of the nucleus.

3.2.2 Net magnetization and Larmor precession

Usually, the nuclei in a medium are randomly oriented and the net magnetization of the medium is zero. Placed in a static magnetic field, \mathbf{B}_0 , the spinning nuclei will have a tendency to align their magnetic dipole moment with the magnetic field direction. More will align in a parallel fashion than anti-parallel, leading to a net magnetization, \mathbf{M} , which is aligned with the magnetic field. However, the magnetic moments do not individually align with the field completely since the presence of the external field applies a torque to the spinning nuclei, forcing them to rotate around the direction of the field. This is called precession. Figure 3.1 shows the magnetic moment of a nucleus precessing in the presence of the external magnetic field. The frequency of precession is proportional to the magnetic field strength, as given in the well-known Larmor equation⁵⁹:

$$\omega_0 = \gamma B_0 \quad 3.2$$

where ω_0 is the Larmor angular precession frequency of the nuclei, B_0 is the magnetic field strength (amplitude of \mathbf{B}_0) and γ is the gyromagnetic ratio that is characteristic of the nucleus involved. The gyromagnetic ratio of the ^1H atom is 42.58 MHzT^{-1} . For a magnetic field strength of 1.5 Tesla, at which these Fricke-gel dosimetry experiments were carried out, the Larmor frequency of the ^1H atom is 63.87 MHz.

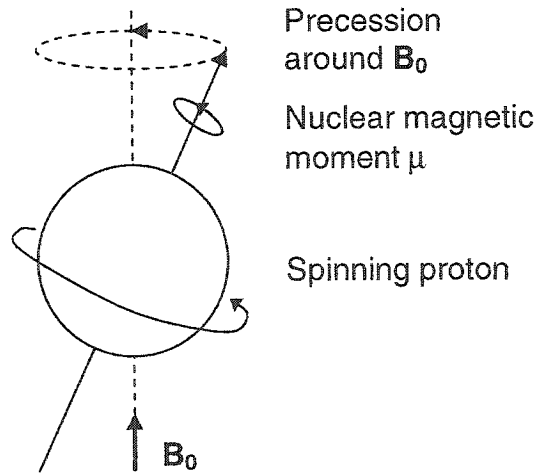


Figure 3.1: Nucleus precessing around magnetic field B_0 .
The frequency of precession is directly proportional to the magnetic field B_0 .

3.2.3 Excitation pulses and magnetization recovery

In a frame of reference rotating at the Larmor frequency, the net magnetization \mathbf{M} is aligned with the static magnetic field B_0 at equilibrium (Figure 3.2 a). It can be decomposed into two vectors, M_z , which is equal to \mathbf{M} at equilibrium, and M_{xy} , which is zero at equilibrium. The M_{xy} component can be measured with a coil in the xy plane since the magnetization variation along the coil axis will induce a measurable current. Tilting \mathbf{M} to the xy plane is made possible by the resonance property of the nuclei. A burst application of a magnetic field B_1 , oriented in the xy plane and rotating at the Larmor frequency, excites the nuclei, tilts their magnetic moments and makes them precess in phase for a short period of time. The burst application of the magnetic field B_1 is called the excitation pulse. A 90° pulse has a duration and amplitude that causes the net magnetization \mathbf{M} , to tilt 90° to the xy plane (Figure 3.2 b).

In the laboratory frame of reference, \mathbf{M} spirals down the surface of a sphere as a result of the B_1 field application (Figure 3.3 a). Right after the pulse, M_z is zero and M_{xy} reaches a maximum equivalent to the original M_z amplitude⁶⁰. If the excitation pulse is double the size of the 90° pulse, either in duration or amplitude, it will invert \mathbf{M} and right after the pulse, the amplitude of M_z will have the same value as before the pulse but with a reversed sign, and M_{xy} remains zero⁶⁰.

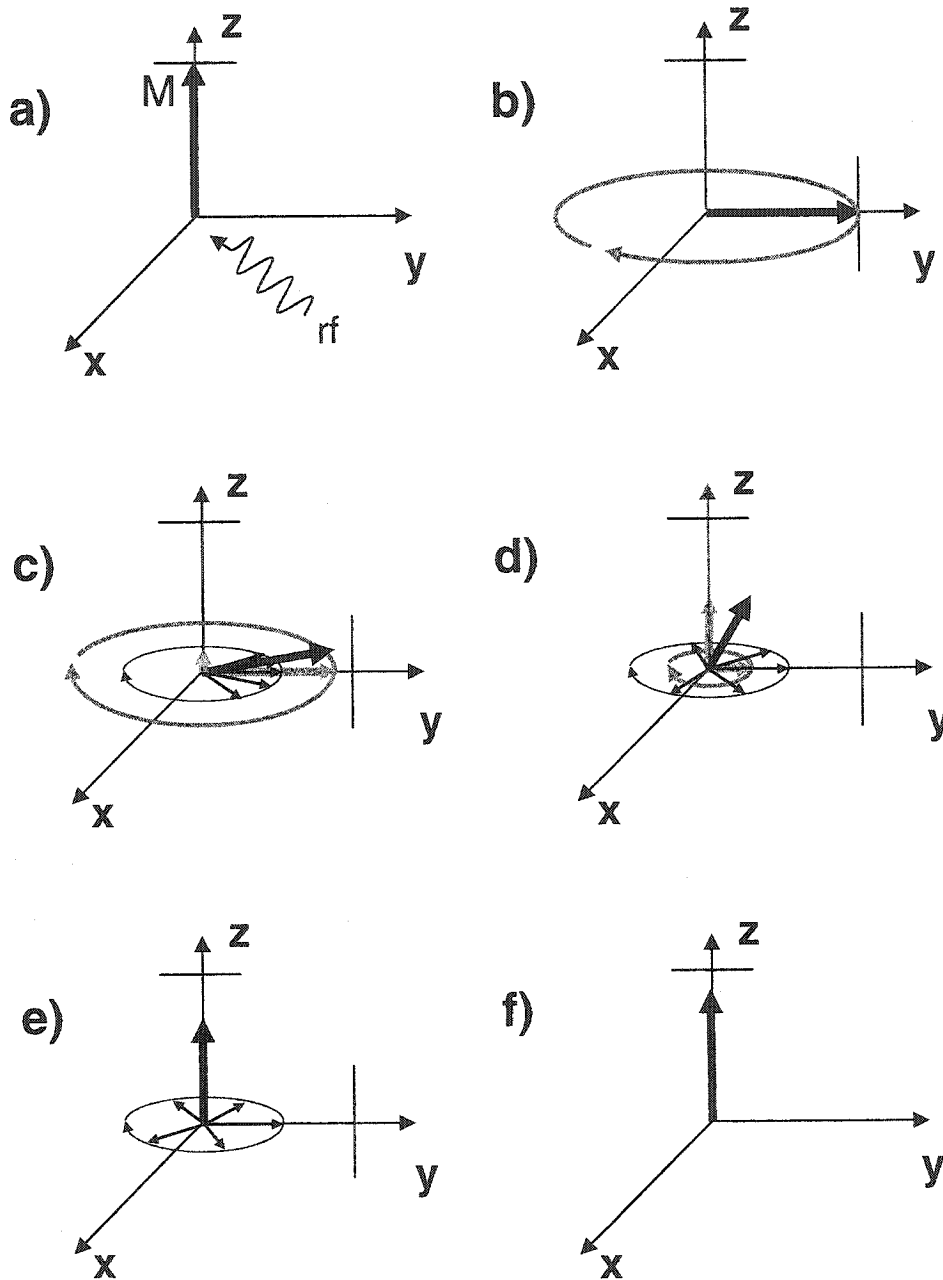


Figure 3.2: M_{xy} decay and M_z recovery after excitation.

This figure shows the progression of the M_{xy} and M_z components of the net magnetization after a 90° excitation rf pulse. a) Just before the pulse, $M_z = M$. b) Just after the pulse, $M_{xy} = M$. c) and d) show the decay of M_{xy} and the recovery of M_z (grey arrows). M (black arrow) is the vectorial summation of the two components. The thin black arrows represent the individual magnetic moments that are dephasing. In e) all the induced phase coherence has decayed, and no more signal is measured. f) M_z recovers more slowly than M_{xy} decays. If the next excitation occurs at this time, the resulting signal amplitude will be smaller than the original signal.

After the pulse, when the nuclei are once again only subjected to the static magnetic field B_0 , the precessing magnetic moments return to equilibrium and the electro-magnetic energy released will produce a signal that can easily be measured by a radiofrequency (RF) coil (Figure 3.3 b). Right after the excitation pulse, the spins composing the net magnetization are in phase with each other and a strong electromagnetic signal can be measured (Figure 3.2b). As this phase coherence is gradually lost (Figure 3.2 c, d and e), the signal, produced by the nuclei returning to equilibrium, decays (Figure 3.3 c).

"The *decay* of the *induced* signal arising from *free* precession of the nuclei in the field B_0 "⁶¹ is called a Free Induction Decay, or FID. A Fourier Transform of the FID (Figure 3.3 d) shows the signal amplitude and frequency. The spread in frequency around ω_0 is due to small inhomogeneities in the magnetic field (no magnet is perfect) and local magnetic field strength variations due to the chemical and physical surroundings of each nucleus. These are also responsible for the dephasing of the magnetic moments during the FID.

3.2.4 Relaxation

The return of the magnetization to its equilibrium value after an excitation is called relaxation. The nuclei involved will release the stored energy via interactions with their surroundings⁶². Magnetic resonance relaxation can be separated into longitudinal and transverse components. Figure 3.4 and Figure 3.5 respectively present the longitudinal and the transverse relaxation processes.

The longitudinal or spin-lattice relaxation represents the restoration of the original net magnetization in the z-axis. In this case, the energy is transferred from the nuclear magnetic spins to the molecular framework or lattice. This is characterized by the spin-lattice relaxation constant T_1 . In the case of a solid, there is a strong coupling within the lattice and T_1 will be shorter than in a liquid sample. Figure 3.4 shows the M_z recovery. After a time T_1 , the magnetization has recovered 63% of its value at thermal equilibrium.

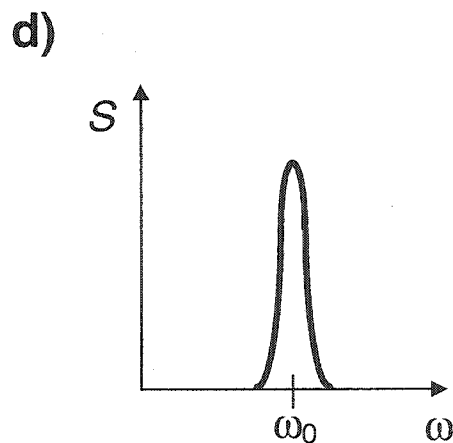
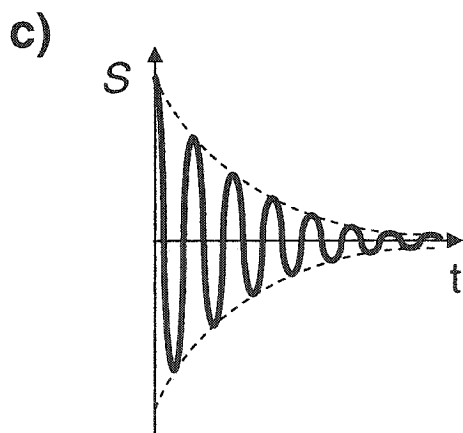
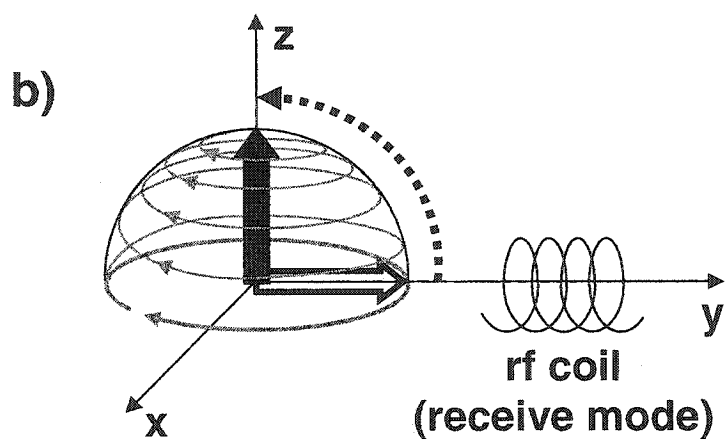
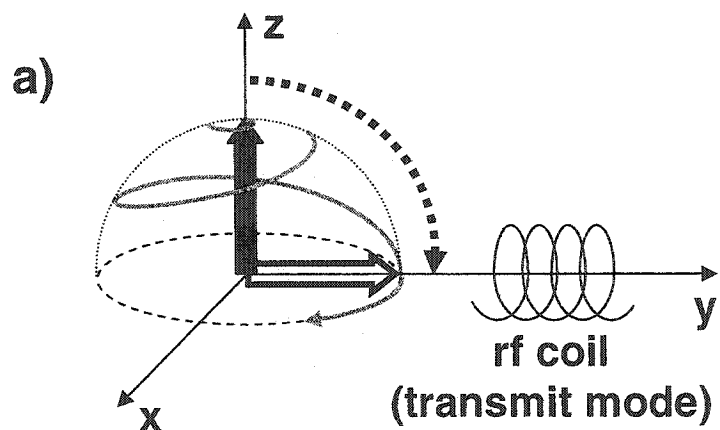


Figure 3.3: Free induction decay (FID) in the space, time and frequency domains.

a) The 90° excitation pulse causes M to flip to the xy plane. Also in the laboratory frame of reference, b) shows the magnetization spiralling up the surface of an ovoid sphere. c) The signal measured by the receiver coil decays exponentially. d) A Fourier Transform to the frequency domain shows the signal amplitude at the Larmor frequency ω_0 .

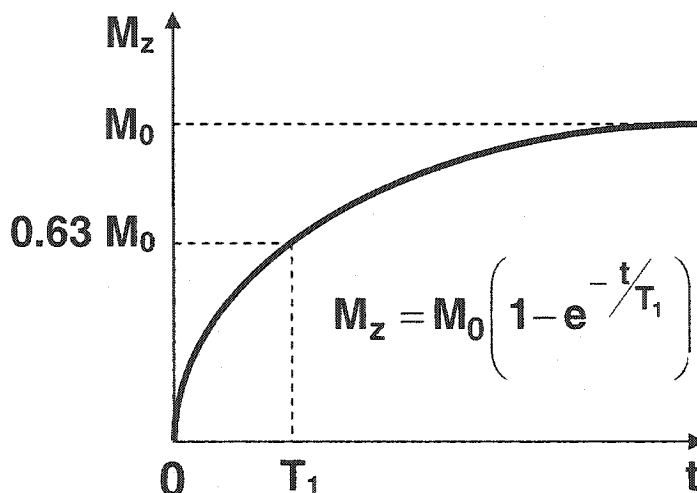


Figure 3.4: Longitudinal relaxation.

An exponential function with T_1 time constant describes the M_z recovery to M_0 , the magnetization value at thermal equilibrium.

Transverse relaxation is the loss of magnetization in the xy plane, which is a combination of the loss of phase coherence, by interactions between neighbouring nuclear spins, and the net loss of signal in the xy plane due to longitudinal relaxation.

The transverse or spin-spin relaxation constant is called T_2 . T_2 is usually much smaller than T_1 in tissue samples, but can approach T_1 for small molecules in a dilute solution⁶². Other factors, such as magnetic field inhomogeneities, contribute to the loss of magnetization in the xy plane. Therefore an effective transverse relaxation rate T_2^* describes the decay of the envelope of the FID, which is shown in Figure 3.5 a), while Figure 3.5 b) compares T_2^* with the theoretical T_2 .

3.2.5 Pulse sequence in MRI

There are many ways to produce a MR signal by tilting the magnetization into the xy plane. Different pulses and pulse sequences are used, depending on the desired result. Section 3.2.3 explained the 90° pulse and the FID signal obtained. A series of these pulses can be combined to form a saturation recovery pulse sequence, as seen in Figure 3.6.

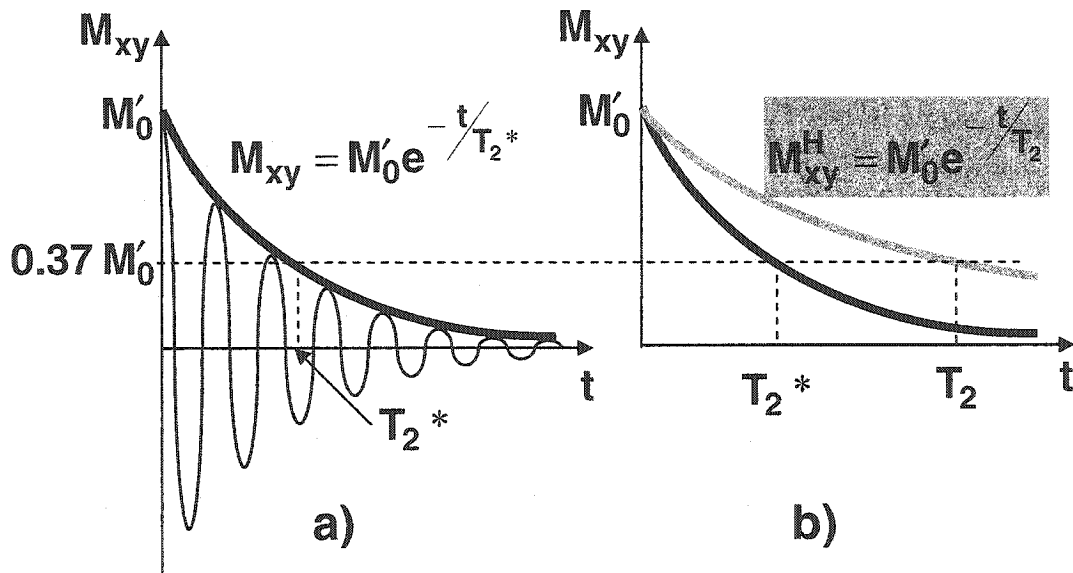


Figure 3.5: Transverse relaxation.

a) An exponential decay function with T_2^* time constant describes the M_{xy} decay from the initial magnetization value M'_0 , which can be smaller than M_0 if M_z has not completely recovered from the previous excitation. b) In the case of a perfectly homogeneous magnetic field, M_{xy} is now M_{xy}^H and decays with the transverse relaxation time constant T_2 .

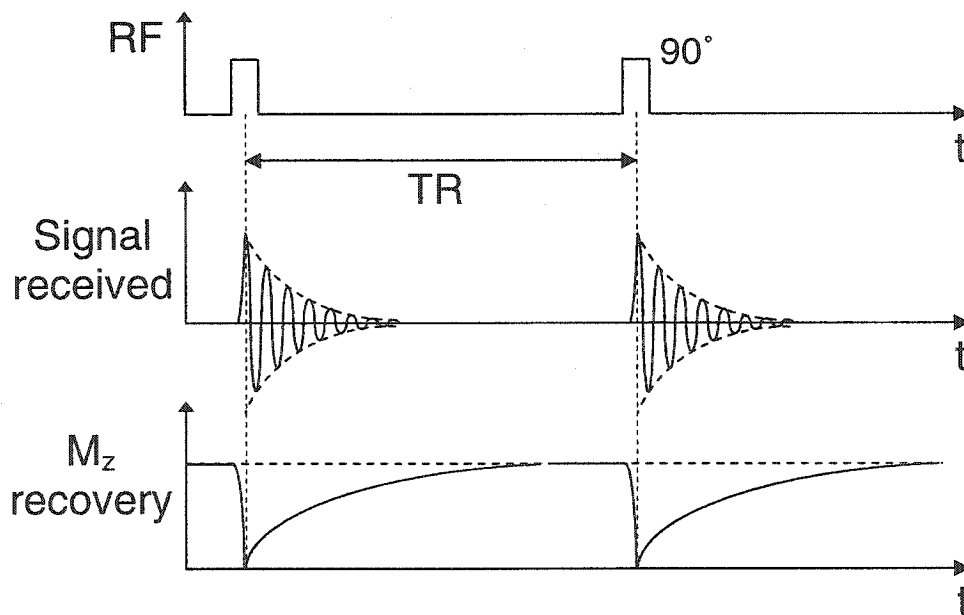


Figure 3.6: Saturation recovery sequence.

The saturation pulse is applied after a sufficiently long repetition time (TR) to have a full M_z recovery.

The saturation recovery sequence is so called because the pulse “saturates” the magnetization in the xy plane and there is no more magnetization in the z -axis. With k as a receiver gain constant, the pixel signal of a saturation recovery sequence will be

$$S_{SR} = kM_0 \left[1 - e^{-TR/T_1} \right] \quad 3.3$$

where TR is the repetition time between each pulse and M_0 is the magnetization value at thermal equilibrium.

The spin-echo pulse sequence is the most commonly used in Fricke-gel dosimetry. The spin echo sequence (Figure 3.7) is similar to the saturation recovery sequence but has a 180° pulse following the 90° pulse, in order to refocus the phase of the spins and create a second signal which occurs at time TE (echo time). Section 3.2.3 explained why this dephasing occurred. The 180° pulse is applied at $\frac{1}{2} TE$.

This can be illustrated by the classical analogy: a group of runners with different speeds are lined up at time $t = 0$ and the race is started. They spread out according to their respective speeds and at time $t = \frac{1}{2} TE$, they are ordered to turn around and run back the other way. At time $t = TE$, the faster runners will have caught up with the slower ones and they will all be lined up before spreading out again. The regrouping spin phases generate a complete signal echo that rises up and down, making easier to record and process, even if the echo amplitude is reduced by T_2 decay. The pixel signal of a spin echo sequence is

$$S_{SE} = kM_0 \left[1 - e^{-TR/T_1} \right] e^{-TE/T_2} \quad 3.4$$

The main advantage of a spin echo sequence is the time delay between the excitation pulses and the echo signal. This allows the possibility of adding magnetic field gradients to artificially shift the resonant frequency and phase of the nuclei by amounts proportional to their location, and thus encoding the signal with positional information.

The imaging technique used in this thesis is a multiple slice variation on the spin echo sequence, and will be explained in greater detail in section 3.3.2.

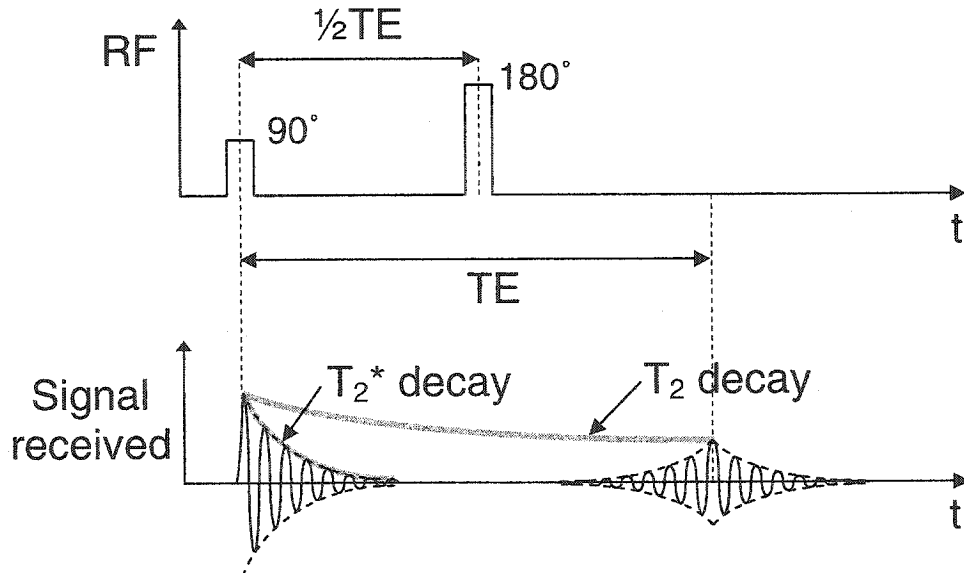


Figure 3.7: Spin echo sequence.

After the 90° pulse, the FID decays with the time constant T_2^* . The amplitude of the echo is governed by T_2 decay and occurs at time TE as a result of an inversion pulse being applied at time $\frac{1}{2} TE$.

3.3 Magnetic resonance imaging

To obtain magnetic resonance images, the signals coming from the different positions in the sample must somehow be spatially encoded. Knowing that the resonant frequency of the nuclei depends on the strength of the applied magnetic field, the nuclei along a line in a given direction will resonate at slightly different frequencies if a magnetic field gradient is applied along that line. Using magnetic field gradients in the x , y , and z directions will yield an image of the signal distribution, the signal of each voxel being related to the proton density and chemical composition of the sample inside that voxel, while its position is determined by its precise frequency and phase.

3.3.1 2D Image acquisition and reconstruction

3.3.1.1 Gradients

The judicious application of magnetic field gradients along the x , y , and z directions leads to frequency-encoding, phase-encoding and slice selection respectively. By

extracting the amplitude of the signal at a given frequency and phase, an MR image of the sample can be reconstructed.

A gradient G_z (from $-G_z$ to $+G_z$) applied along the B_0 direction at the time of the excitation pulse, changes the resonant frequency of the nuclei, except for the region at $G_z = 0$. That axial slice retains the same resonant frequency and will selectively be excited by the RF pulse, as explained in Figure 3.8. When another slice needs to be acquired, the gradient is adjusted so that the null level is at the physical position of the wanted slice. Usually applied in the z direction in order to acquire axial images, the slice selection gradient can also be applied in the x or y direction for the acquisition of sagittal and coronal images⁶².

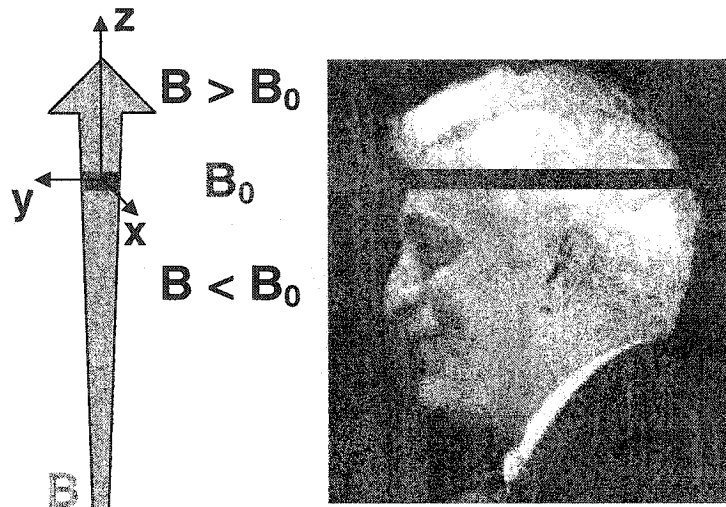


Figure 3.8: Slice selection by a magnetic field gradient.

In order to select an axial slice, a magnetic field gradient is added in the z -axis. It adds or subtracts to the static magnetic field B_0 , leaving only a thin region with an unchanged magnetic field strength and a Larmor frequency close to ω_0 , the excitation pulse frequency. Using this profile of Dr. Richard Damadian, the founder of MRI, the corresponding selected slice is shown.

If a gradient G_x is applied when the echo is acquired, the signal received will be a combination of the signals of each voxel along the x direction but with a slightly different frequency for each x position. In other words, the frequency encoding represents the spatial distribution in the x direction.

If a gradient G_y is applied for a given time between the excitation pulse and the acquisition echo, the nuclei will be given a phase encoding, which varies with their y position. For the subsequent excitation at the selected slice, the strength of the gradient G_y is incremented, which leads to a different amount of phase warping⁶³. In order to separate the image into 256 pixels in the y direction, 256 excitations with different G_y gradient strengths are needed.

3.3.1.2 Fourier space and 2D Fourier Transform

Instead of being acquired continuously, the signal measured after an excitation pulse is sampled. If a 256x256 matrix image is desired, the signal will be sampled 256 times, and the acquisition sequence repeated 256 times with increasing phase warping. The equally spaced data points acquired in one repetition sequence have the same phase but their frequency varies. In Fourier space, also called k -space, where frequency is k_x and phase is k_y , these points would fill out one row. Repeating the sequence, while incrementing the strength of G_y , will fill the k -space row after row with data points. Once the k -space is sufficiently sampled, a 2D Fourier Transform (FT) is applied to the data and yields the desired 256x256 object-space image.

Figure 3.9 shows an MR image of the brain and the corresponding k -space. In k -space, contrast is represented by low spatial frequencies, which can be found in the center of the k -space image, while detail is represented by high spatial frequencies, towards the ends of the k_x axis.

3.3.2 Multislice spin echo imaging

In most spin echo acquisition sequences, the repetition time, TR, is much longer than the echo time TE to allow for longitudinal relaxation, and can be as long as a few seconds. If many slices are required to image the volume of interest, the total imaging time can be exceedingly long. In order to reduce the scanning time, a non-contiguous slice is excited right after the echo acquisition of the initial slice. A set of non-contiguous slices is excited one after the other until TR for the first slice has elapsed. The set of slices is then excited with an increasing phase-encoding to yield another line in k -space. When the k -space is filled for those slices, another set of slices is acquired.

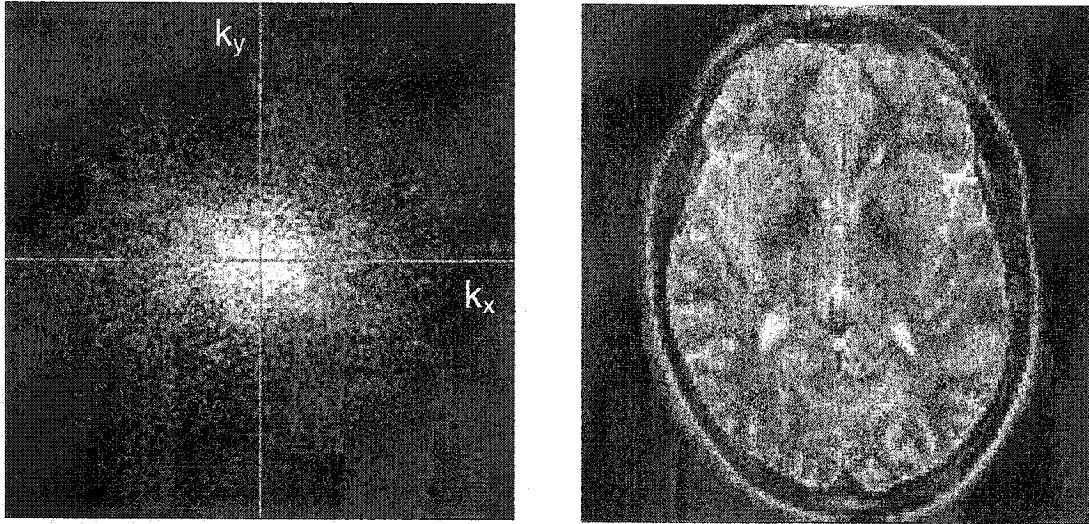


Figure 3.9: k-space and corresponding axial MR image of brain.

This figure shows the acquired data in k-space, from which an MR image of the brain can be reconstructed⁶⁴.

Although multiple slices may be acquired simultaneously, the process may still be time consuming when a large number of slices are required. In the work presented in this thesis, approximately 60 slices are acquired twice, first at TR 500 ms, then at TR 1500 ms, using multiple excitations to increase the signal-to-noise ratio. The need for these two image sets will be explained in section 3.3.5. Using these scanning conditions, the overall MR scanning time is around two hours. When including the time needed to irradiate the phantom and realign it in the MR scanner, the time limit of two hours (section 2.5.5) for the Fricke-gel dosimeter is exceeded. One way around this would be to increase the thickness of the slices, thus reducing the number of slices and the resolution of the dosimeter in the z-direction. Another way would be to limit the imaging to the section irradiated.

Since regions of gel receiving low or no doses are as important as the irradiated regions in order to produce complete dose-volume histograms, an alternate imaging technique is required.

3.3.3 Fast spin echo imaging

Fast spin echo imaging provides a faster way to obtain all the needed slices. In this sequence, not only are multiple slices successively excited within the time TR, but multiple k-space lines are also acquired for each slice. Figure 3.10 shows how the phase encoding

gradient is applied after each 180° pulse with an increasing strength, making each echo signal correspond to a different phase section of k -space. The strongest first echo fills the central portion of k -space (a) and the subsequent echoes fill sections above and below the central part, moving away the increasing gradient strength. The overall imaging time is reduced from over two hours to less than 40 minutes. Such a reduction in imaging time has the advantage of reducing the diffusion in the gel and preserves the sharp dose gradients experienced in conformal radiation therapy and IMRT.

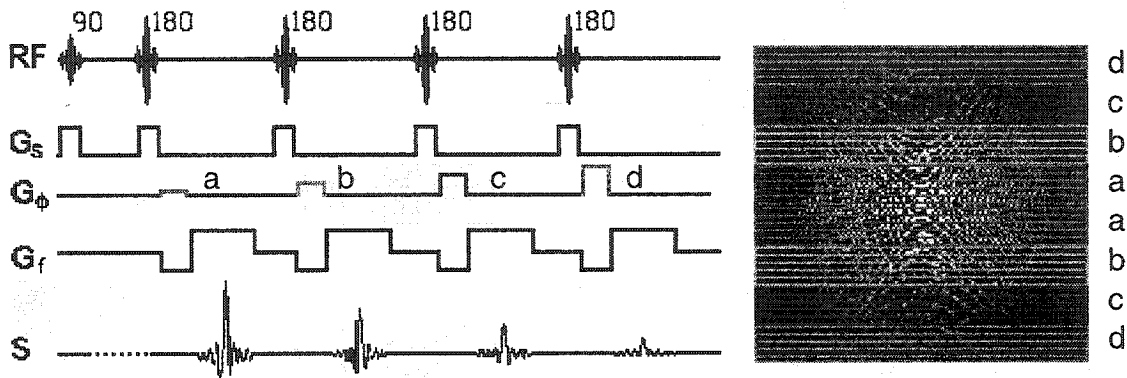


Figure 3.10: Fast spin-echo sequence with four echoes and corresponding k -space. Each echo, due to increasing phase gradient G_ϕ , fills a different part of the k -space. The gradient indices refer to the slice (s), phase (ϕ) and frequency (f) selection gradients. (Used with permission⁶⁵.)

3.3.4 Weighted images (proton density, T_1 , T_2)

The contrast of images produced by a given sequence is affected by T_1 and T_2 relaxation times as well as by the proton density (see equation 3.4). These are intrinsic characteristics of the tissues. TR and TE are among many adjustable parameters that can influence the weighting of contrast.

In order to have an image contrast that is predominated by proton density, a long TR and a short TE are required. TR must be long enough ($TR > 5T_1$)⁶² in order for M_z to have recovered completely, while TE should be much shorter than the T_2 relaxation times of the tissues so that only negligible T_2 relaxation occurs before the echo⁶⁶.

A pulse sequence with a long TR and a sufficiently long TE ($TE \approx T_2$) will produce T_2 weighted images, where tissues with a long T_2 will have a stronger echo and appear brighter than their shorter T_2 counterparts.

Finally, a sequence with a very short TE and a sufficiently short TR will produce T_1 weighting, which produces image contrast dominated by T_1 and proton density. In this case, tissues with a short T_1 will have a stronger signal and appear brighter than their longer T_1 counterparts. An increase in R_1 , caused by an increase in dose, will therefore cause an increase in signal.

In this work, the dose measured in the gel dosimeter is proportional to both $1/T_1$ and $1/T_2$, with a higher sensitivity for T_2 than for T_1 . However, T_2 images require much longer TRs than T_1 images, and T_2 imaging times become prohibitively long. The T_2 signal level is also much lower.

Figure 3.11 shows the theoretical relationship between signal and dose, for various spin echo TE and TR combinations, thus demonstrating the possible proton, T_1 and T_2 weighting of the gel dosimeter images. T_1 and T_2 for each dose level were calculated using the R_1 sensitivity measured in this work ($0.03256 \text{ s}^{-1}\text{Gy}^{-1}$) and the R_2 sensitivity measured by Duzenli⁹ ($0.077 \text{ s}^{-1}\text{Gy}^{-1}$).

3.3.5 Two-point-ratio calculation of T_1 relaxation time

Using the two-point-ratio method presented by Bengtsson²¹ and modified by Knutsen²³, it is possible to remove the proton density dependence of the raw T_1 weighted images and obtain pure R_1 images. Two spin-echo images, acquired with the same echo time but with different repetition times, show a different amount of T_1 weighting. R_1 is then calculated pixel by pixel, using the signal ratio of the two images. Due to the very short TE used, the T_2 dependence can be removed.

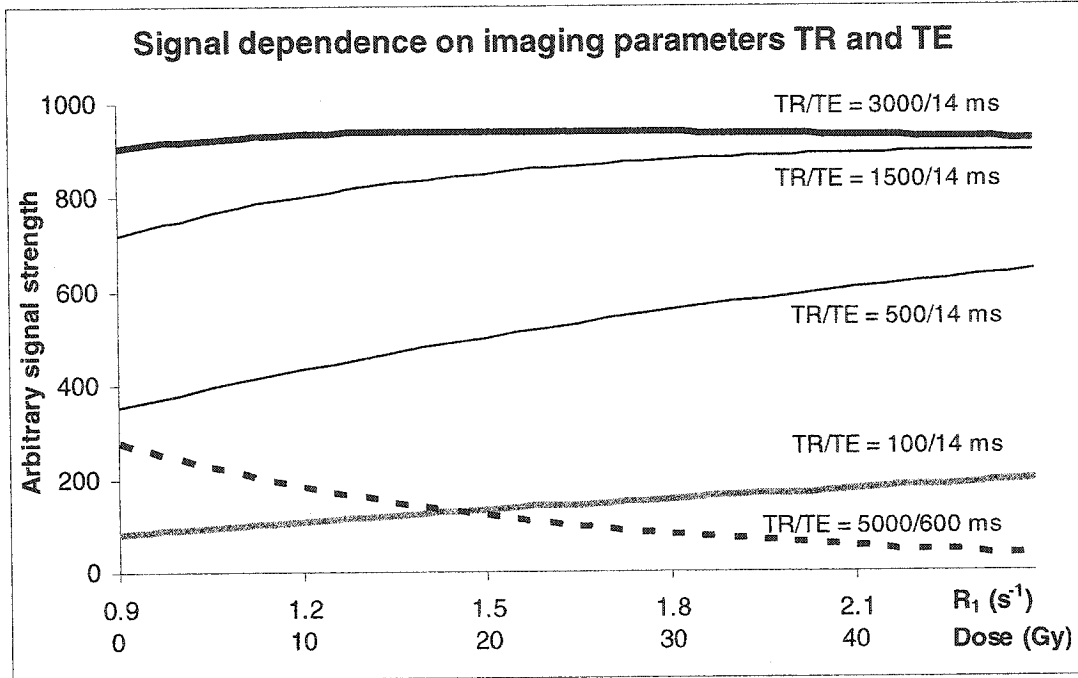


Figure 3.11: Calculated signal vs. dose curves for various imaging parameters. The dotted line represents T₂ weighting and the full lines show various levels of T₁ weighting, from heavy T₁ weighting (grey line) to heavy proton weighting (thick black line). The thin lines represent the expected MR signal response of the two sets of selected parameters in this thesis. R₁ values are those of the irradiated vials, before subtraction of the background.

The following equation, shows how the signals (S₁ and S₂) are related to R₁, the repetition times (TR₁ and TR₂) and to the echo time (TE). It is solved iteratively for R₁ until a precision of 0.0001% is reached⁶⁷.

$$\frac{S_1}{S_2} = \frac{1 - 2 \cdot \exp\left(-\left(\text{TR}_1 - \frac{\text{TE}}{2}\right) \cdot R_1\right) + \exp(-\text{TR}_1 \cdot R_1)}{1 - 2 \cdot \exp\left(-\left(\text{TR}_2 - \frac{\text{TE}}{2}\right) \cdot R_1\right) + \exp(-\text{TR}_2 \cdot R_1)} \quad 3.5$$

3.3.6 Noise and the signal-to-noise ratio (SNR)

The many sources of noise in an MR image can be divided into an instrumental category and an imaging sequence category. The magnetic fields **B**₀ and **B**₁, the coils and the receiver electronics are noise sources from the first category, while the data acquisition

time, spatial resolution and type of sequence used are noise sources from the second category. There is also imaging noise produced in the body of the examination subject.

The signal-to-noise ratio (SNR) is the ratio of the average image signal, \bar{S} , to the standard deviation of the background noise, σ , as seen in equation 3.6.

$$\text{SNR} = \frac{\bar{S}}{\sigma} \quad 3.6$$

In order to improve the SNR, many excitations are used to produce many images, which are then averaged to yield the final image. The SNR is proportional to the root of the number of excitations, NEX, used to obtain the average image⁶⁵. Note that the imaging time is proportional to NEX, so a reasonable NEX value must be used.

$$\text{SNR} \propto \sqrt{\text{NEX}} \quad 3.7$$

Using larger voxels would also improve the SNR, but at the detriment of spatial resolution, which is needed for the purpose of this work. The specific MRI parameters for the experiments in this thesis will be explained in the next chapter.

3.4 MRI instrumentation

The main components of instrumentation surrounding magnetic resonance imaging are the magnet, the magnetic field gradient coils, the radiofrequency system and the computer system. Figure 3.12 presents a picture of a clinical MR scanner with a headcoil in place (see section 3.4.4 in the following pages).

3.4.1 Magnet

In modern clinical MR units, a superconductive magnet creates the main magnetic field, B_0 . It has a large bore of approximately 1 meter in diameter, in which the patient is placed by a mechanized sliding couch. To maintain the usual field strength of 1.5 Tesla, the magnet coils must be cooled by liquid helium to a temperature of 4.3 Kelvin⁶², while the magnet bore is kept close to room temperature for the comfort of the patient.

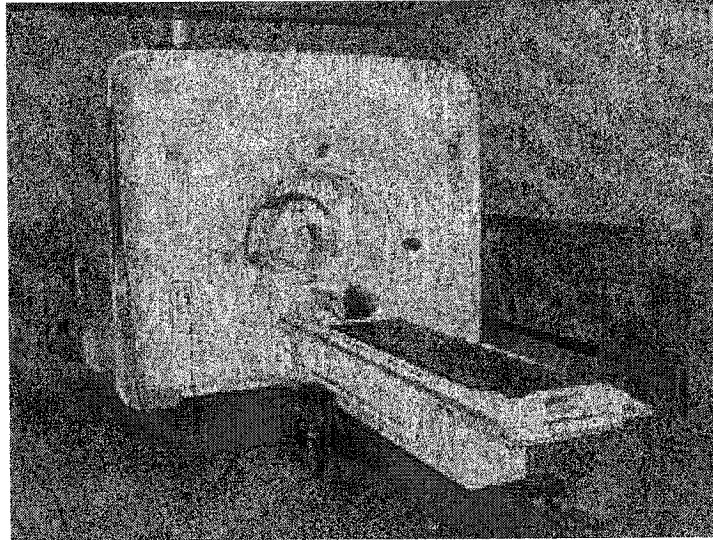


Figure 3.12: GE Signa MRI scanner with 1.5 T field.

3.4.2 Magnetic-field gradient coils

Three additional sets of coils are located between the superconducting magnet and the empty bore space. These produce gradients in the z , x and y directions that add or subtract to the main magnetic field. Any of these gradients can be used for slice selection, while the other two are used for frequency and phase encoding, allowing images to be acquired not only in the axial plane, but also in the sagittal and coronal planes. The gradients must be able to be ramped up and switched on and off very rapidly.

3.4.3 Radiofrequency system

This is the system that supplies the radiofrequency (RF) that excites the nuclear spins. It consists of a quartz-crystal oscillator which provides the RF, a modulator to obtain RF pulses of a predetermined bandwidth and a power amplifier. The RF system must be very stable and powerful while still allowing fine-tuning to match the RF to the resonant frequency of the sample. It is located inside the magnet bore, between the gradient coils and the patient.

3.4.4 Transmit and receiver coils

The body coil and the head coil used in the MR scanner both transmit the RF and receive the signal from the sample. The body coil is the only one always present in the scanner because it is located between the gradient coils and the interior wall of the magnet core. A large selection of surface coils exists in order to place the coil as close as possible to the region of interest to increase the signal-to-noise ratio. These coils are designed to receive only, while the body coil provides the RF. When used, the coils are secured on the couch and connected to the system in at the head of the couch. In this thesis, the various phantoms were placed in a head coil, which has birdcage geometry (Figure 3.13).

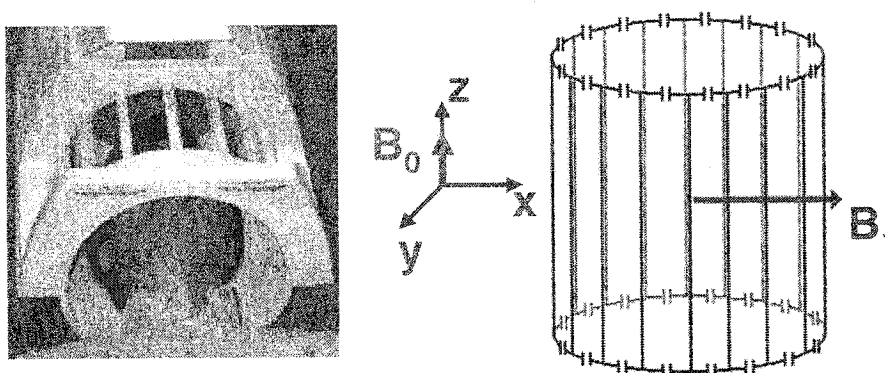


Figure 3.13: MRI head coil with birdcage geometry.

Being closer to the region of interest, this coil yields a higher signal-to-noise ratio and fewer geometric artefacts than the body coil. (Used with permission⁶⁵.)

3.4.5 Computer system

The MRI control console is the user end of the MRI computing system. It is used to input the patient information, select the imaging sequence and parameters and operate the MR scanner. The gradients and RF pulses are also controlled in the background by the computer, where it also processes the signal and performs Fourier Transforms to produce the diagnostic images. The different slices acquired can be viewed on the console, the windowing level can be adjusted and some image analysis tools are available. The computer system is also responsible for managing the image files and storing the patient data. Since the advent of powerful computers, MRI has developed into an important diagnostic tool.

Chapter Four

4 Methods and Materials

This chapter describes the experimental procedures used in this research. In the first section, details concerning the preparation of the gel phantoms, their irradiation and the magnetic resonance imaging are given. The treatment planning system and the tools used to extract the dose distribution from the MR images are also described. The second section describes the specifics of each experiment in detail.

4.1 General experimental procedures

4.1.1 Preparation of the gel

The dosimetric gel used in this research is both a phantom and a dosimeter in itself. During its preparation, it can be poured into plastic molds that mimic human body shapes, such as the head phantom, or simpler geometric shapes such as the box phantom. The dosimeter gel was prepared following the methods of Olsson⁵ and Hazle⁶ and consists of a Fricke solution mixed with 5% gelatin per weight. The first step of the procedure is to dissolve a pig skin gelatin (type A: 300 bloom, Aldrich Chemical Co., Milwaukee, WI) in distilled water (75% of the total water volume). To do this, the gelatin is slowly added to the constantly stirred water that is under heating. When the gelatin is completely dissolved, the gel is transparent and yellow in color. The gel is heated to 45°C, at which time all the

gelatin has dissolved. The gel is then cooled until it reaches a temperature of about 40°C. The cooling time can take a few hours when 4 L of dosimetric gel is prepared (box phantom or head phantom). The gel is stirred continuously throughout the entire heating and cooling processes.

While the gel is cooling, the ferrous sulphate solution is prepared in a separate beaker containing the remaining 25% of the total water volume. One mM NaCl (reagent grade, Aldrich), 1 mM ferrous ammonium sulfate hexahydrate (99+% purity, Aldrich) and 0.05 M sulphuric acid (reagent grade, Aldrich) are added. A darkening hood is placed over the beaker and the solution is stirred for fifteen minutes.

The Fricke solution is then slowly poured into the beaker containing the dissolved gel. The contents are stirred under a darkening hood for 30 minutes. The liquid gel is then poured into the selected phantom mold, which is subsequently sealed. The phantom is placed in a refrigerator for about 12 hours in order for the gelation process to occur. The filled phantom is then put in a closed cardboard box at room temperature for 14 to 16 hours, allowing the gel to return to room temperature.

4.1.2 Selection of phantoms

Since the radiation beam passes through the phantom wall, it is important that the phantom walls are made of a water-equivalent plastic. Polymethylmethacrylate (PMMA), also known as acrylic or Lucite®, was chosen as the phantom wall material because its radiological properties are well known.

Material	Composition	Z_{eff}	ρ (kg/m ³)	ρ_e^w
Water	H ₂ O	7.51	1000	1.000
Fricke-gel	H ₂ O, gelatin, FeSO ₄ :6H ₂ O, H ₂ SO ₄ , NaCl	7.56	1005	1.004
PMMA	C ₅ H ₈ O ₂	6.56	1180	0.972

Table 4.1: Radiological properties of water, Fricke-gel and PMMA.

This table presents the chemical composition, effective atomic number, density and relative electronic density for water, Fricke-gel and PMMA. Fricke-gel is composed of water, gelatine, ferrous ammonium sulphate hexahydrate, sulphuric acid and NaCl.

The vials used in the dose-response experiments were machine-tooled out of Lucite® rods and sealed with paraffin. The 16.5 x 16.5 x 15.75 cm³ box phantom and lid were assembled from 3 mm thick Lucite® sheets. Crosshairs indicating the center of the box were also etched on all sides. A hollow transparent mold of the Rando phantom's head (The Phantom Laboratory, Salem, New York) was created by vacuum-molding a 3 mm acrylic sheet. A plastic and rubber plug was used to seal the filling hole of its baseplate. In all cases, the gel had to be well sealed within the phantom to avoid oxygenation, which could have affected the gel dose response⁹. The various phantoms are shown in Figure 4.1.

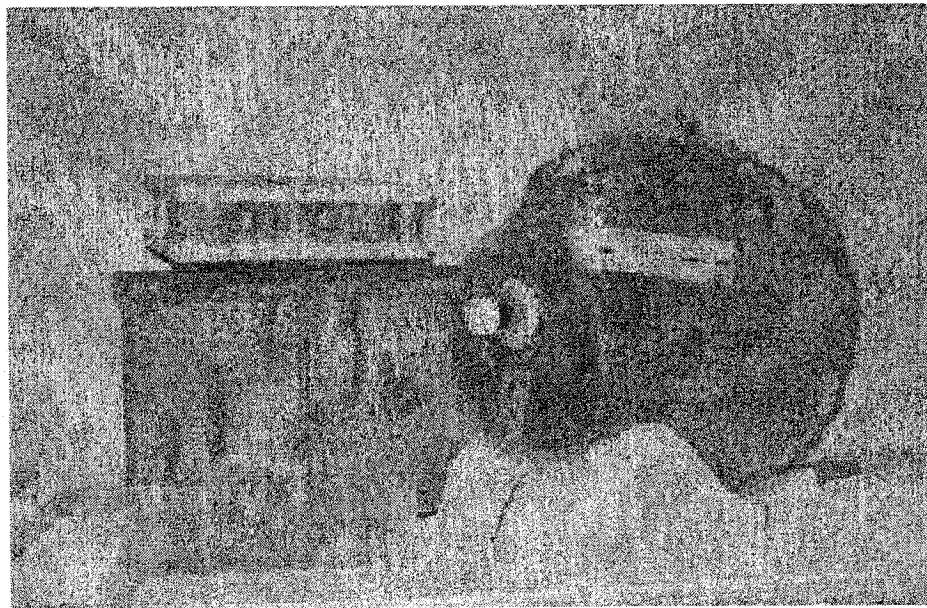


Figure 4.1: Vials, box phantom and head phantom.

Six vials are in front with six more in the MRI immobilization jig. The lid, etched crosshairs and taped fiducial markers are visible on the box phantom. Fiducial markers and alignment guidelines can also be seen on the gel-filled head phantom, which is on a typical treatment headrest.

4.1.3 CT imaging and treatment planning

Prior to preparing the gel, the chosen phantom was filled with water and taken to the CT-simulator suite. In order to create the treatment plan, the water-filled phantom was CT scanned with fiducial markers that determined the reference frame of origin. They were also used to align the phantom in the linac treatment room and to register the CT and MR images. The CT markers were made from radio-opaque plastic catheters. After the

treatment plan was calculated, the water inside the phantom was replaced with the dosimetric gel and the CT markers were replaced by MR fiducial markers. These consisted of sealed catheter tubing filled with a standard copper sulphate solution. The CuSO_4 solution was chosen because it produces a strong MR signal, making the small MR markers visible on both the raw images and the R_1 processed images.

Once the CT images had been acquired on the AcQSim CT-simulator (Philips, Cleveland, Ohio), the images were transferred to an AcQSim workstation where the contours of the target and the critical organs were drawn on the CT of the water-filled phantom mold. In the case of the Corvus IMRT experiment, anatomically correct contours were drawn directly on the CT information of the Rando head phantom. The contoured images were then transferred to the treatment planning station where a plan was formulated and the dose distribution was calculated. A commercial treatment planning system CadPlan (Varian, Palo Alto, California) was used to plan and obtain a dose distribution for the forward-planned experiments.

The two IMRT planning systems used at the McGill University Health Center are Corvus (NOMOS, Sewickley, Pennsylvania) and Helios (Varian Associates, Palo Alto, California). Corvus uses a pencil-beam algorithm and a fine dose calculation matrix. Its objective function is a DVH-based cost function, and for optimisation it relies on a hybrid between simulated annealing and gradient search. On the other hand, Helios uses a variation of the downhill gradient method with a DVH-based cost function. Both systems produce plans that can be delivered by either dynamic MLC or the step-and-shoot method. The dose distribution, the contours and the CT information are later retrieved and sent to a computer for further analysis.

4.1.4 Linac irradiation

The gel dosimeters were irradiated using 6 MV photons, from one of three Varian linear accelerators (Varian Associates, Palo Alto, California) found at the Montreal General Hospital (McGill University Health Center) Radiation Oncology department. These linacs, a Varian Clinac 2300CD, a Varian Clinac 6EX and a Varian Clinac 21EX, are equipped

wih 120-leaf Millenium multileaf collimators (MLC), capable of IMRT, by either the step-and-shoot method or the dynamic MLC method. The beam can be wedged by either inserting a static wedge below the linac head, or by using the enhanced dynamic wedge mode, whereby a moving jaw creates a wedged beam profile.

For each experiment, the dosimeter was aligned on the linac isocenter using the room lasers, either with a source-surface distance (SSD) of 100 cm or a source-axis distance (SAD) of 100 cm. The SSD setup was used in the preliminary experiments validating the gel dosimeter, while the SAD setup was used for the more complex beam geometries used in the forward-planned and inverse-planned 3D dose distribution experiments.

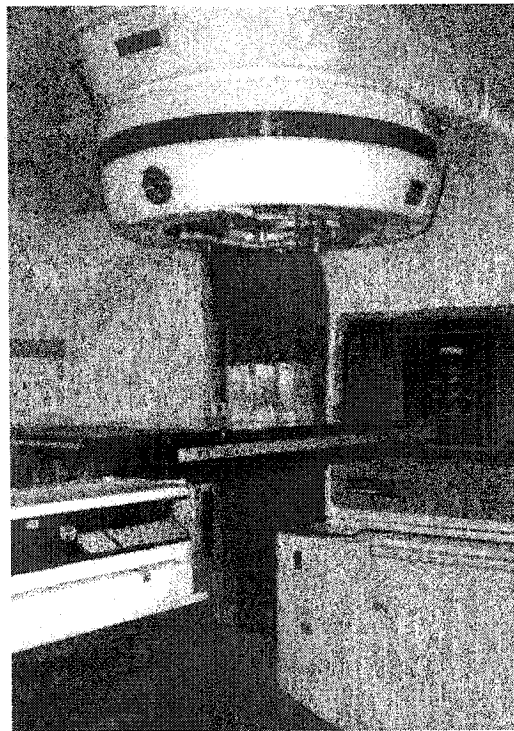


Figure 4.2: Linac setup of box phantom.

The box phantom sits in position on the treatment couch of the Varian Clinac 2300C/D.

4.1.5 MR scanning

The MR-scanning was performed on a 1.5 T (64 MHz) GE Signa MRI-scanner (GE Medical Systems, Waukesha, Wisconsin). The phantoms were imaged using the head coil to transmit and receive the signal. All imaging was done using a 2D multi-slice fast spin

echo sequence. The imaging parameters, shown in Table 4.2, were chosen in order to minimize the imaging time while maximizing the signal-to-noise ratio. The phantoms were imaged twice, first with a repetition time (TR) of 500 ms and then with TR = 1500 ms, in order to calculate the spin-lattice relaxation rate R_1 .

Imaging parameters	1 st sequence	2 nd sequence
Technique	Fast spin echo	Fast spin echo
Repetition time (TR)	500 ms	1500 ms
Effective echo time (TE)	14 ms	14 ms
Number of echoes (ETL)	4	4
Number of excitations (NEX)	4	4
Field of view (FOV)	48x48 cm ²	48x48 cm ²
Matrix size	256x256	256x256
Pixel size	1.875 mm	1.875 mm
Slice thickness	3 mm	3 mm

Table 4.2: Gel dosimeter MRI scanning parameters.

Scans at both repetition times (TR) were acquired before the irradiation and immediately following it. The R_1 images were calculated separately for pre- and post-irradiation situations, and then the background (initial) R_1 image was subtracted from the irradiation R_1 image, in order to reduce the MR-induced image nonuniformities. The resulting images have R_1 values ranging from 0 to 1.5 s⁻¹.

4.1.6 Data analysis and relative dose distributions

The R_1 image extraction and data analysis were carried out on a desktop PC using the image manipulation software AVS 5.4 (Advanced Visual Systems, Waltham, Massachusetts), operating under Linux SuSE 7.0 (SuSE Inc., Oakland, California).

In the dose range where dose and R_1 are proportional, the R_1 image can be normalized to a given dose value at a known position (d_{\max} on the central axis for SSD experiments, or the isocenter for SAD experiments), thus becoming a relative dose

distribution. Percent-depth-doses (PDDs) and off-axis ratios (OARs or profiles) can be extracted from single beam experiments, and this information can be compared to PDDs and OARs obtained with other types of dosimeters, in order to validate the gel dosimeter. To compare the 3D dose distribution measured by the gel dosimeter to the TPS planned distribution, the two sets of data must first be registered and fused.

4.1.7 Registration and fusion

The fiducial markers that appear on both the MR and CT images of the gel phantom are used to register the MR dose information with the CadPlan data set, which includes the CT images, the contours and the calculated dose distribution. One set of data is then fused to the other, using software developed by Bercier⁶⁸ and described by Bélanger⁶⁹. This allows the superposition of CT-defined contours on the MR dose image, and the superposition of the actual delivered dose (as measured by gel dosimetry) onto the CT anatomical information.

4.1.8 Dose-volume histograms

The fused CadPlan contours and the MR dose distribution are used to generate dose-volume histograms (DVH) for the target, margins, structures “at risk” and whole body. These gel-measured DVHs can then be compared to the DVHs computed by the treatment planning software. The mean, minimum and maximum doses for each contour were also computed and compared to the treatment planning system contour statistics.

4.2 Experiments

4.2.1 Vials

In order to obtain a dose-response curve, 15 mL vials were irradiated to 0, 10, 20, 30, 40 and 50 Gy and imaged together. After the R_1 calculation and background subtraction, regions-of-interest were selected on the resulting image and R_1 values for each dose level were obtained and plotted. From this, the dose-response range and sensitivity of the gel dosimeter can be established.

Since only 90 mL were needed to fill the six vials, the Fricke-gel was prepared in a large batch, with most of the gel filling one of the large volume phantoms for another experiment. For the pre- and post-irradiation MR imaging, the six vials were placed in an immobilisation jig. The jig was put in the box otherwise used as the box phantom, and this box was filled with water, in order to minimize interface effects and artifacts at the periphery of the vials. With similar weight, volume and water composition, the imaging conditions of the vials were then similar to those of the other experiments.

For the irradiation on the Varian 2300C/D linac, three vials at a time were put in a box filled with water in such a way that the vial centres were at 1.5 cm from the side of the water-equivalent Lucite box (Figure 4.3). Solid water surrounded the box to provide sufficient scatter. With the linac gantry at 90°, the side of the box was put at 100 cm from the source and a sufficiently large field size was used in order to cover the vials and the water phantom. This put the vial centres at the depth of dose maximum for the 6 MV irradiation photon beam. The vials were irradiated to doses of 10, 20, 30, 40 and 50 Gy.

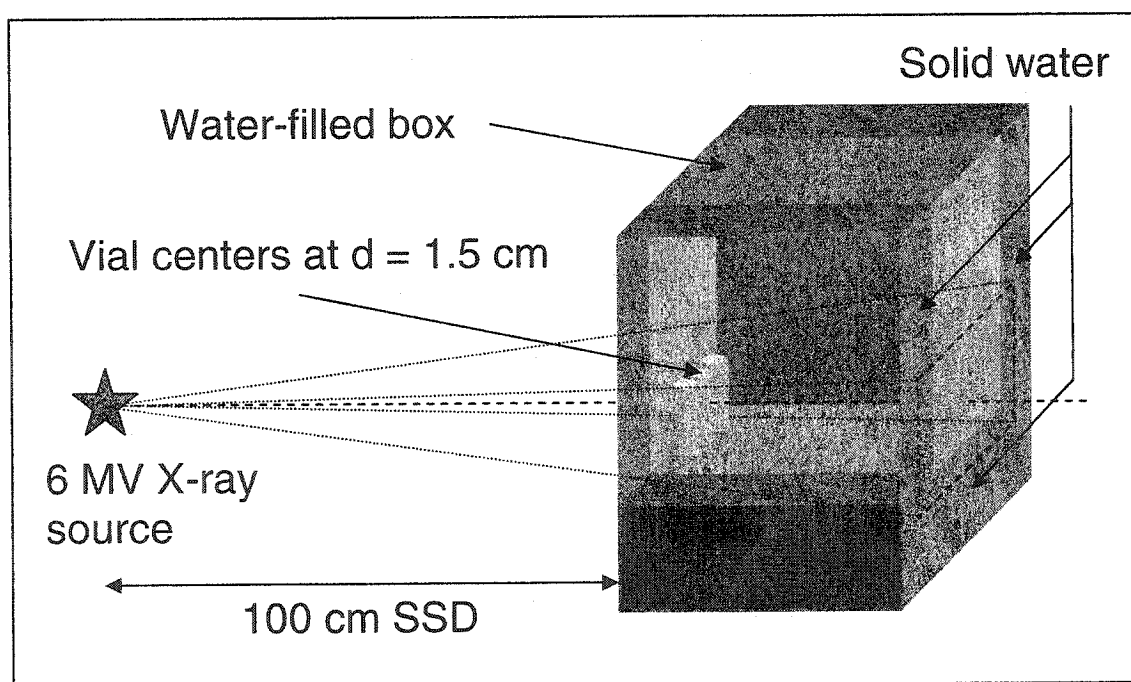


Figure 4.3: Diagram showing the irradiation setup of the vials.

The vials were contained in a water-filled box, surrounded on three sides by solid water to provide full scatter conditions.

4.2.2 Open and wedged beam PDDs and profiles

For the pre- and post-irradiation MR scanning, the box phantom alone was aligned using the centering lights and the etched crosshairs. The MR acquisition covered the whole phantom and yielded 57 slices. For both the open beam and wedged beam experiments, the gel-filled box phantom was setup on the Varian 2300C/D linac at a source-to-surface distance (SSD) of 100 cm. The box was centered on the beam axis using the room lasers and the etched crosshairs. For the first experiment, the box was irradiated with a 6 MV 10x10cm² open beam, the field size being defined at the surface. At that time, the linac output, as per TG-51⁷⁰, was 101.6 cGy / 100 MUs. 3445 MUs were needed for a dose at d_{\max} of 35 Gy. For the second experiment, the phantom was irradiated with a similar setup, but using a 60° external static wedge, which a wedge factor of 0.403 (ratio of doses with and without the wedge). At that time, the linac output, as per TG-51⁷⁰, was 100.5 cGy / 100 MUs. 6173 MUs were needed for a dose at d_{\max} of 25 Gy, and the wedge hotspot received approximately 35 Gy. Percent depth dose (PDD) curves and off-axis ratio (OAR) profiles at depths of 1.5 cm (d_{\max}) and 9.5 cm were extracted for both cases. The setup for the open and wedged field experiments may be seen in Figure 4.4.

4.2.3 Forward-planned box phantom

The water-filled box phantom was first CT-scanned with fiducial markers in place. The external contour was automatically obtained and an arbitrary cubic target (GTV, see section 1.2) was drawn approximately centered on the reference isocenter. Additional contours with a 1 cm margin were added in order to represent the CTV, PTV and PTV2. Since the 3D CadPlan dose matrix consists of a set of 2D dose matrixes, which are limited to 160 x 112 pixels⁷¹, using the 1.25 mm grid resolution causes the dose matrixes to be limited to an area of 20 x 14 cm². The treatment planning system dose calculation matrix therefore does not cover the whole external contour of the 16.5 x 16.5 x 15.75 cm³ box. Additionally, the TPS data is unreliable in the buildup region. An organ “External - margin” was therefore created for dose volume histogram calculations in order to resolve these issues. The organ consisted of the External contour minus a 1.5 cm margin to exclude the buildup data and the area not covered by the TPS dose matrix.

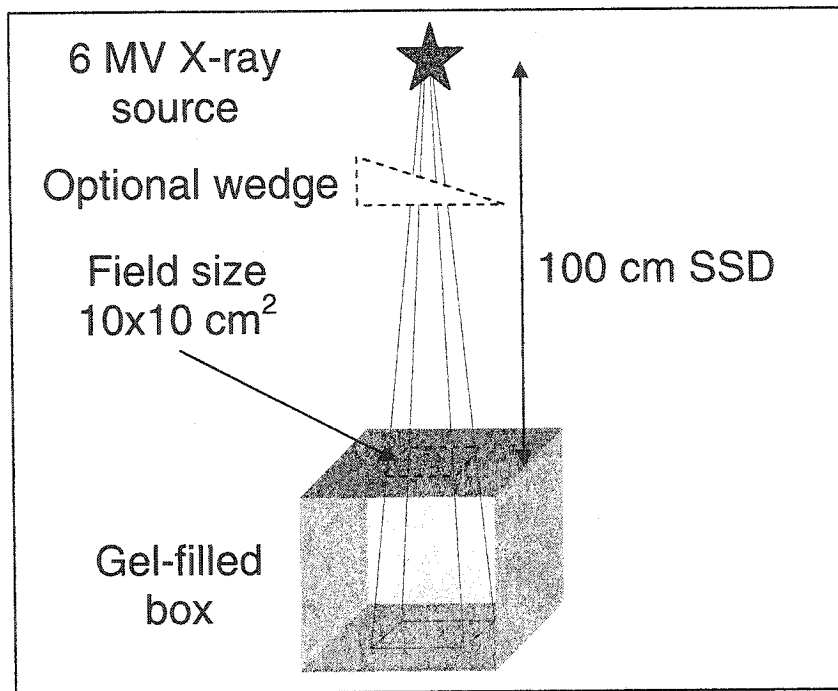


Figure 4.4: Diagram showing the irradiation setup for the PDDs and profiles.

The box phantom was directly aligned on the linac isocenter, at a source-to-axis (SAD) distance of 100 cm, using the room lasers. It was irradiated to 20 Gy at the isocenter with four 6 MV beams. The monitor units (MUs) were calculated by the treatment planning system and verified by hand. The beam parameters for this isocentric treatment plan can be found in Table 4.3, while Figure 4.5 shows a 3D view of the treatment planning beam setup. The box phantom was MR imaged using the same parameters as for the simple beam experiments.

Field	Gantry Angle (°)	Collim. Angle (°)	X field (cm)	Y field (cm)	Beam weight	SSD (cm)	MUs
1	0	0	5.0	5.0	1.0	92.2	632
2	90	0	5.0	5.0	1.0	91.9	632
3	180	0	5.0	5.0	1.0	92.2	632
4	270	0	5.0	5.0	1.0	91.8	632

Table 4.3: Forward-planned box phantom treatment parameters.

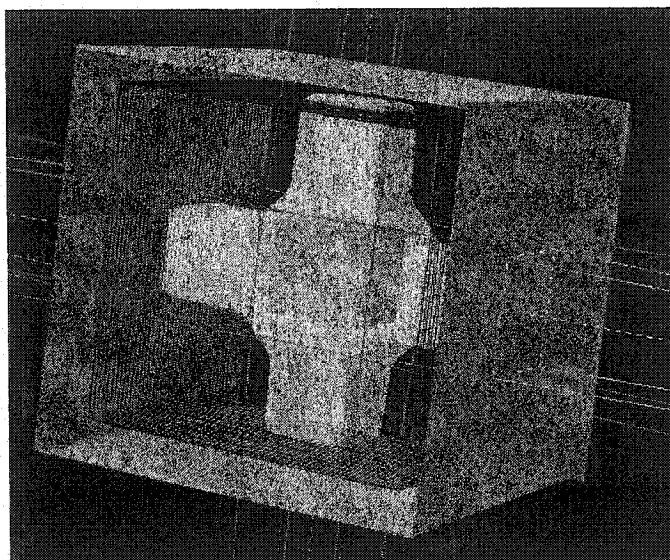


Figure 4.5: 3D treatment plan for the forward-planned box phantom.

This figure features the external (green), external-margin (blue) and target (red) contours, the 50% isodose surface (white), and the four beam directions.

4.2.4 Forward-planned head phantom

The water-filled head phantom was first CT-scanned with fiducial markers at the level of the nasion (where the nose meet the forehead). The external contour was automatically obtained and an arbitrary cylindrical target (GTV) was drawn and approximately centered on the reference isocenter. This may be seen in Figure 4.6. An additional contour with a 1 cm margin was added in order to represent the PTV. Contours were also added to represent critical structures such as the eyes and spinal cord. The external-margin structure was represented on the CT axial slices by ovals which were approximately 1.5 cm within the external contour. These ovals were also useful for the DVH comparison since the TPS dose calculation matrix did not extend fully to the external contour of the head phantom.

The head phantom, secured with a typical treatment headrest, was directly aligned on the Varian 6EX linac isocenter, at a source-to-axis (SAD) distance of 100 cm, using the room lasers and the fiducial markers. It was irradiated to 20 Gy at the isocenter with three 6 MV beams, two of which were dynamically wedged. The beam parameters may be found in Table 4.4, while Figure 4.7 shows a 3D view of the treatment planning beam setup.

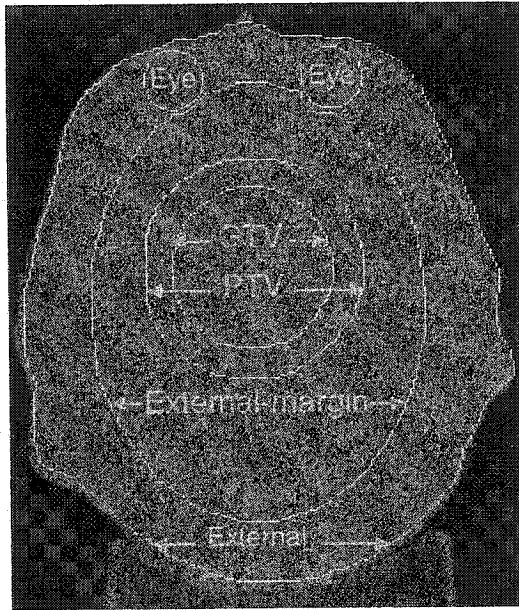


Figure 4.6: Head phantom CT and user-defined planning contours.

Field	Gantry Angle (°)	Collim. Angle (°)	X field (cm)	Y field (cm)	Dyn. wedge angle (°)	SSD (cm)	MUs
1	0	90	6.2	5.4	0	91.8	825
2	90	90	6.2	5.4	30 (OUT)	92.6	903
3	270	90	6.2	5.4	30 (IN)	91.7	903

Table 4.4: Forward-planned head phantom treatment parameters.

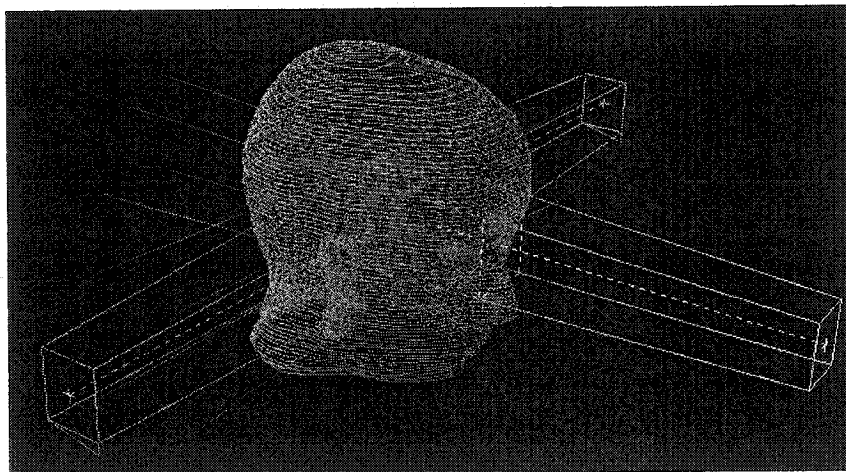


Figure 4.7: 3D treatment plan for the forward-planned head phantom.

This figure features the external (green), target (red) contours, as well as the eyes and cord (pink) and the three beam directions.

4.2.5 Helios IMRT inverse-planned head phantom

Using the same CT images and contours as for the forward-planned head phantom experiment (section 4.2.4), an IMRT plan was inverse-planned using Helios (Varian). The plan was designed to give a uniform 20 Gy dose to the GTV and a boost to the surrounding PTV to 24 Gy, by using five dynamic MLC fields with gantry angles 72° apart. The calculated fluence for each beam was transformed into deliverable dynamic MLC leaf sequences and the resulting dose distribution was calculated by CadPlan.

The head phantom, placed on a headrest, was directly aligned on the Varian 2300C/D linac isocenter, at a source-to-axis (SAD) distance of 100 cm, using the room lasers and the fiducial markers. It was irradiated to 20 Gy at the isocenter with five dynamic MLC 6 MV beams. The beam parameters for this isocentric treatment plan may be found in Table 4.5, while Figure 4.8 shows a 3D view of the treatment planning beam setup.

Field	Gantry Angle (°)	Collim. Angle (°)	X field (cm)		Y field (cm)	Beam weight	MUs
			X ₂	X ₁			
1	0	0	5.1	5.3	10.4	0.4969	4404
2	72	0	5.4	5.1	10.4	0.4153	3141
3	144	0	5.3	5.1	10.4	0.4819	3508
4	216	0	5.2	5.2	10.4	0.4963	3878
5	288	0	5.1	5.4	10.4	0.4664	3746

Table 4.5: Helios IMRT inverse-planned head phantom treatment parameters.

4.2.6 Corvus IMRT inverse-planned head phantom

The location of fiducial markers was first determined on the Rando anthropomorphic phantom head, and then transferred to the vacuum-molded face mask and gel mould. The phantom head was secured with a typical treatment headrest and was CT-scanned with CT and MR visible fiducial markers on the face mask. The isocenter was at the level of the nasion.

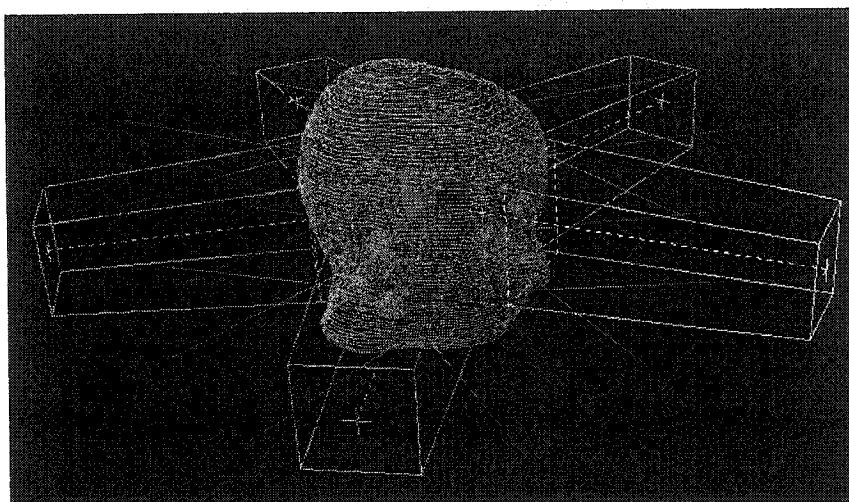


Figure 4.8: 3D treatment plan for the Helios IMRT inverse-planned head phantom. This figure features the external (green) and target (red) contours, as well as the eyes and spinal cord (pink) and the five beam directions.

The external contour of the Rando head was automatically obtained and an arbitrary cylindrical target (GTV) was drawn and approximately centered on the reference isocenter. An additional contour was added in order to represent the PTV and anatomically correct contours of the left eye and brain were also defined. The CT images and contours were then exported to the Corvus inverse treatment planning system, where a step-and-shoot IMRT plan was calculated.

The GTV clinical goals were a minimum dose of 23 Gy, a maximum dose of 24 Gy with only 5% of the volume allowed below the 24 Gy goal. The PTV clinical goals were a minimum dose of 17 Gy, a maximum dose of 19 Gy with only 5% of the volume allowed below the 18 Gy goal. The brain had a 19 Gy limit, with only 10% of the volume allowed to reach 24 Gy. The left eye had a 2 Gy limit, with 50% of the volume allowed to reach 5 Gy. The treatment plan was normalized to 24 Gy at the 86.9% isodose line.

The gel-filled Rando head mold, was MR scanned using the same parameters as for the previous experiments. The head phantom, was directly aligned on the Varian 2100EX linac isocenter, at a source-to-axis (SAD) distance of 100 cm, using the room lasers and the fiducial markers. It was irradiated with five step-and-shoot DMLC 6 MV beams. The beam parameters for this isocentric treatment plan (Figure 4.9) may be found in Table 4.6.

Field	Gantry Angle (°)	Collim. Angle (°)	X field (cm)		Y field (cm)		MUs Delivered
			X ₂	X ₁	Y ₂	Y ₁	
1	0	0	3.8	4.8	3.1	3.1	1419
2	325	0	3.8	4.8	3.1	3.1	1953
3	250	0	4.8	3.8	3.1	3.1	1297
4	35	0	3.8	4.8	2.6	3.1	1377
5	110	0	4.8	4.8	3.1	3.1	2039

Table 4.6: Corvus IMRT inverse-planned head phantom treatment parameters.

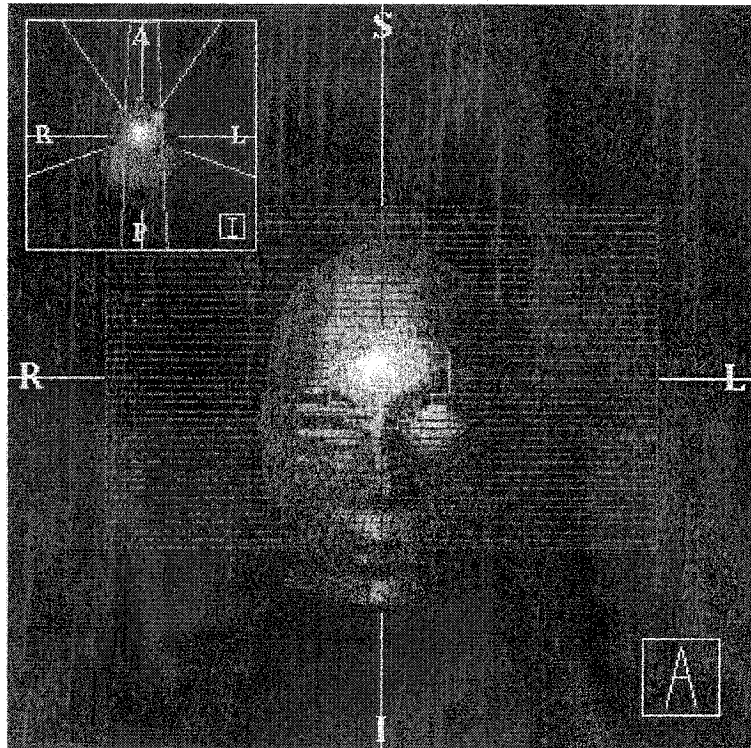


Figure 4.9: Corvus BEV of anterior field with insert showing all field directions (yellow) in axial plane.

Chapter Five

5 Results and Discussion

This chapter presents the experimental results obtained in this research. The gel dosimeter is first validated as a 3D integrating dosimeter by comparing it to other dosimetric tools, and 3D relative dose distributions for complex irradiations are then measured and dose-volume histograms obtained.

5.1 Validation of the gel dosimeter

5.1.1 Characteristics of the gel dosimeter

The characteristics of the gel dosimeter were investigated by irradiating gel filled vials. The raw MR images through the cross-section of the vials using different repetition times ($TR = 500$ ms and 1500 ms) are shown in Figure 5.1 (a and b). The relaxation rate image (Figure 5.1 c) was calculated from these two raw images, on a pixel-by-pixel basis, using equation 3.5.

Figure 5.2 shows relaxation rate images of the vials, before and after irradiation, and the resulting image after subtracting the pre-irradiation image from the post-irradiation image. The increase in pixel intensity due to increasing dose can be linearly correlated in the image shown in c).

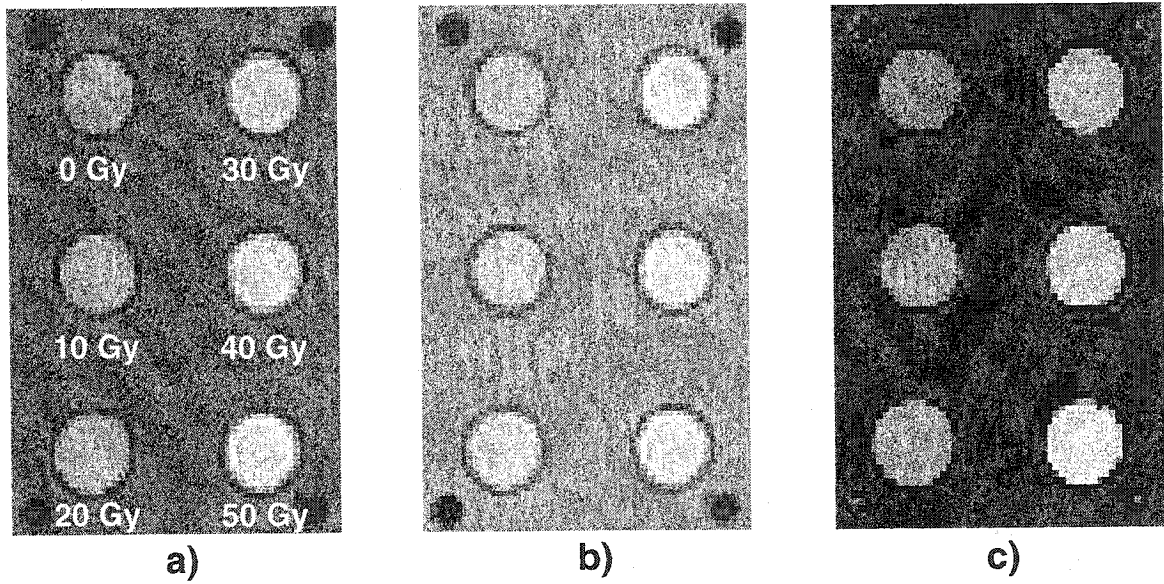


Figure 5.1: Raw MR images of the irradiated vials.
 a) imaged at TR = 500 ms, b) TR = 1500 ms and c) the calculated relaxation rate image of the irradiated vials.

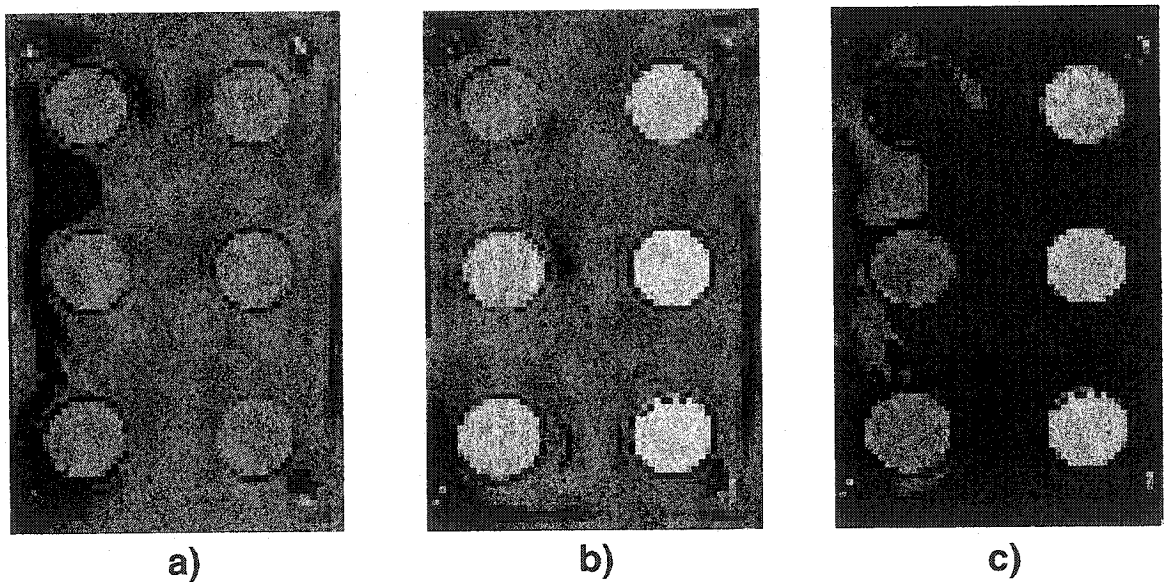


Figure 5.2: Calculated R_1 images of the irradiated vials.
 Imaged a) pre-irradiation, b) post-irradiation and c) after subtraction.

The increase in raw MR signal intensity may be seen numerically in Table 5.1 and graphically in Figure 5.3. The relationship between raw signal at TR = 1500 ms and dose was not linear, but once the relaxation rates were calculated, this dosimeter showed a linear dose response in the 0 to 40 Gy interval, with $r^2 = 0.9985$. Figure 5.3 also shows that

beyond 40 Gy, the dosimeter response begins to saturate. The sensitivity of the gel, which is the slope of the line, was measured to be $0.03256 \text{ s}^{-1}\text{Gy}^{-1}$. Using this sensitivity, measured doses were calculated from the MR measured longitudinal relaxation rates (Table 5.1). They are within 0.8 Gy of the given dose in the 0 to 40 Gy interval. As the dose increases, the MR dynamic range gets smaller, which leads to higher absolute uncertainties.

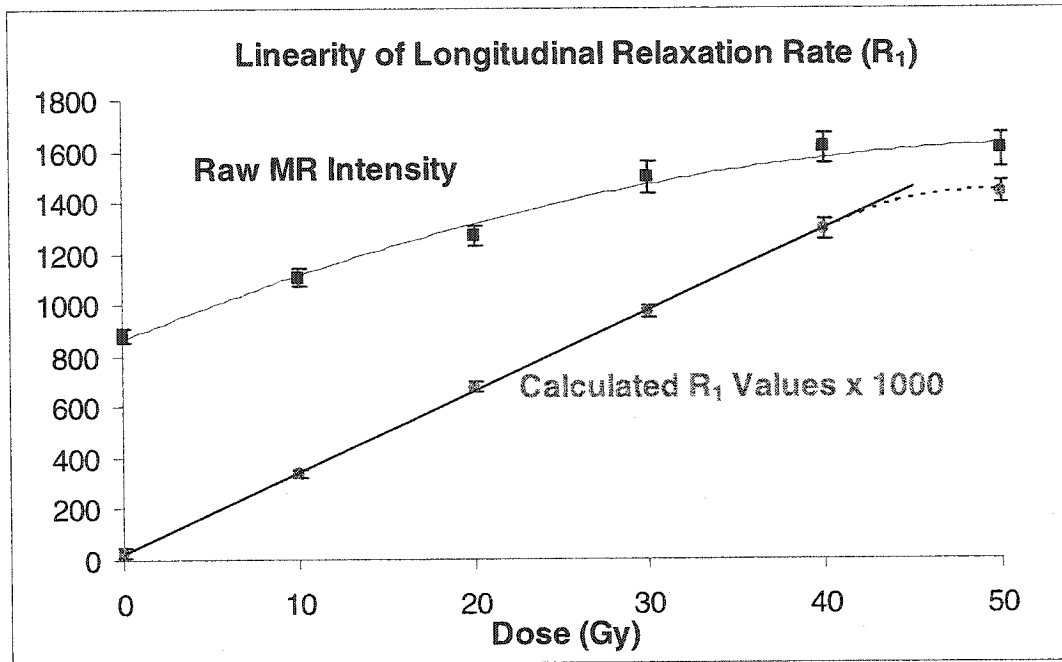


Figure 5.3: Raw MR signal intensity and R_1 values as a function of dose. This graph shows the raw MR signal intensity at TR = 1500 ms and the calculated R_1 values, both as a function of dose.

Given dose (Gy)	Raw MR signal ($\pm 1 \sigma$)	R_1 after subtraction ($\text{s}^{-1} \pm 1 \sigma$)	Measured dose ($R_1 / \text{sensitivity}$) (Gy $\pm 2 \sigma$)
0	879 ± 28	0.025 ± 0.021	0.8 ± 1.3
10	1106 ± 36	0.335 ± 0.018	10.3 ± 1.1
20	1270 ± 40	0.677 ± 0.019	20.8 ± 1.1
30	1496 ± 62	0.972 ± 0.025	29.9 ± 1.6
40	1610 ± 60	1.291 ± 0.038	39.6 ± 2.3
50	1601 ± 64	1.435 ± 0.044	44.1 ± 2.7

Table 5.1: Raw MR signal, R_1 and measured dose for various irradiation doses.

The reproducibility of the MR measurement and R_1 calculation was performed with five acquisitions of a 3 mm thick slice of a beaker containing the unirradiated gel dosimeter, made from the same batch of gel as the vials.

A region-of-interest (ROI) of 36 x 36 pixels (6.75 cm x 6.75 cm) was selected at the same location on each of the five images, and the standard deviation between the five R_1 images was calculated for each pixel individually and for the ROIs.

The gel dosimeter characteristics at 0 Gy were obtained by subtracting an unirradiated beaker R_1 image from another in order to calculate the uncertainty. The minimum detectable dose was three times the standard deviation at zero dose. The quotient of the mean and standard deviation gave the measured signal-to-noise ratio (SNR).

When the five reproducibility ROIs consisted of five vials irradiated to 20 Gy and imaged together, the reproducibility at 20 Gy and the uncertainty were calculated. The sensitivity of this batch of gel was $0.03988 \text{ s}^{-1}\text{Gy}^{-1}$. The tabulated results may be found in Table 5.2. The reproducibility variation at 20 Gy is higher than at 0 Gy due to the additional irradiation procedure.

Gel dosimeter characteristics at 0 Gy		
Signal-to-noise ratio (SNR)	82.2	
Pixel reproducibility variation	2%	(95% confidence)
ROI reproducibility variation	0.8%	(95% confidence)
Uncertainty	0.75 Gy	(95% confidence)
Minimum detectable dose	1.12 Gy	
Gel dosimeter characteristics at 20 Gy		
ROI reproducibility variation	1.8%	(95% confidence)
Uncertainty	0.35 Gy	(95% confidence)

Table 5.2: MR statistics and gel dosimeter characteristics at 0 and 20 Gy.

5.1.2 Percent depth doses and profiles

The percent depth doses (PDDs) and off-axis ratios (OARs) for an open beam and a 60° static wedge beam were compared to commissioning measurements taken with an IC-10 ion chamber in a 3D water tank (Wellhöfer North America, Bartell, TN). For the gel dosimetry data, the longitudinal relaxation rates (R_1) were extracted from five 3 mm thick MR slices which were combined to obtain a single 15 mm thick slice on the central axis, perpendicular to the phantom surface. The data was then normalized to a relative dose of 100% at d_{\max} on the central axis, and PDDs and OARs (1.5 cm and 9.5 cm depth) were extracted. Figure 5.4 shows the R_1 maps and the locations of the PDD and profiles.

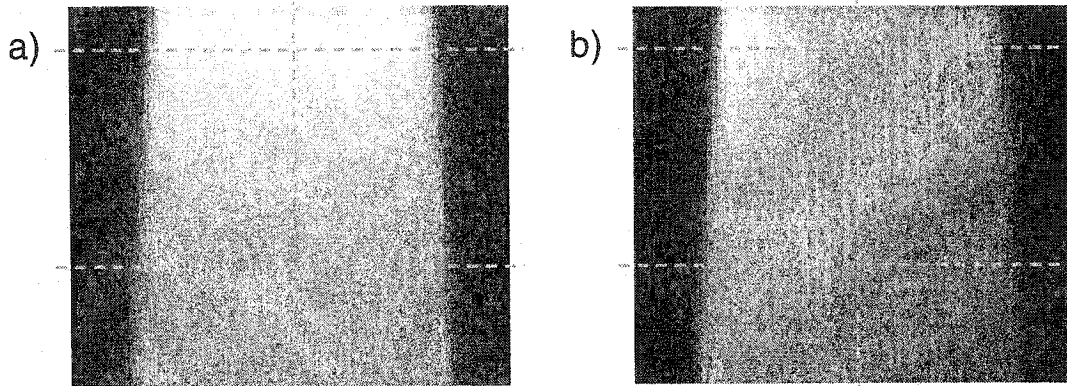


Figure 5.4: Central axis R_1 images of the 10x10 cm² open and 60° wedged beams. This figure shows the locations of the PDD and of the profiles (1.5 cm and 9.5 cm depth) on a) the open beam and b) the wedged beam.

For PDDs of the open and 60° wedge beams, the depth of dose maximum (d_{\max}) was measured to be 1.51 ± 0.19 cm. Due to the unreliability of the ion chamber in the dose buildup region and to surface effects in the gel dosimeter, the measurements between the surface and the depth of dose measurements were not compared. Figure 5.5 and Figure 5.6 show a very good qualitative agreement between the gel-measured PDDs and those measured with the ion chamber. Statistics were computed pixel by pixel and are presented in Table 5.3. Between d_{\max} and a depth of 14 cm (end of open beam gel), the mean differences between the gel and the ion chamber measurements were about 1% for both the open beam and the wedged beam.

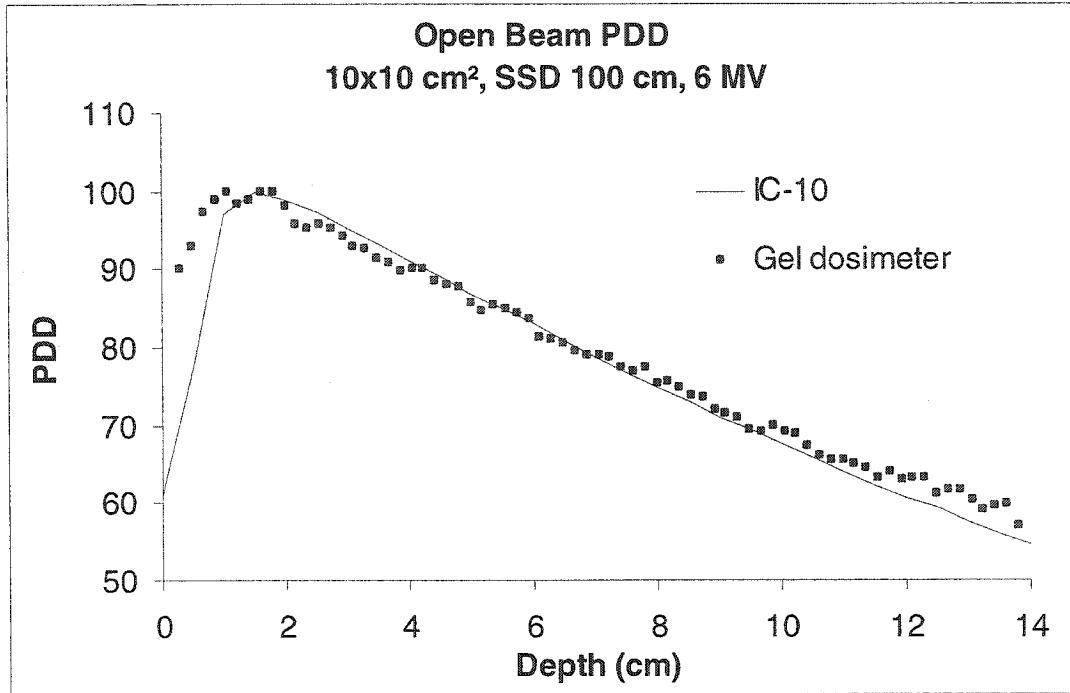


Figure 5.5: Percent Depth Dose (PDD) graph of a 10x10 cm² open beam.
The beam was directed through the bottom of the phantom and the top was left uncovered. This led to an increased oxygenation effect towards the end of the PDD.

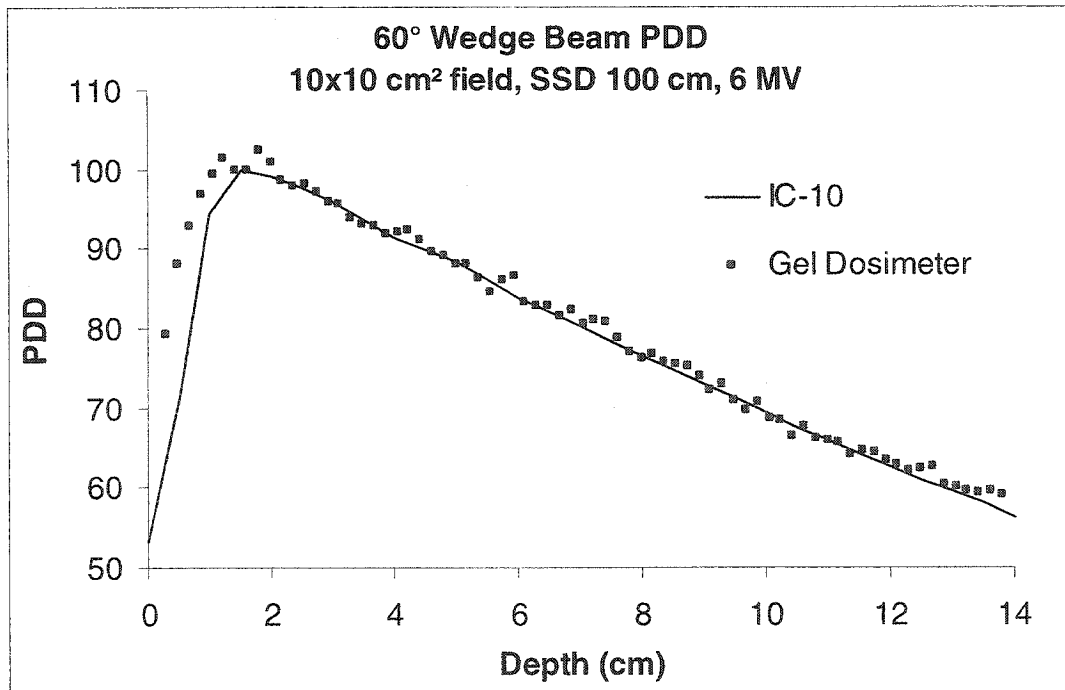


Figure 5.6: Percent Depth Dose (PDD) graph of a 60° wedge 10x10 cm² beam.
The beam was directed through the top of the fully filled and covered phantom.

Between d_{\max} and 10 cm, the average differences were less than 0.5%, and the absolute maximum differences for both curves were less than 3%. At depths beyond 10 cm, larger differences (up to 7.4%) can be seen in the open beam PDD (see Figure 5.5). The open beam was directed through the bottom of the phantom with the top surface exposed to air, leading to oxygenation effects at the end of the PDD.

Percent depth dose curves		Open beam	Wedged beam
d_{\max} to 10 cm depth	Mean difference	-0.1%	0.5%
	Maximum difference	2.9%	3.0%
	Number of points > 2%	7	4
d_{\max} to 14 cm depth	Mean difference	1.1%	0.7%
	Maximum difference	7.4%	3.5%
	Number of points > 2%	24	8
	Number of points > 5%	5	0

Table 5.3: Statistics of the open and wedged beam PDDs.

Considering OARs, Figure 5.7 and Figure 5.8 show a very good qualitative agreement between the gel-measured profiles and those measured with the ion chamber, at both depths of 1.5 and 9.5 cm. Statistics were computed pixel by pixel for the central 80% of the 10 cm field and are presented in Table 5.4. Profiles for both beams at both depths show an average difference between the off-axis ratios (OAR) of the gel and the ion chamber of less than 1%, with maximum absolute deviations that are less than 5%. In the penumbra, the positional error was less than 2 mm.

The mean deviations of the gel dosimeter measurements agree very well to the ion chamber measurements, and are less than the 2% or 2 mm ICRU-42⁴² requirements for a quality assurance dosimeter. The fluctuations in absolute maximum differences can be explained by the statistical noise in the MR-read images, while the discrepancy at 1.5 cm depth for the wedged beam hot spot (less than 4%) can be explained by the smaller dynamic range at high dose (Figure 5.3), leading to lower precision and higher uncertainty.

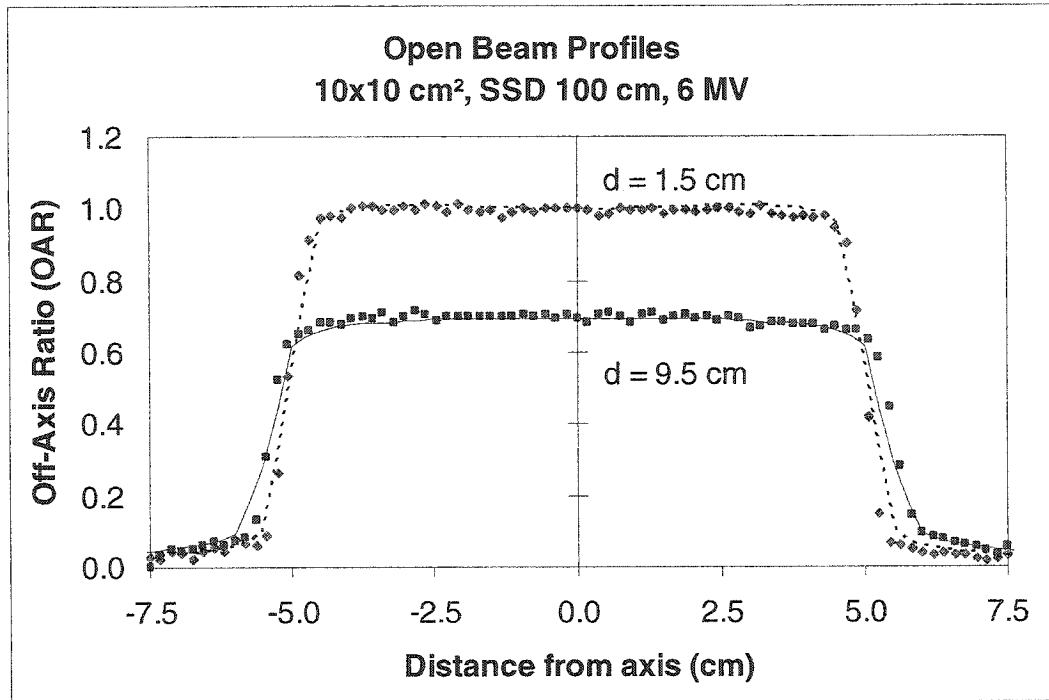


Figure 5.7: Profiles at 1.5 cm and 9.5 cm of the open beam. Gel-measured profiles are represented by the symbols, while the ion chamber profiles are a dotted line (1.5 cm) and a full line (9.5 cm).

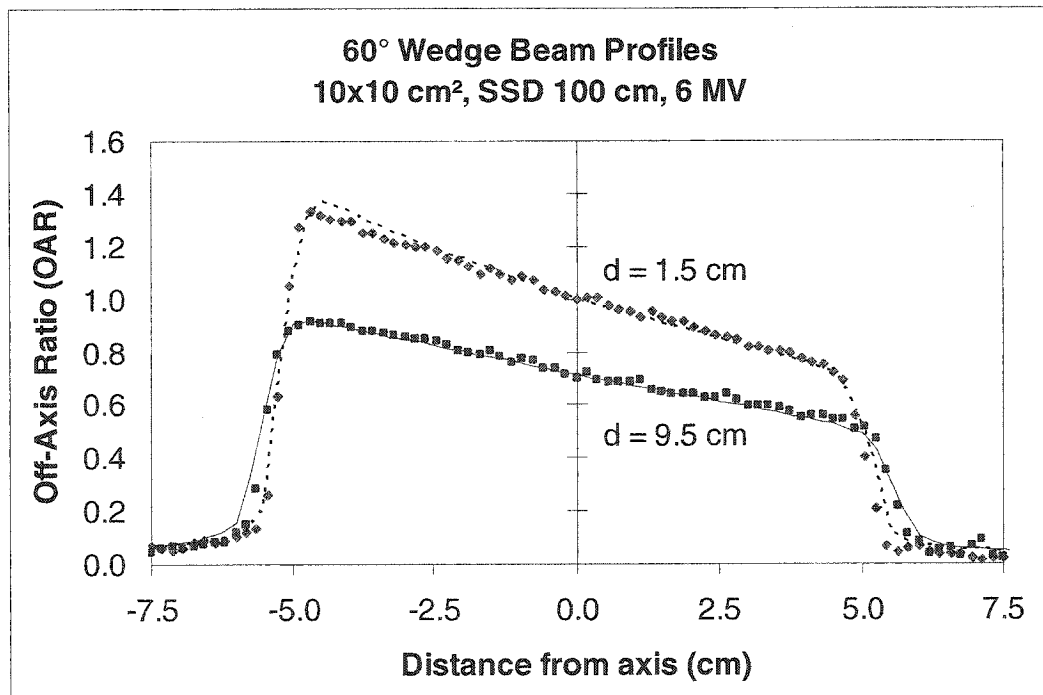


Figure 5.8: Profiles at 1.5 cm and 9.5 cm for the 60° wedge beam. Gel-measured profiles are represented by the symbols, while the ion chamber profiles are a dotted line (1.5 cm depth) and a full line (9.5 cm depth).

Open beam profiles	1.5 cm depth	9.5 cm depth
Mean difference	-0.7%	0.8%
Maximum difference	2.7%	4.2%
Number of points > 2%	4	10
Number of points > 3%	0	3
Wedged beam profiles	1.5 cm depth	9.5 cm depth
Mean difference	0.02%	1.0%
Maximum difference	4.2%	5.1%
Number of points > 2%	15	10
Number of points > 3%	4	3

Table 5.4: Statistics of the open and wedged beam profiles.

5.2 3D dose distributions and dose volume histograms

3D dose distributions were created by the combination of multiple beams, which can be either simple open beams, wedged beams or complex intensity-modulated beams. Regardless of the type of beams and of the shape of the phantom used, expected dose distributions can be calculated on commercially available treatment planning systems. 3D treatment planning consists of volume definition, beam geometry determination and dose calculation. By registering the Fricke-gel measured dose distribution with the image format of the treatment planning system, one can easily superimpose the measured dose distribution to the anatomical information from the CT scan. Similarly, the contours drawn on the anatomy and used to create the treatment plan can be applied to the gel-measured dose distribution and therefore measured dose-volume histograms can be computed.

5.2.1 Forward-planned box phantom

For this forward-planned experiment, four open beams irradiated a box phantom. Four isocentric beams intersected and created a cross-shaped irradiation pattern, with a region of uniform, higher dose where the beams overlapped (see Figure 5.9). This simple

configuration was used to verify the overall process which included the extraction of the dose information from the Fricke dosimeter system, the registration and fusion of the measured dose distribution to the treatment planning information image format, and finally the computation and comparison of the statistics and the dose-volume histograms for the measured and calculated dose distributions.

In Figure 5.9, we see the TPS-calculated dose matrix and the arbitrary contours GTV, CTV, PTV and PTV2, as well as the External and the External-margin contours. Figure 5.9 also shows that the calculated dose matrix does not cover the whole external contour of the box.

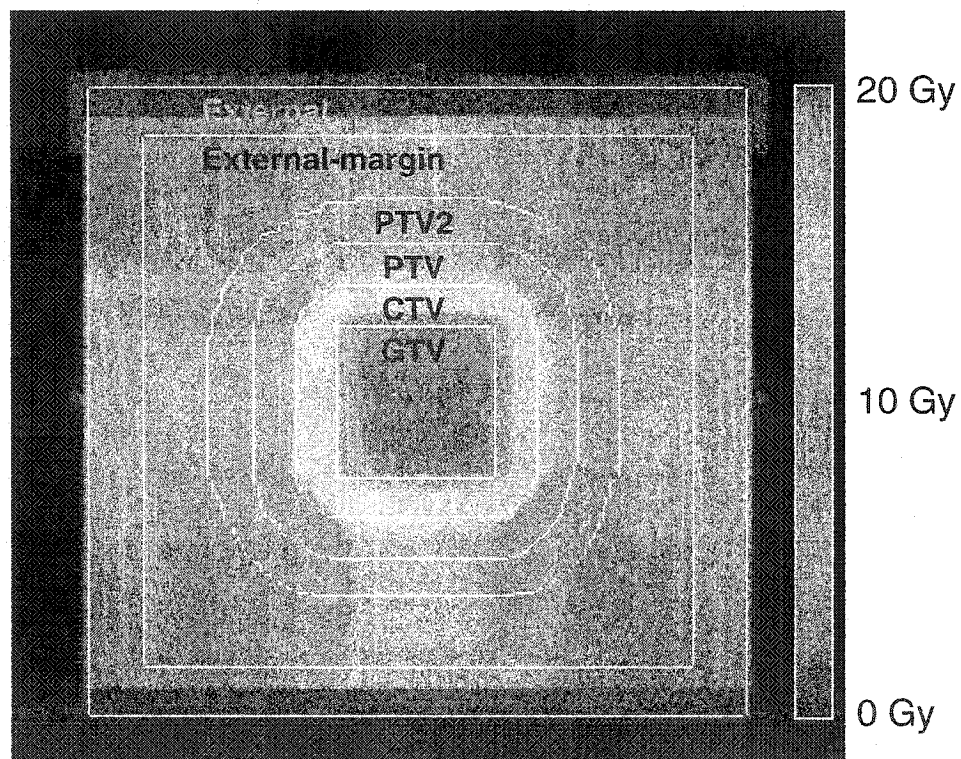


Figure 5.9: Forward-planned box phantom contours on TPS dose at isocenter.

Figure 5.10 shows the gel-measured dose distribution, which qualitatively compares well to the TPS-calculated dose distribution of Figure 5.9.

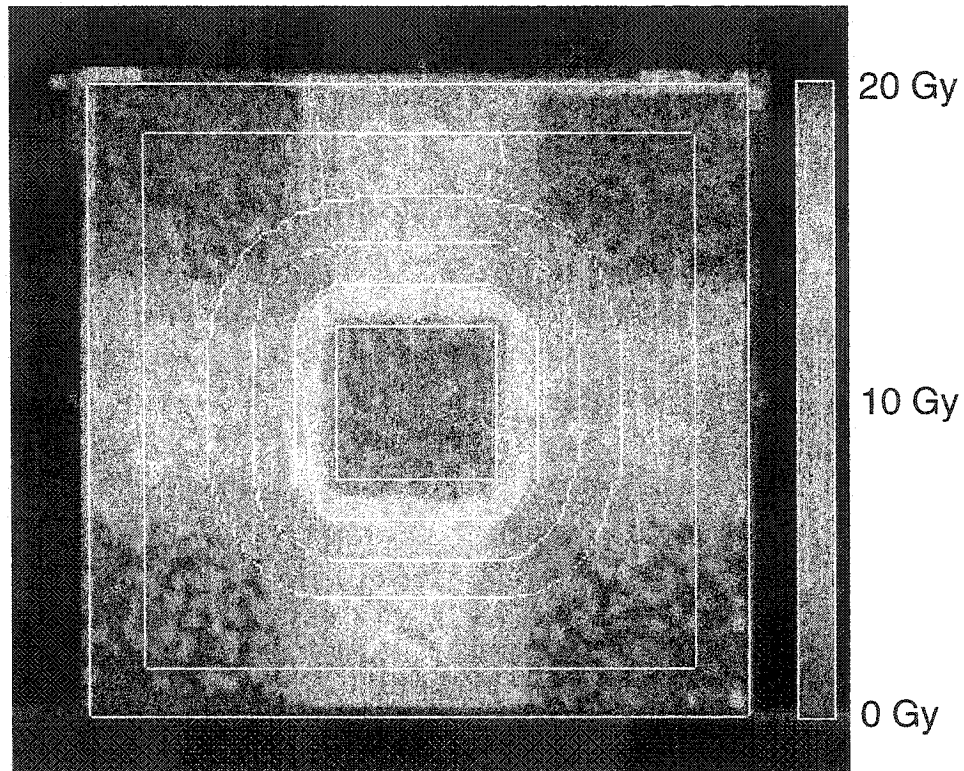


Figure 5.10: Forward-planned box phantom contours on gel dose at isocenter.

The 20, 50, 60, 90 and 98% isodose lines are shown at the level of the isocenter in Figure 5.11 and Figure 5.12. The first obvious difference is that the TPS-calculated isodose lines are smoother than those obtained from the gel-measured dose distribution. This is caused by statistical noise in the MR images. Further examination shows that the isodose lines in the high dose gradient regions are slightly different. For example, the 60% gel isodose is obviously within the CTV contour, while the 60% TPS isodose more or less conforms to the contour, and the 20% and 50% gel isodoses, are closer than the corresponding TPS isodoses.

In order to explain these isodose discrepancies, the TPS-calculated dose distribution was subtracted from the gel-measured dose distribution. Figure 5.13 shows the percent dose difference distribution at the isocenter, in the range -5% to 5%, relative to the isocenter dose (20 Gy), with all values above or below set to +/- 5%. In this figure, the difference in noise level is easily seen, and the dose difference at the beam edges becomes evident.

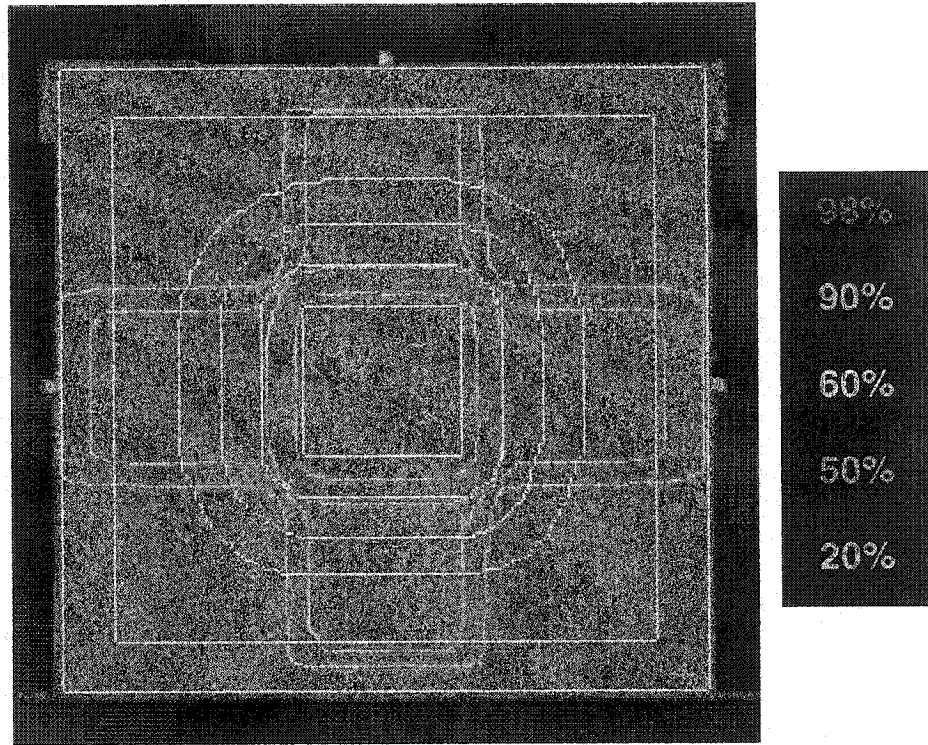


Figure 5.11: Forward-planned box phantom TPS isodoses on CT and contours.

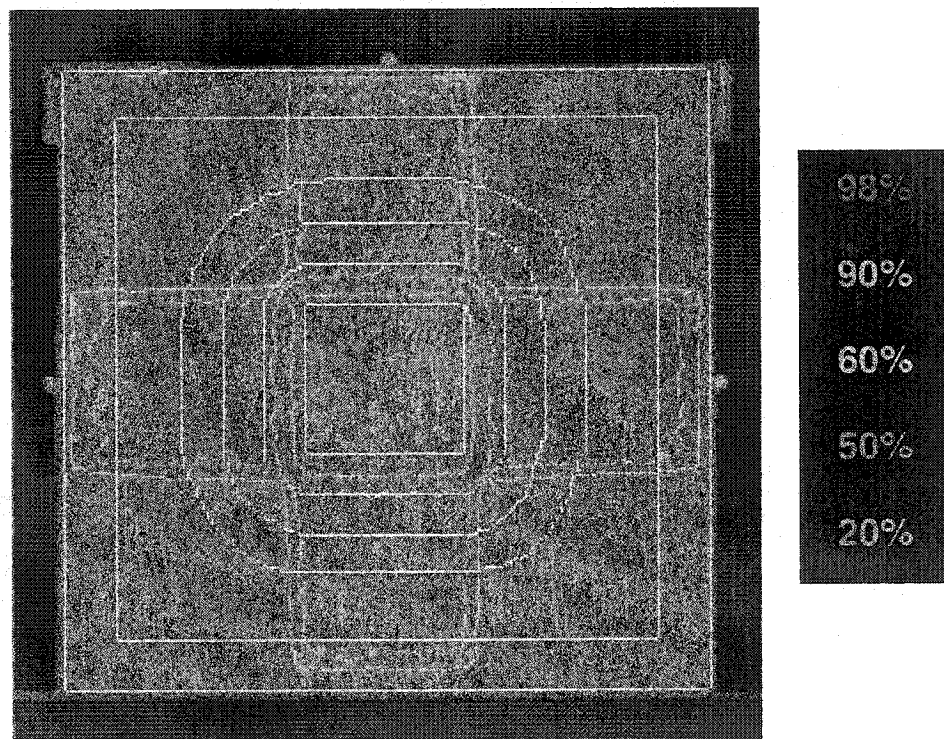


Figure 5.12: Forward-planned box phantom gel isodoses on CT and contours.

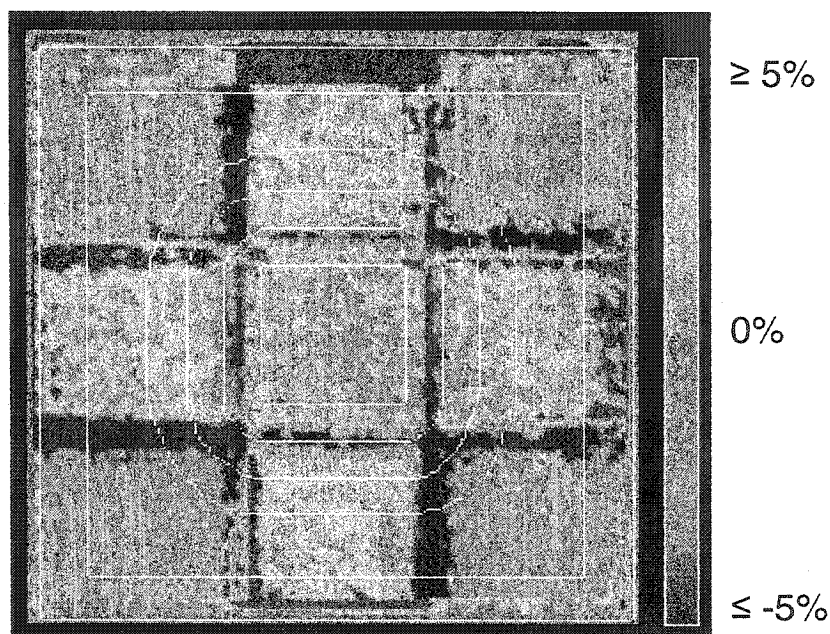


Figure 5.13: Percentage dose difference map at the isocenter of the box phantom. This figure shows the dose distribution difference (gel-measured - TPS-planned) at the isocenter of the box phantom, as a percentage of the isocenter dose (20 Gy).

The TPS predicts a wider penumbra than the gel measures, but within the gel penumbra, the dose gradient is sharper. This effect is the opposite of the expected gel diffusion, and can only be explained by how the TPS deals with lateral scatter at beam edges. The TPS uses beam profiles acquired in a very large watertank to calculate profiles in the smaller phantom, and thus overestimates the amount of lateral scatter at the beam edges¹³.

On a pixel-by-pixel basis, these differences can be as high as 8 Gy (steep dose gradients) but the absolute mean difference is 0.12 Gy. This pixel-by-pixel variation is due to statistical noise in the gel data, imprecision of the TPS-dose calculation in the penumbra, misalignment of the phantom for the irradiation and errors stemming from the image registration and fusion processes.

Figure 5.14 shows the difference between the gel and TPS dose maps in the coronal axis. The misalignment in the z-direction is most apparent at the beam edges, where it presents a rippled appearance, up to 5 pixels wide. However, by translating the datasets to minimize the difference, the misalignment was estimated to be between one and two pixels

(1 to 2 mm). The misalignment and ripples can be explained by alignment limitations of the 3 mm thick slices and the multiple image interpolations needed in order to fuse the gel and TPS datasets. The image fusion technique required cubic voxels, so both datasets had to be subdivided and linearly interpolated in the z-direction in order to make the 3 mm slice thickness the same as the pixel size (1.875 mm for MR images, 1.015 for CT images). During the image fusion, the gel data was also interpolated in x, y and again in z in order to have the same pixel size as the TPS data.

Overall, the dose discrepancies found at the beam edges in the coronal image (Figure 5.14) will have an impact on the minimum and maximum dose of the CTV, PTVs and External-margin structures.

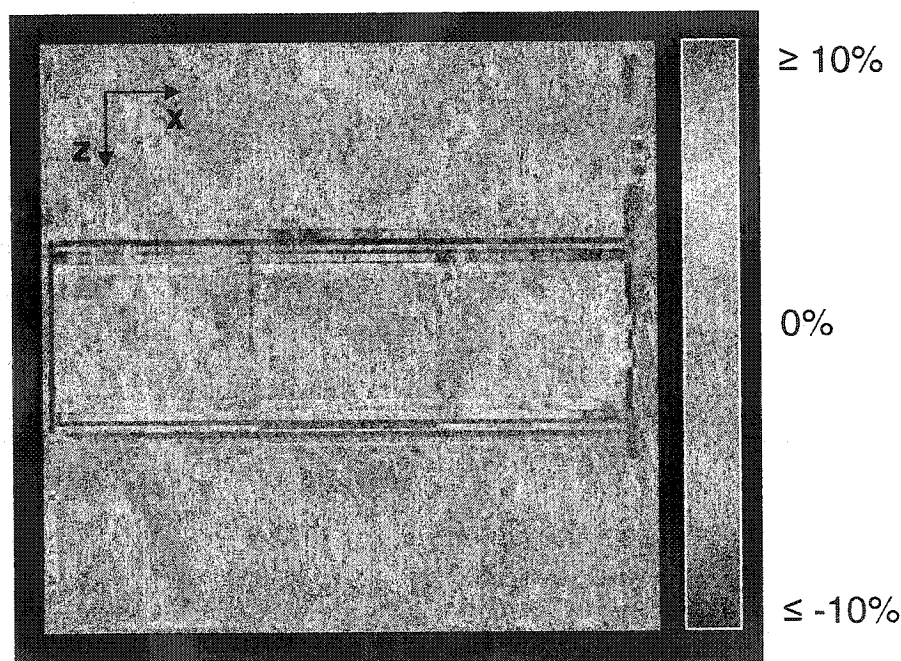


Figure 5.14: Mid-coronal slice showing misalignment of the box in the z-axis. The misalignment and interpolations create a noticeable ripple effect at the high dose gradient beam edges (shown as a percentage of the isocenter dose).

Table 5.5 shows excellent correspondence between the gel-measured and TPS-calculated mean doses for each of the contoured structures, with dose differences less than 0.3 Gy. However, the minimum and maximum doses for each contour present higher differences. Of course, results below the minimum detectable dose of 1.12 Gy were not considered for the comparison.

Forward-planned box phantom		MR-Measured (Gy)	TPS-Calculated (Gy)	Difference	
				(Gy)	(%)
External - margin	Minimum Dose	0.00	0.00	n/a	n/a
	Maximum Dose	11.93	10.81	1.12	10.4%
	Mean Dose	1.27	1.39	-0.11	-8.2%
PTV II	Minimum Dose	0.00	0.05	n/a	n/a
	Maximum Dose	11.90	10.75	1.15	10.7%
	Mean Dose	3.57	3.66	-0.09	-2.6%
PTV	Minimum Dose	0.00	0.35	n/a	n/a
	Maximum Dose	13.02	12.94	0.08	0.6%
	Mean Dose	5.65	5.88	-0.23	-3.8%
CTV	Minimum Dose	1.12	4.51	-3.39	-75.2%
	Maximum Dose	20.17	19.72	0.45	2.3%
	Mean Dose	14.00	14.04	-0.04	-0.3%
GTV	Minimum Dose	17.48	17.52	-0.04	-0.2%
	Maximum Dose	20.70	20.01	0.69	3.4%
	Mean Dose	19.49	19.62	-0.13	-0.7%

Table 5.5: Forward-planned box phantom contour statistics.

For each contour, the minimum, maximum and mean doses measured with the gel dosimeter are compared to the ones calculated by the treatment planning system. The acronym n/a (not applicable) refers to cases when the measured MR dose is less than the minimum detectable dose.

The largest difference is -3.39 Gy for the minimum dose of the CTV, which contains the most important dose gradients, as seen in Figure 5.9 to Figure 5.12. However, only 4% of the CTV volume is found between the gel minimum of 1.12 Gy and the TPS minimum of 4.51 Gy. This area of the CTV, where the edges of the beams intersect, is sensitive to how the penumbra is calculated and how well the dose distributions are registered. The other discrepancies pertain to the maximum doses of the PTV2 and the External-margin contours. In these cases, the gel-measured maximum dose was higher by about 1.1 Gy, but the volume contributions were respectively only 9.8% and 2.8%. For the maximum doses of the GTV and CTV, the differences were 0.69 Gy and 0.45 Gy, with 7.1% and 0.3% of

the respective contributing volumes. In both cases, this can be attributed to the absolute dose normalization of the statistically noisy MR-measured relative dose distribution. The volume contributions were calculated using the differential DVH data (illustrated in Figure 5.16) and the calculated total volume for each structure, as found in Table 5.6.

Forward-planned box phantom	Number of pixels	Volume (cm ³)
External (Gel only)	1668117	1744.31
External-margin	1586343	1658.80
PTV II	329597	344.65
PTV	212058	221.74
CTV	116206	121.51
GTV	54834	57.34
Total volume	3967155	4148.37

Table 5.6: Number of pixels and volume of each contour in the box phantom.

Figure 5.15 shows how the measured cumulative DVHs compare to the calculated DVHs. There is a qualitative agreement between both, with the differences due to discrepancies between the dose distributions in the high dose-gradient regions, intrinsic positioning and registration uncertainties, and the unreliability of both the gel-measured and the TPS-calculated dose distributions at very low doses. Figure 5.16 presents the differential DVHs. There is an excellent correspondence between the gel-measured and TPS-calculated DVHs for all structures except for the CTV, which still show a general agreement in the dose-volume distribution. The discrepancies in the peaks can be explained by dose map interpolations in the 3 dimensions, binning the data in 1 Gy increments, and smoothing and rounding errors.

Overall, this experiment shows the potential of the dosimetric gel system to measure 3D dose distributions. There is a very good qualitative agreement between the gel-measured and TPS-calculated dose distributions. The overall mean dose difference for all pixels located inside the “External – margin” contour is 0.12 Gy. All contours show a

mean dose difference less than 0.25 Gy. The gel-measured and TPS calculated differential and cumulative DVHs also show very good agreement.

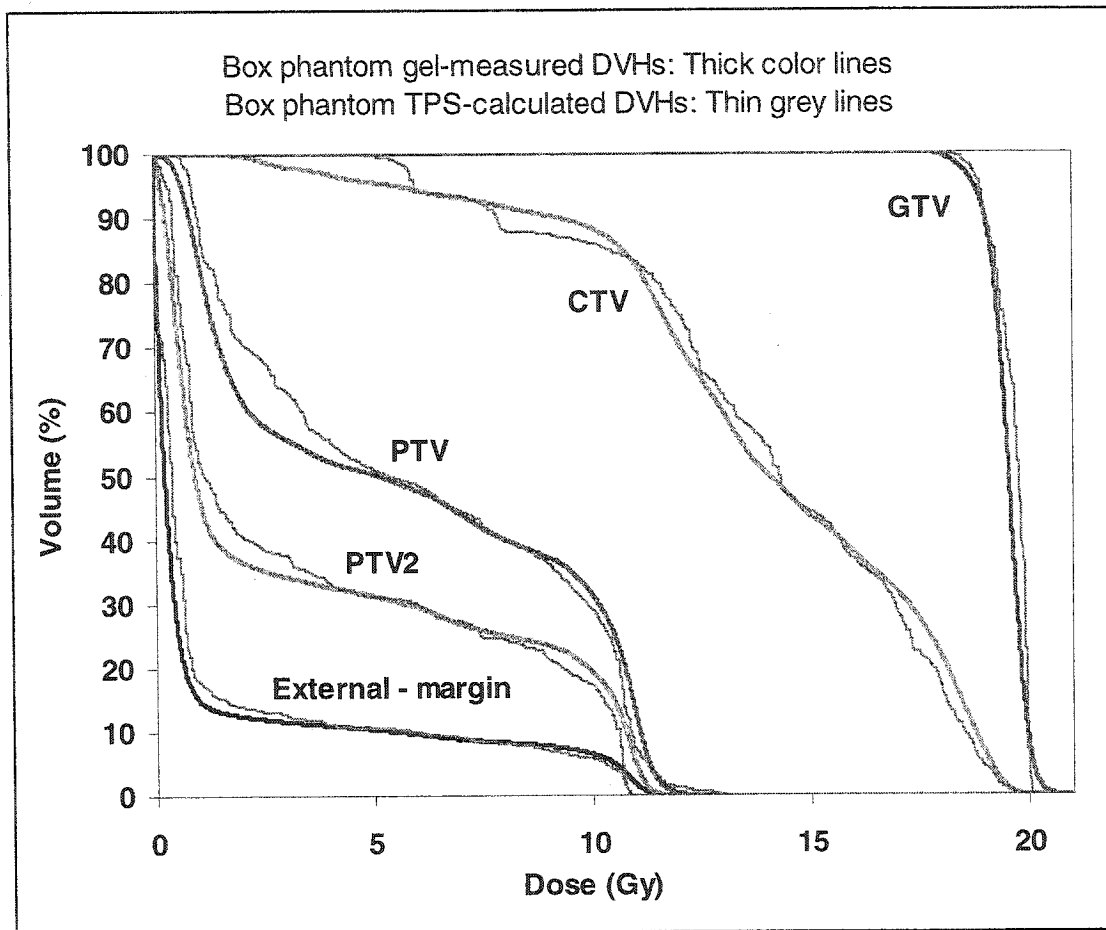


Figure 5.15: Forward-planned box phantom cumulative DVHs.

5.2.2 Forward-planned head phantom

For this experiment, a cylindrical GTV was defined in the middle of a head phantom and was irradiated to 20 Gy at the isocenter with three rectangular fields. One open beam entered between the eyes and two parallel-opposed wedged beams were directed through the lateral temples. This configuration was used to verify the overall performance of the Fricke dosimeter in an irregularly shaped phantom, with emphasis on the registration and fusion of the gel-measured dose distribution to the TPS image format. Statistics and dose-volume histograms were also computed and compared for the measured and calculated dose distributions.

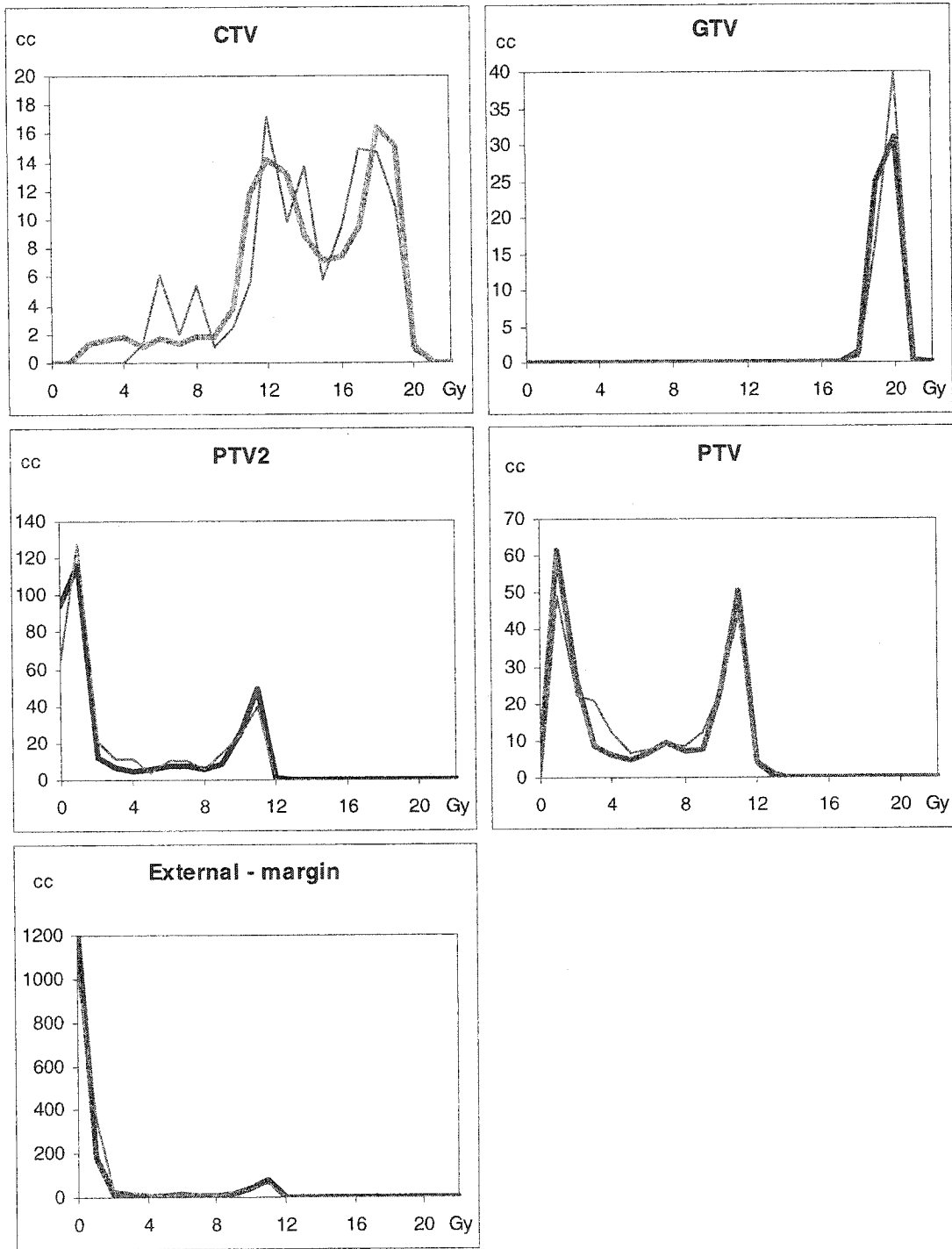


Figure 5.16: Forward-planned box phantom differential DVHs. The gel-measured DVHs are in thick color lines, while the TPS-calculated DVHs are represented by thin grey lines. The dose data was binned with one Gy increments.

Figure 5.17 presents four examples of the fused gel dose distribution superposed on the CT images and planning contours, at two locations below the isocenter (toward the neck) and two above the isocenter. By visual inspection, the fusion produced very good results for the whole volume. A more quantitative assessment is done by comparing DVHs.

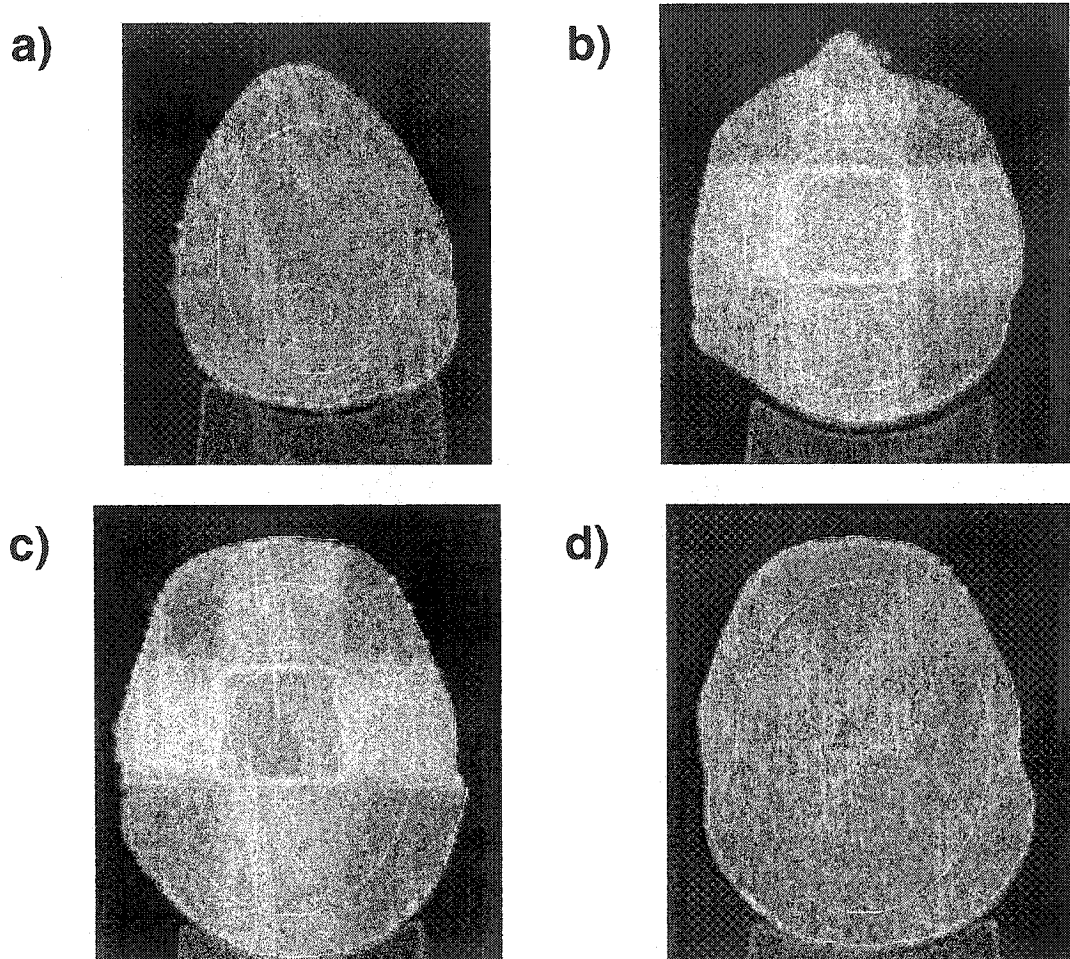


Figure 5.17: Image fusion verification for forward-planned head phantom.

These images show the image fusion of the gel-measured dose distribution with the CT and contours of the treatment planning system, at a) 6.7 cm and b) 2.6 cm below the isocenter, and c) 2.2 cm and d) 4.9 cm above the isocenter.

By comparing the dose distributions in Figure 5.18 and Figure 5.19, we can see a good qualitative agreement, even though the gel-measured dose distribution shows some mottle due to noise.

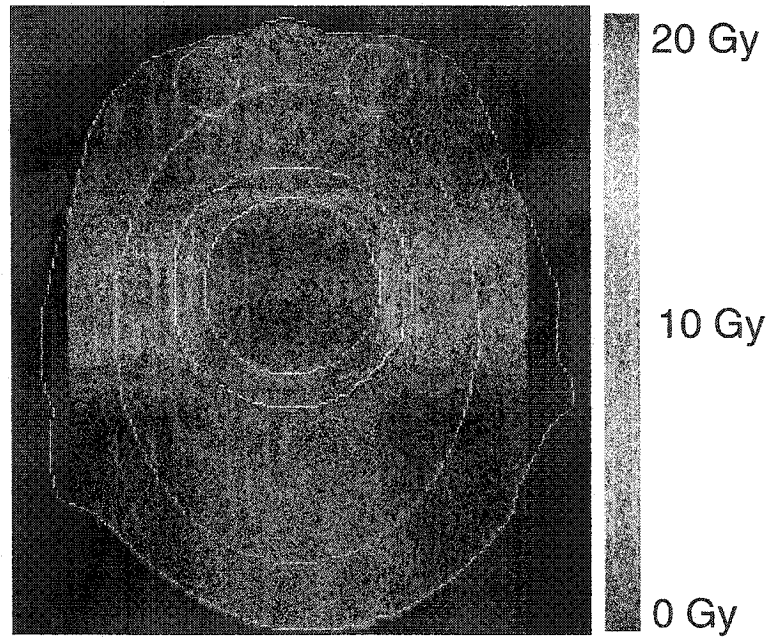


Figure 5.18: Forward-planned head phantom contours on TPS dose at isocenter.

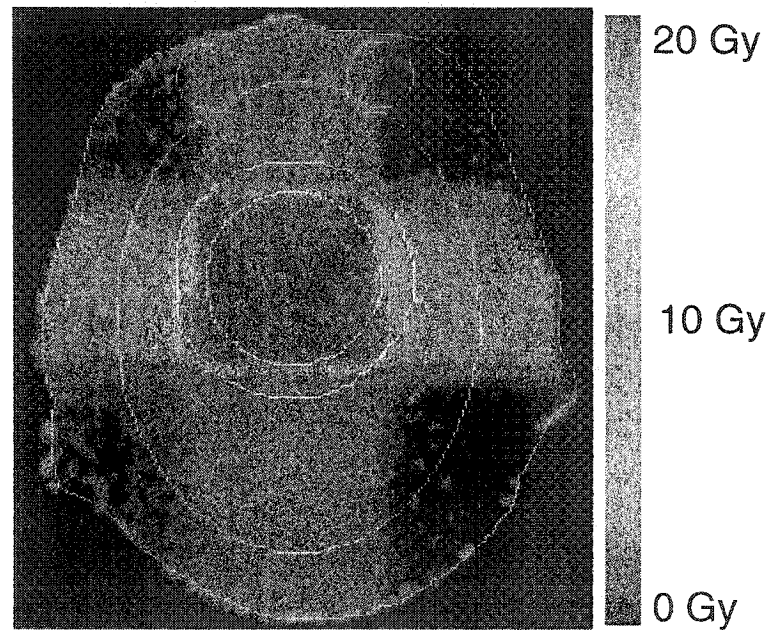


Figure 5.19: Forward-planned head phantom contours on gel dose at isocenter.

The isodose lines in Figure 5.20 and Figure 5.21 present a similar qualitative agreement, although the gel-measured 70% isodose line is mottled and asymmetrical compared to the TPS-calculated isodose line.

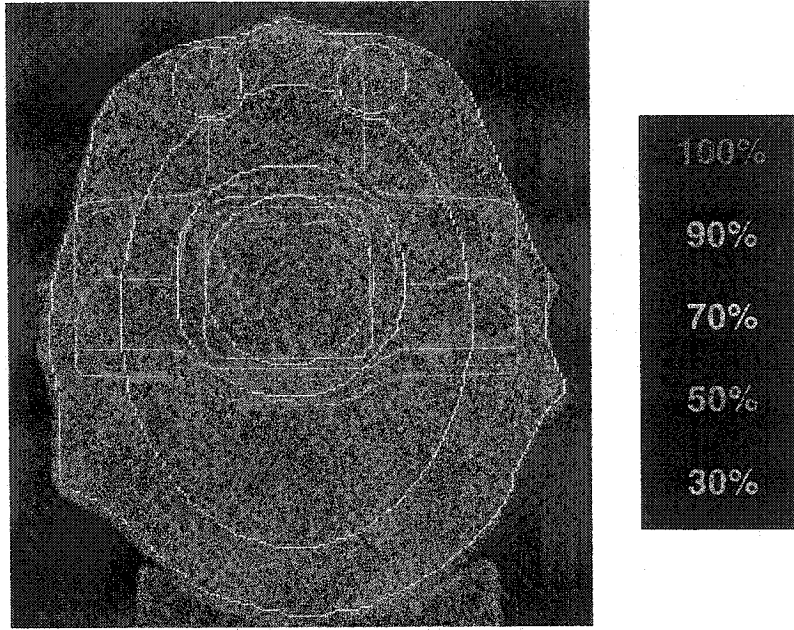


Figure 5.20: Forward-planned head phantom TPS isodoses on CT and contours.

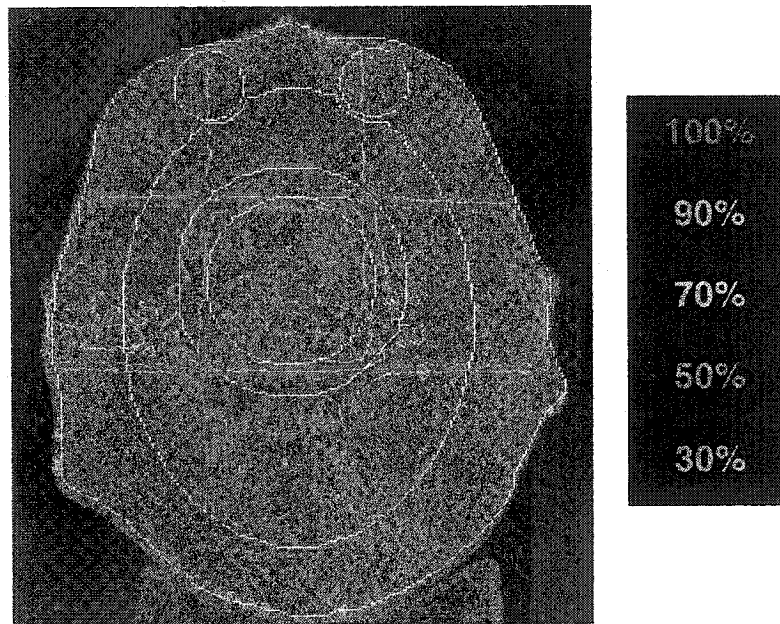


Figure 5.21: Forward-planned head phantom gel isodoses on CT and contours.

Figure 5.22 shows a similar asymmetry in the difference dose map, which was probably caused by misalignment of the head phantom at the time of the irradiation. Simply resting on a clinical headrest, the head phantom had six degrees of freedom (translations and rotations along the three axis) to account for. Yet, the mean dose

difference is less than 0.25 Gy for all structures except the left eye, where it is less than 1 Gy. On a pixel-by-pixel basis, the difference between gel-measured and TPS-calculated doses, for all structures except the external contour, is between -5.99 and 7.05 Gy, with an average of -0.15 Gy (20 Gy delivered to the isocenter).

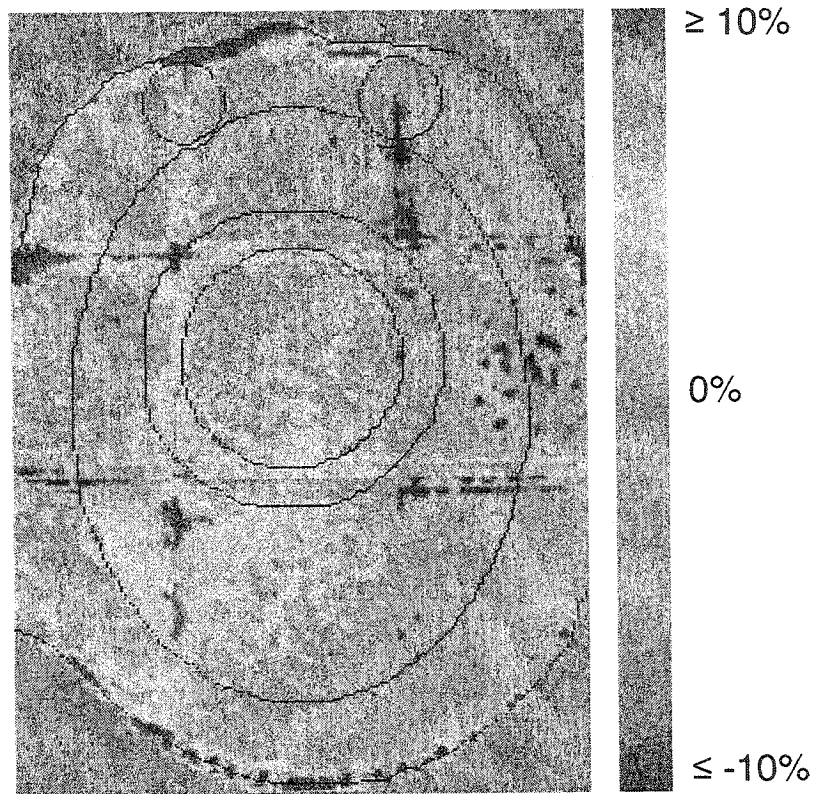


Figure 5.22: Percentage dose difference map at the isocenter of the head phantom.

This figure shows the difference between gel-measured and TPS-planned dose distributions at the isocenter of the forward-planned head phantom, as a percentage of the isocenter dose (20 Gy). The image was trimmed to the size of the TPS dose matrix.

Table 5.7 indicates that the largest difference is 3.21 Gy for the GTV minimum dose. However, only 0.12% of the GTV volume is found between the gel minimum and the TPS minimum. There is also a 1.43 Gy difference for the GTV maximum dose (3% of the volume), a 2.14 Gy difference in the External-margin minimum dose (0.04% of the volume), and a 1.14 Gy difference in the PTV maximum dose (0.6% of the volume). Excluding these values, all minimum, maximum and mean absolute dose differences are below 1 Gy, and have an average of 0.36 Gy.

Forward-planned head phantom		MR-Measured (Gy)	TPS-Calculated (Gy)	Difference	
				(Gy)	(%)
External -margin	Minimum Dose	0.00	0.00	n/a	n/a
	Maximum Dose	18.18	16.04	2.14	13.3%
	Mean Dose	2.12	2.35	-0.23	-9.7%
PTV	Minimum Dose	0.00	0.72	n/a	n/a
	Maximum Dose	21.05	19.91	1.14	5.7%
	Mean Dose	9.53	9.64	-0.11	-1.1%
GTV	Minimum Dose	4.69	7.90	-3.21	-40.6%
	Maximum Dose	21.83	20.40	1.43	7.0%
	Mean Dose	18.55	18.39	0.16	0.9%
Left eye	Minimum Dose	0.00	0.32	n/a	n/a
	Maximum Dose	9.56	9.51	0.05	0.5%
	Mean Dose	2.96	3.89	-0.93	-23.9%
Right eye	Minimum Dose	0.00	0.32	n/a	n/a
	Maximum Dose	9.91	9.59	0.32	3.3%
	Mean Dose	5.28	5.06	0.22	4.4%
Cord	Minimum Dose	0.00	0.08	n/a	n/a
	Maximum Dose	3.61	2.74	0.87	31.8%
	Mean Dose	0.17	0.41	n/a	n/a

Table 5.7: Forward-planned head phantom statistics.

The acronym n/a (not applicable) refers to cases when the measured MR dose is less than the minimum detectable dose.

Figure 5.23 shows a qualitative agreement between the measured and calculated cumulative DVHs, even if the TPS DVHs present a staircase appearance compared to the MR DVHs. These are smoother because the MR data is intrapolated in 3 dimensions during fusion to reach the 0.898 mm side voxel size of the CT data, while the exported TPS DVHs are calculated on a 1.25 mm grid with the original 3 mm slice thickness, with little difference in dose from slice to slice. In small structures such as the eyes, the discrepancy between the gradual MR dose and the steplike TPS dose becomes obvious. The misalignment of the head phantom at the time of irradiation (Figure 5.21) also shows up as

an increased separation between the MR-measured eye DVHs. Furthermore, the eyes are located in the buildup region where both the measured and calculated dose distributions are unreliable. In larger structures, such as the PTV and GTV, the non-interpolated thick slices produce sharp variations at the superior and inferior edges of the structures, leading to steps in the DVHs. Once again, the interpolated MR-measured dose distribution is smoother.

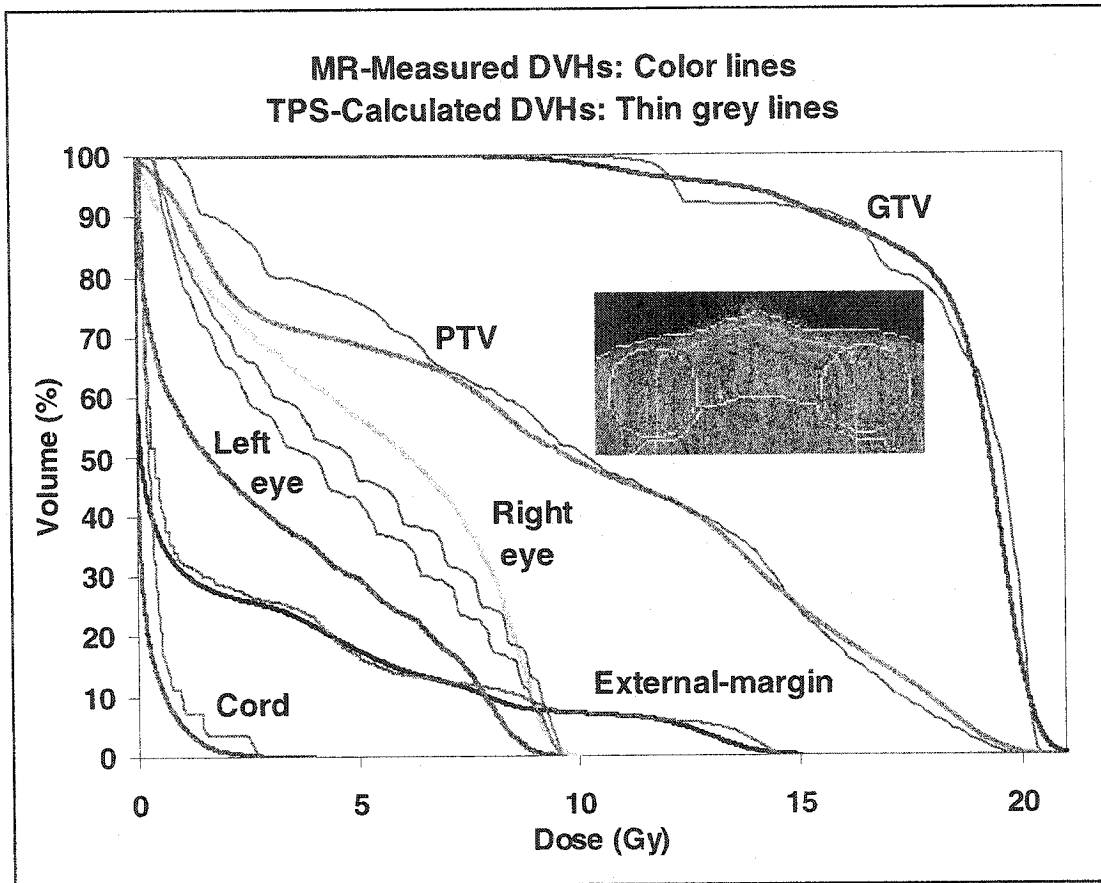


Figure 5.23: Forward-planned head phantom cumulative DVHs.

The insert shows the 1, 2, 4, 6, 8 and 9 Gy CadPlan isodose lines in the eyes. Combined with a limited dose dynamic range and a small volume, this leads to staircase DVHs.

Differential DVHs for the contours can be found in Figure 5.24. A very good agreement is seen between the gel-measured and TPS-calculated dose distributions, even for the cord and eyes. The discrepancies in the peaks can be explained by binning the data in one Gy increments, interpolation, and rounding errors. This experiment verified that the Fricke dosimeter performs very well in an irregularly shaped phantom. The image fusion

produced very good results and all values of minimum, maximum and mean doses above the MDD showed a difference of less than 1 Gy, with most below 0.3 Gy.

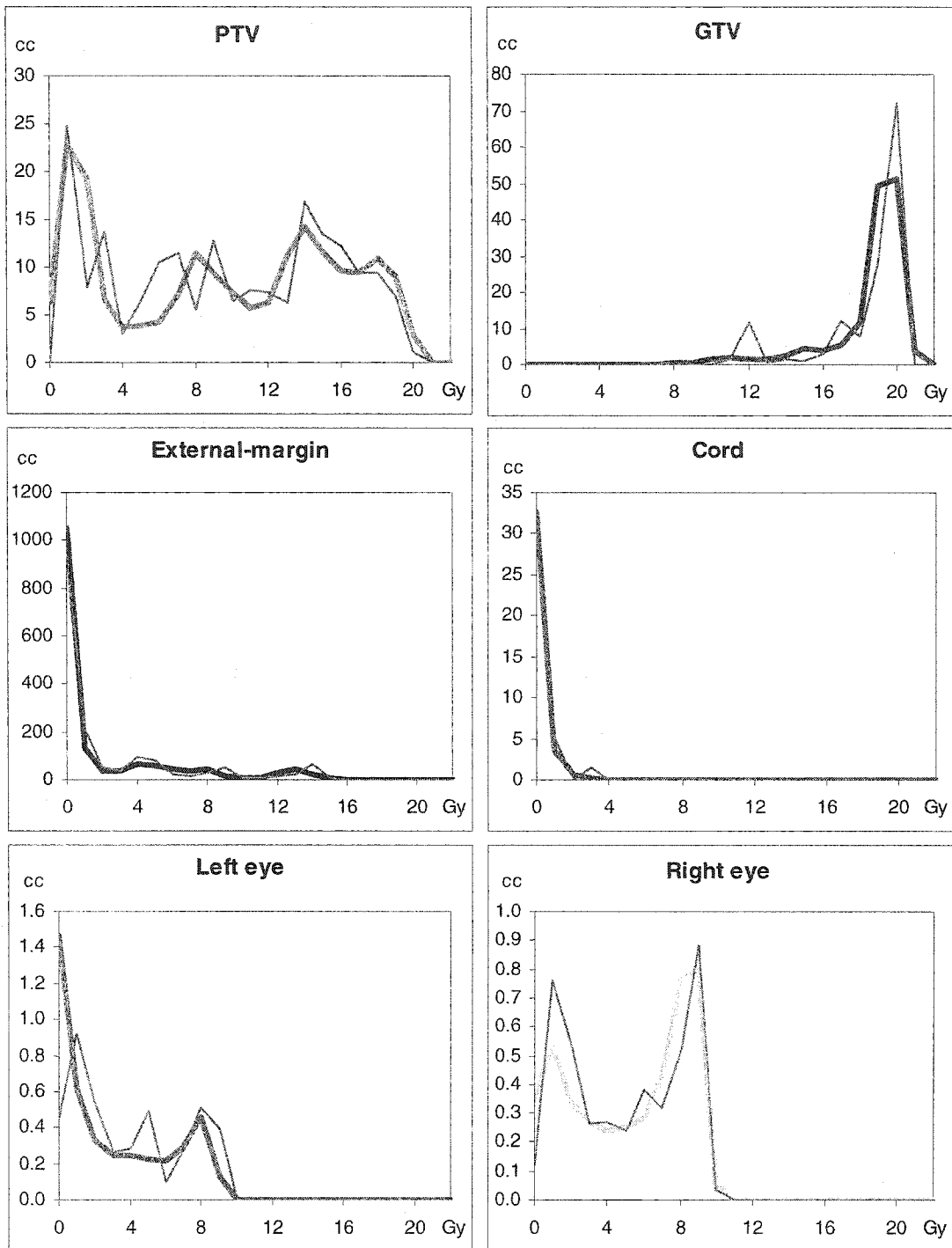


Figure 5.24: Forward-planned head phantom differential DVHs.

The gel-measured DVHs are in thick color lines, while the TPS-calculated DVHs are represented by thin grey lines. The dose data was binned with one Gy increments.

5.2.3 Helios IMRT inverse-planned head phantom

In this case, the treatment was designed to deliver a higher dose to the PTV than the GTV. This yielded an annular dose distribution with considerable dose gradients and a higher fluence at the edges of each IMRT beam. There were no dose constraints on the other structures, so the Helios IMRT inverse plan had spokes of high dose regions occurring outside the PTV. This plan tested the ability of the gel dosimeter to deal with irregularly shaped high dose gradients.

Figure 5.25 shows the TPS-calculated dose distribution on an axial plane at the level of the isocenter, while the gel-measured dose distribution can be found in Figure 5.26. To ease the visual comparison, the gel image was smoothed to remove most of the noise. The gel-measured dose distribution shows an excellent qualitative agreement with the corresponding TPS-calculated dose distribution.

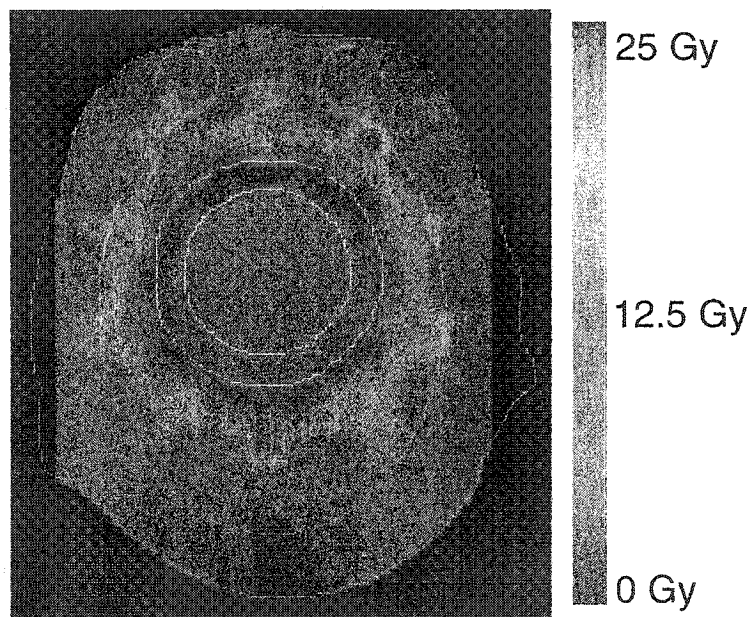


Figure 5.25: Helios IMRT contours superimposed over the TPS dose at isocenter.

When the TPS data was subtracted from the unsmoothed gel-measured dose distribution (Figure 5.27), the differences in the buildup region, near the edge and at the intersection of some of the beams became apparent.

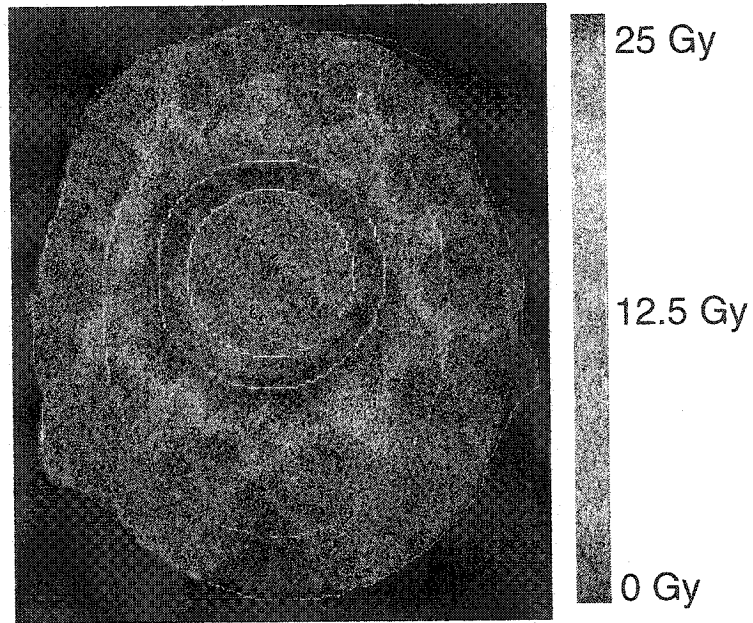


Figure 5.26: Helios IMRT contours superimposed over the gel dose at isocenter.

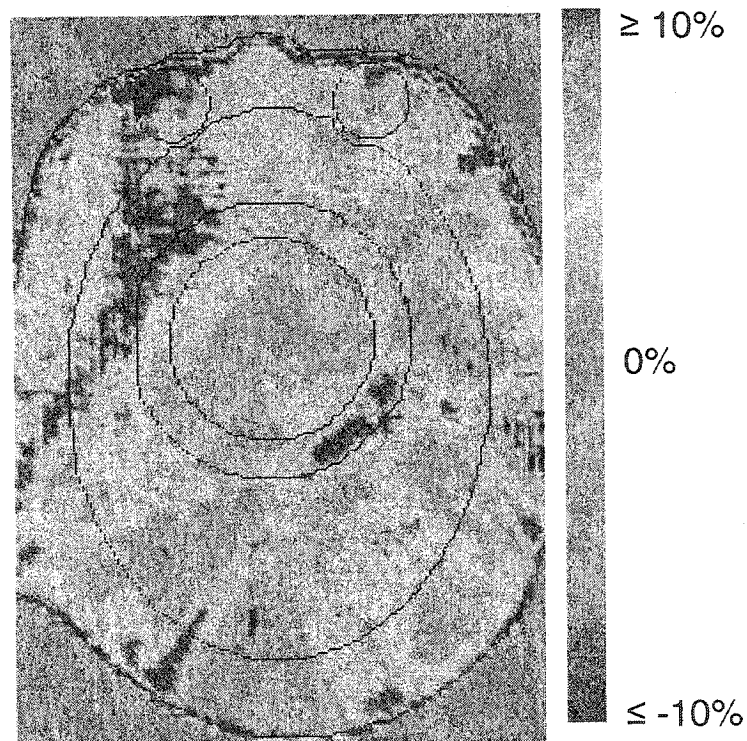


Figure 5.27: Helios IMRT percentage dose difference map at the isocenter.

This figure shows the dose distribution difference (gel-measured – TPS-planned) at the isocenter of the forward-planned head phantom, as a percentage of the isocenter dose (20 Gy). The image was trimmed to the size of the TPS dose matrix.

Figure 5.28 shows the TPS and gel dose distributions in the sagittal plane. The gel image is obviously noisier than the TPS image, but overall, the dose distributions compare in a satisfactory manner.

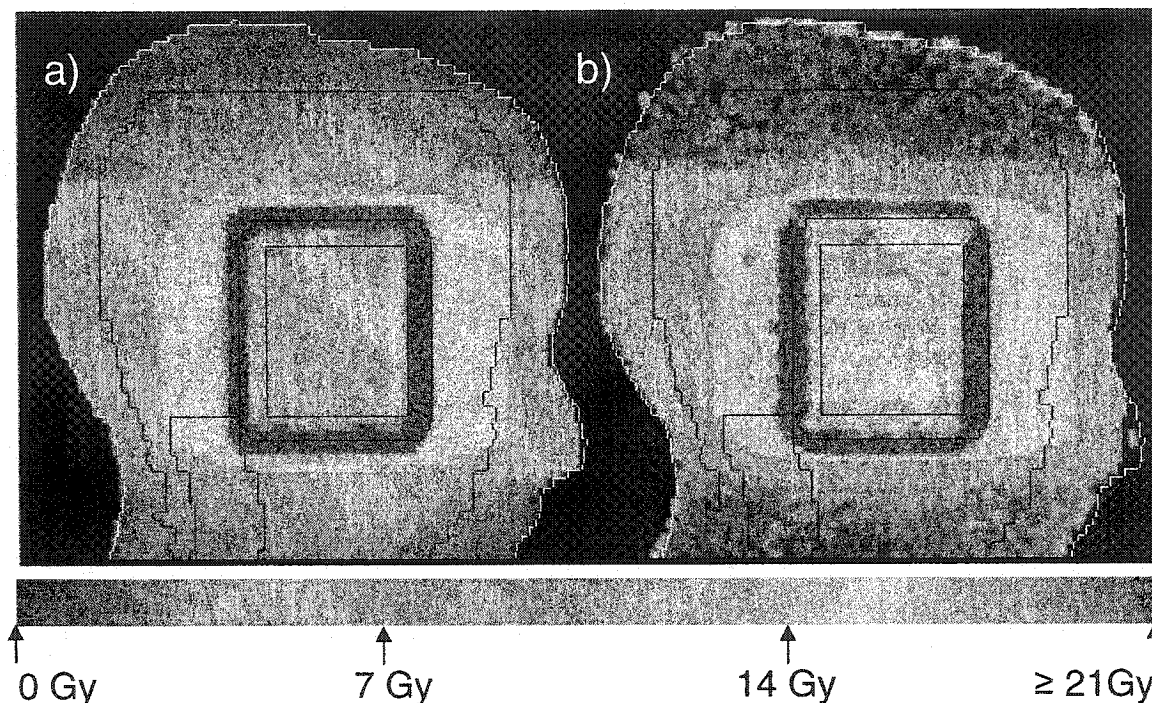


Figure 5.28: Sagittal views of (a) TPS and (b) gel dose distributions. All dose values above or equal to 21 Gy are put to the color value indicated.

The isodose lines found in Figure 5.29 and Figure 5.30 also show a good agreement between the two distributions. Quantitatively, the spikes, horns and steep dose gradients found in the dose distribution created a difficulty in comparing minimum and maximum doses, because uncertainties were amplified. This effect is apparent in the data presented in Table 5.8. The minimum and maximum doses for the PTV and GTV showed an absolute difference between 1.8 Gy (8.6%) and 3.0 Gy (12.6%). However, the mean doses for these structures demonstrated excellent agreement with a difference of 0.04 Gy (0.2%) and 0.31 Gy (1.6%) respectively.

The gel-measured cumulative DVHs for the PTV and GTV, found in Figure 5.31, were not as sharp as predicted by the TPS DVHs, but their differential DVHs (Figure 5.32) corresponded very well, with some spreading of the gel-measured DVHs. The discrepancies were due to diffusion, a slight phantom misalignment and the 1 Gy data bins.

The staircase effect (Figure 5.23 of the previous experiment) is not visible here because the eyes are now fully irradiated and the CTV and GTV have a more uniform dose distribution.

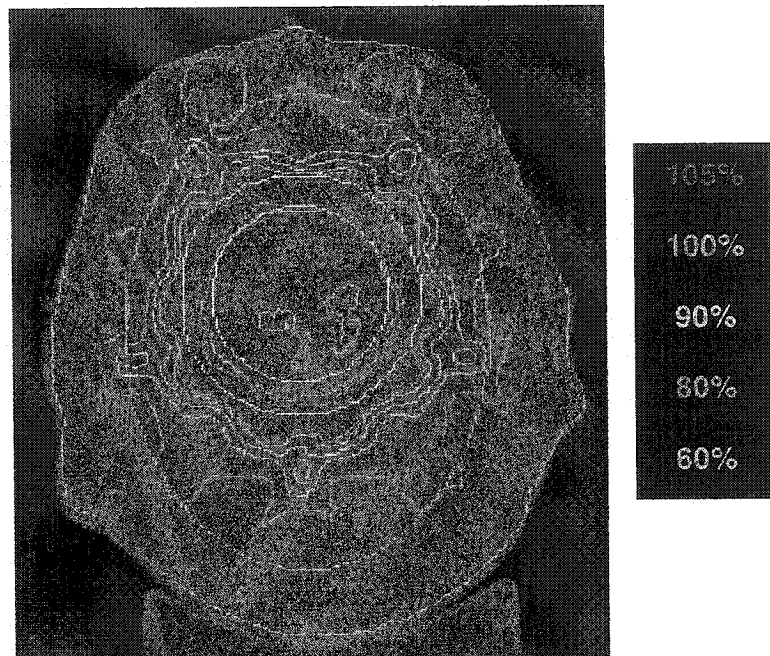


Figure 5.29: Helios IMRT TPS isodoses superimposed on CT and contours.

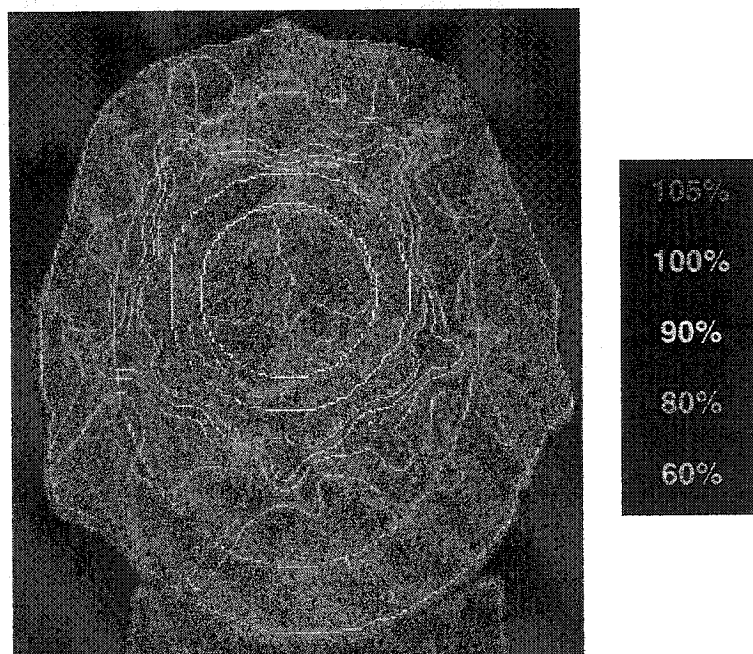


Figure 5.30: Helios IMRT gel isodoses superimposed on CT and contours.

Helios IMRT		MR-Measured (Gy)	TPS-Calculated (Gy)	Difference	
				(Gy)	(%)
External -margin	Minimum Dose	0.00	0.41	n/a	n/a
	Maximum Dose	25.71	24.79	0.92	3.7%
	Mean Dose	8.84	9.10	-0.26	-2.9%
PTV	Minimum Dose	16.99	18.95	-1.96	-10.3%
	Maximum Dose	26.75	23.75	3.00	12.6%
	Mean Dose	21.27	21.31	-0.04	-0.2%
GTV	Minimum Dose	16.99	18.95	-1.96	-10.3%
	Maximum Dose	22.40	20.62	1.78	8.6%
	Mean Dose	19.56	19.87	-0.31	-1.6%
Left eye	Minimum Dose	0.00	6.25	-6.25	-100.0%
	Maximum Dose	15.60	13.12	2.48	18.9%
	Mean Dose	10.88	9.91	0.97	9.8%
Right eye	Minimum Dose	4.10	6.45	-2.35	-36.4%
	Maximum Dose	16.58	13.75	2.83	20.6%
	Mean Dose	11.45	10.01	1.45	14.5%
Cord	Minimum Dose	0.00	0.41	n/a	n/a
	Maximum Dose	23.63	22.50	1.13	5.0%
	Mean Dose	4.22	5.06	-0.83	-16.5%

Table 5.8: Helios IMRT inverse-planned head phantom statistics.

The acronym n/a (not applicable) refers to cases when the measured MR dose is less than the minimum detectable dose.

There is also the possibility that the delivery is not exactly as predicted by the TPS. The DVHs of the cord and External-margin contours showed differences at doses lower than 2 Gy, because of the gel minimum detectable dose. Beyond 2 Gy, the differential DVHs had an excellent correspondence. The cumulative DVHs are off for a wider dose range since the initial dose discrepancy is carried on through the curve. 66% of the cord volume received 2 Gy or less, with 34% receiving less than 0.4 Gy. For the TPS, 61% of the cord volume received a dose less than 2 Gy, with a minimum dose of 0.41 Gy.

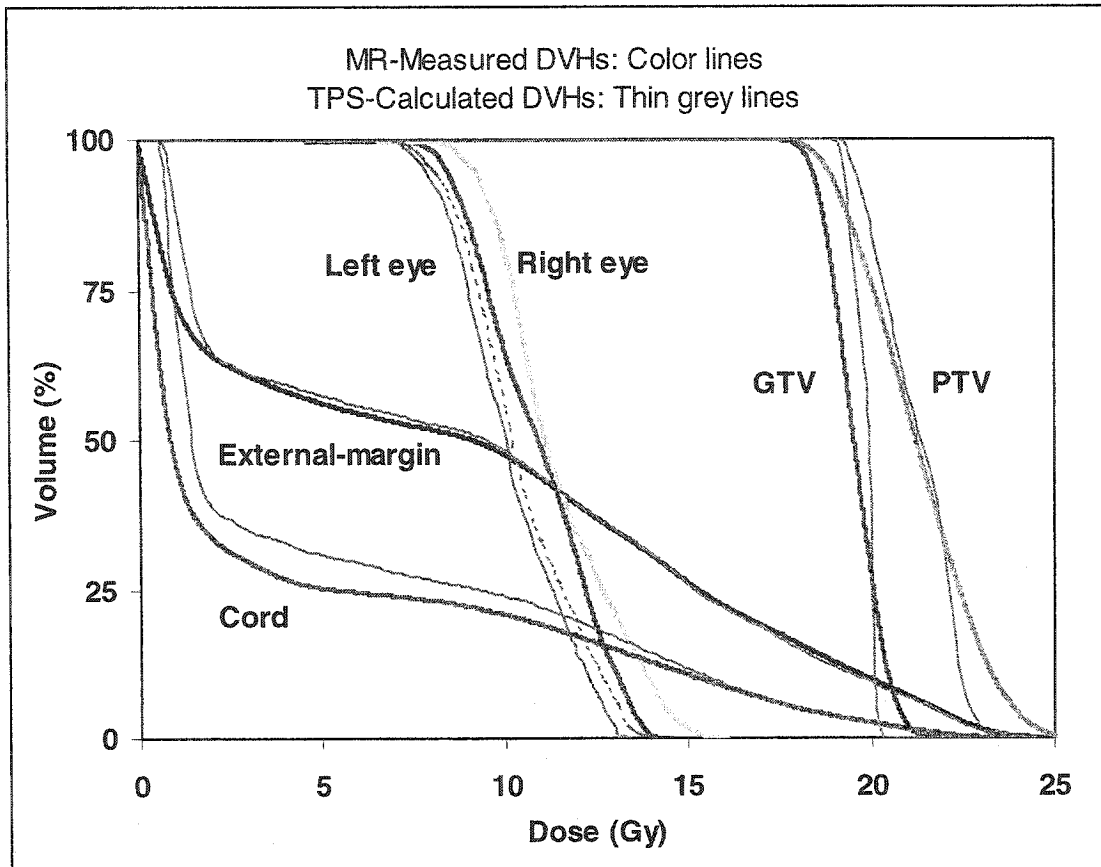


Figure 5.31: Helios IMRT inverse-planned head phantom cumulative DVHs.

The most noticeable differences, both for the statistics and the DVHs, are for the eyes, with differences in statistics ranging from 1 to 6 Gy. These structures have a volume so small that variations are more apparent than for larger structures, and they are located in the buildup region, where the TPS dose distribution is not trustworthy. Another reason for the discrepancy is the presence of high dose gradient “horns” within the eyes. However, the difference between the means is less than 1.5 Gy, and the differential DVHs for both modalities are very similar for the right eye and quite similar for the left eye. The discrepancies in the peaks can be explained by dose map interpolations in the 3 dimensions, binning the data in 1 Gy increments, and smoothing and rounding errors.

The gel-measured and TPS-calculated dose distributions compare well qualitatively and the differential DVHs show an excellent agreement. The mean dose difference was less than 0.4 Gy for the PTV, GTV and external-margin contour, and less than 1.5 Gy for the smaller cord and eyes structures. Overall, the results of this experiment are very good.

This shows that the gel dosimeter is an adequate modality to measure and validate 3D IMRT dose distributions as complex as an annular distribution.

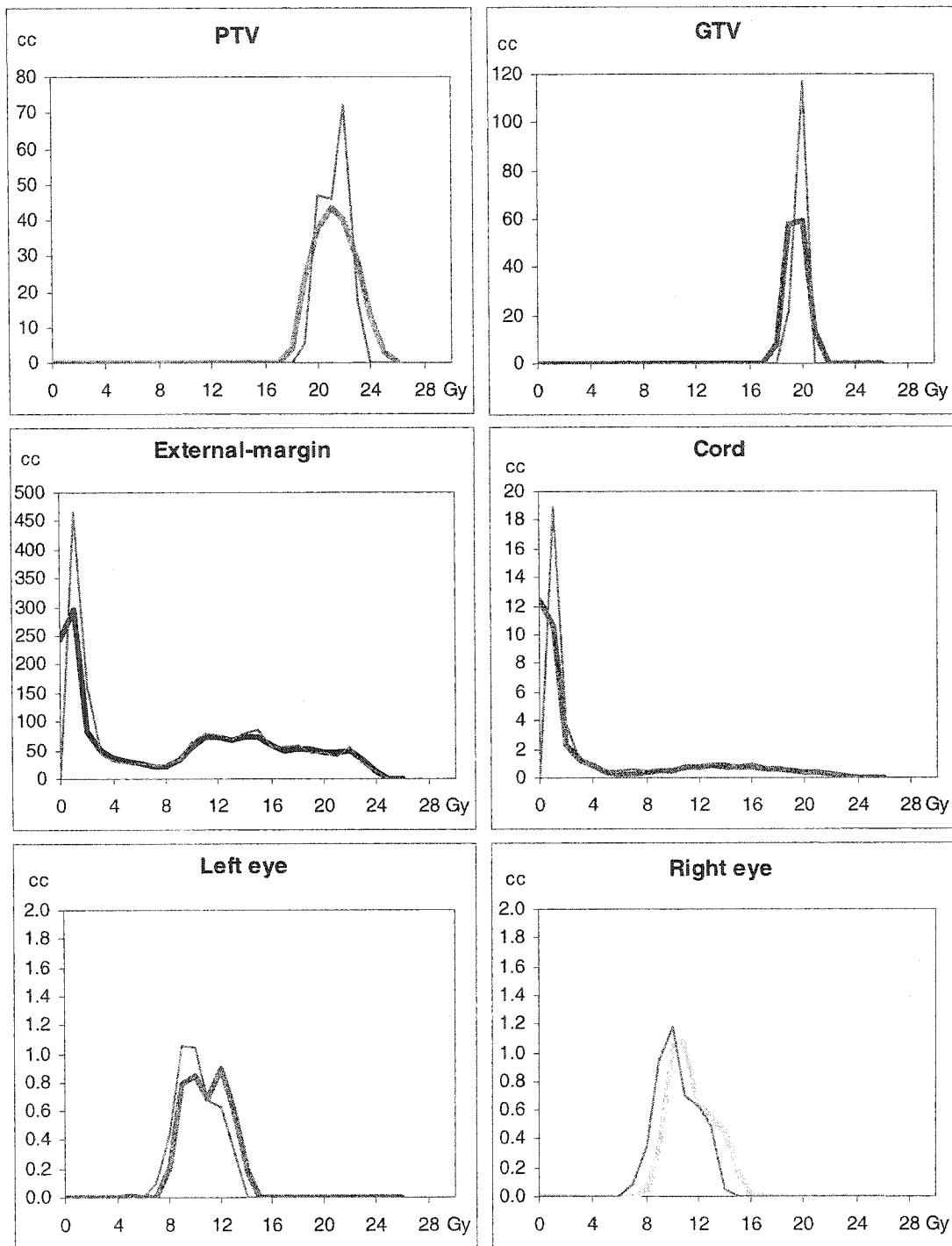


Figure 5.32: Helios IMRT inverse-planned head phantom differential DVHs. The gel-measured DVHs are in thick color lines, while the TPS-calculated DVHs are represented by thin grey lines. The data was binned with one Gy increments.

5.2.4 Corvus IMRT inverse-planned head phantom

Using the Rando anthropomorphic phantom, an experiment to simulate all the steps required to validate actual IMRT cases was performed. Before simulation, a hollow mold of the treated area (head) and a fiducials-bearing simulation mask were made. The mold also had fiducial markers at the same positions. The head of the anthropomorphic phantom was CT-simulated, with fiducial markers on the simulation mask (see section 4.1.2). Anatomically correct contours were drawn for the brain and eye, and an arbitrary GTV and PTV were created in the middle of the frontal area of the brain. The CT information and contours were transferred to the Corvus planning system where an IMRT treatment was inverse-planned. The plan consisted of five step-and-shoot intensity modulated beams. In this case, the treatment was designed to deliver a minimum dose of 18 Gy to the PTV and 24 Gy to the GTV. The IMRT inverse plan obtained with Corvus included steep dose gradients at the edges of the PTV and GTV. The plan was delivered to the gel-filled head mold in a single session, using a Varian Clinac 21EX treatment machine.

Figure 5.33 and Figure 5.34 show the isocenter in axial and sagittal images of the raw MR image and the corresponding extracted R_1 images.

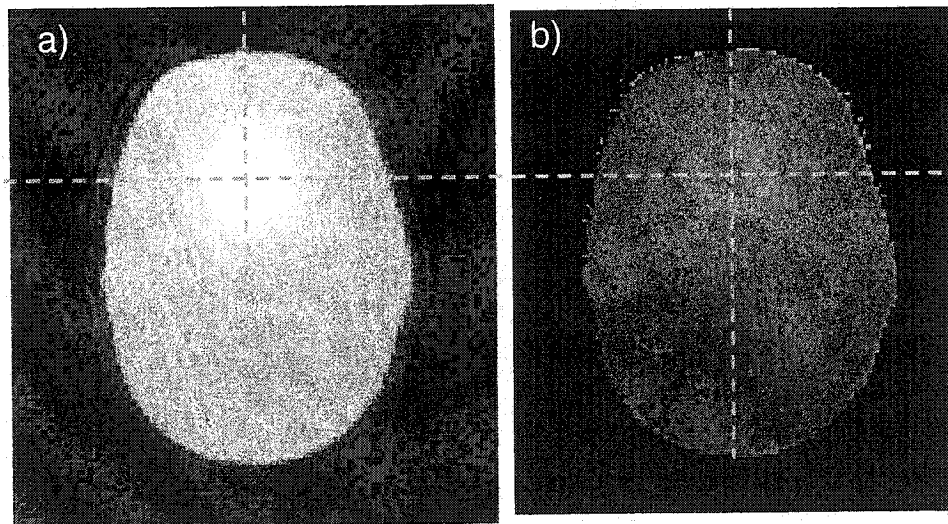


Figure 5.33: Axial image of Corvus IMRT inverse-planned head phantom.
a) Raw MR image ($T_R = 500$ ms) and b) R_1 dose image, dotted lines cross at isocenter.

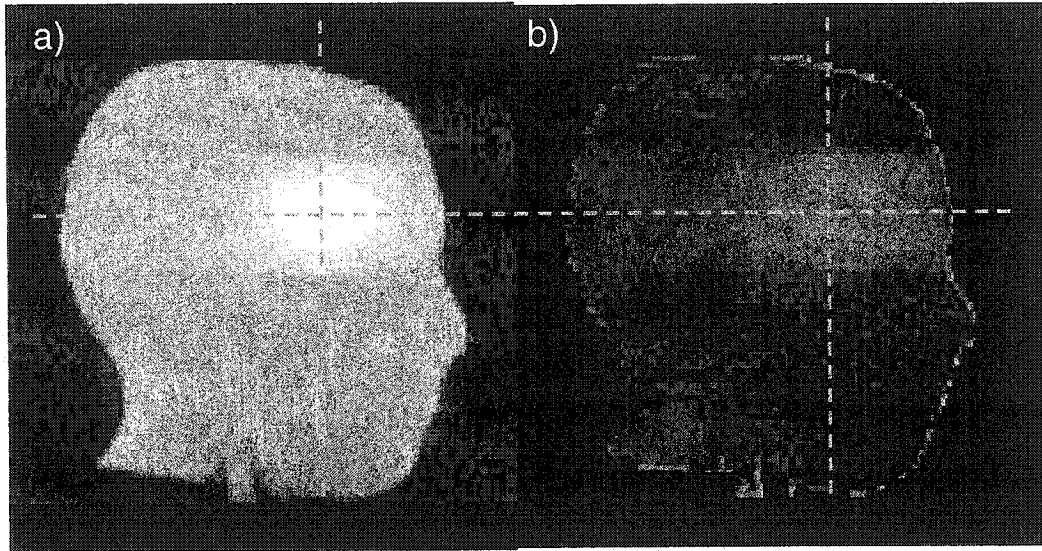


Figure 5.34: Sagittal image of Corvus IMRT inverse-planned head phantom.
 a) Raw MR image (TR = 500 ms) and b) R_1 dose image, dotted lines cross at isocenter.

A Gibbs ringing artifact appears as a series of lines parallel to the phantom edge in the axial raw MR image. The ringing, found inside and outside the phantom, is caused by incomplete digitization of the echo due to the fast spin echo sequence used⁶⁵. Combined with oxygenation effects through the phantom walls, this artefact can affect the measured dose in a surface layer up to 1.5 cm thick, therefore the data outside the brain (except for one eye) was excluded from this study.

It was apparent in the gel-measured dose distributions of Figure 5.35 a) and b) that the head mold was not a perfect reproduction of the original. There is not much difference at the anterior and posterior sides, as seen in a) and c), but the mold was obviously larger left and right than the phantom head. This could be explained by the fact that the hollow mold was made in two halves, joined together along the coronal axis. The head mask, a replica of the anterior half of the head, was similarly larger.

Although undesirable, the size difference between the planned volume and the actual treated volume mimicked a radiation therapy reality of weight gain or loss, and/or swelling of the treatment area between the time of simulation and the end of the 4 to 6 week long treatment course.

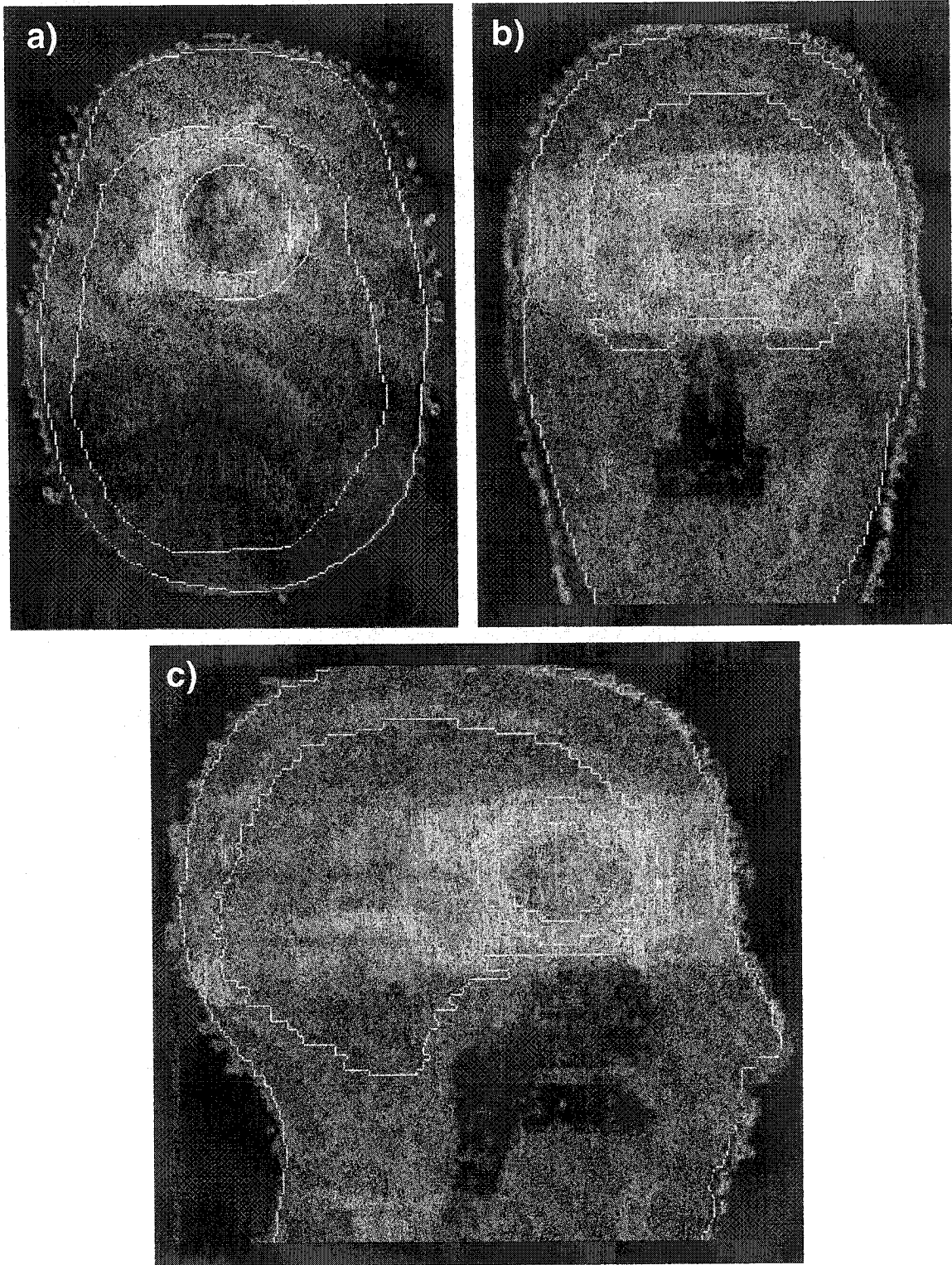


Figure 5.35: Corvus IMRT planning contours and gel dose on CT at the isocenter. These (a) axial, (b) coronal and (c) sagittal slices show how the gel-measured dose distribution follows the planning contours. It is obvious on the coronal image that the hollow mold is wider in the left-right direction than the original. The face mask, visible as a grey line outside the external contour, flares out in a similar fashion.

For this experiment, the 3D gel-measured and Corvus-calculated dose distributions were compared only through statistics and DVHs, since Corvus does not export whole volume dose distributions. At best, a screenshot of the isodose lines at the isocenter could be acquired and juxtaposed to the corresponding image of the gel-measured isodose lines, such as in Figure 5.36. This qualitative visual comparison has to suffice.

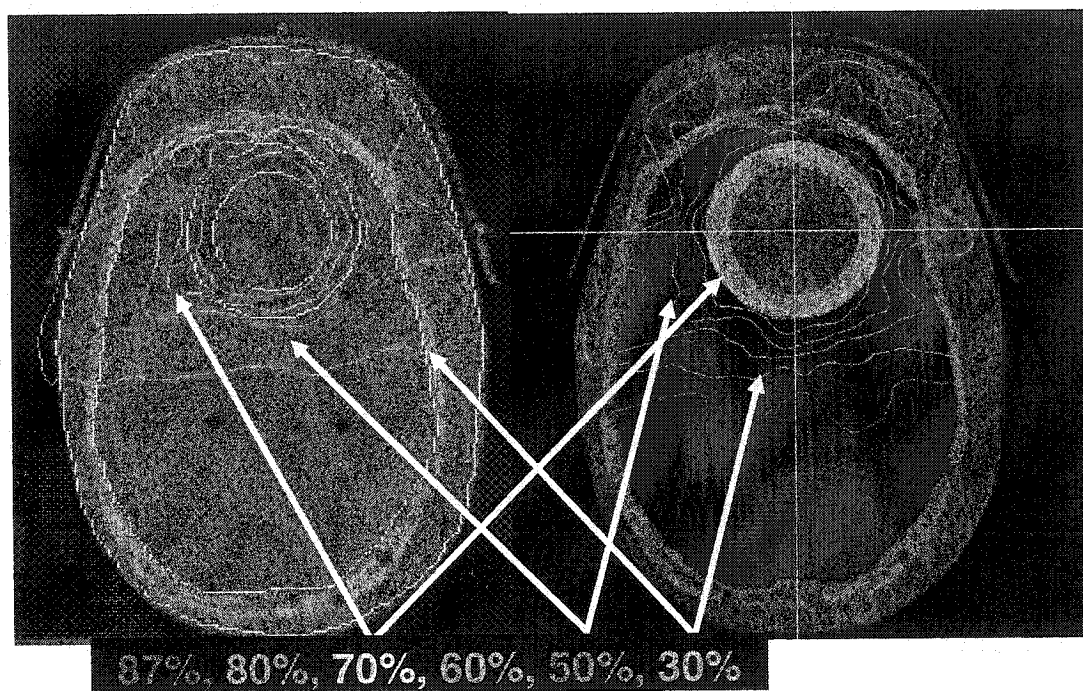


Figure 5.36: (a) MR isodoses and (b) Corvus isodoses on CT image with contours.

Table 5.9 presents the statistics for the Corvus IMRT experiment. Excluding the eye structure statistics, the average absolute difference for the minimum, maximum and mean statistics was 0.5 Gy. The relative differences were less than 5% at high dose (more than 15 Gy) and 3.2% at the 5 Gy level. For the GTV, the absolute dose differences for the minimum, maximum and mean were less than 0.2 Gy or 0.5%. The gel-measured PTV mean was higher by 1 Gy than the calculated dose. This discrepancy is also visible in the cumulative and differential DVHs (Figure 5.37 and Figure 5.38). The phantom appears to be 3 to 5 mm too low in the anterior/posterior direction, as can be seen in the axial and sagittal views of Figure 5.35. This explains the discrepancy and could either be an alignment error or a problem with the fiducial marker positions. Even with a misalignment

of the phantom on the treatment table, the use of margins (PTV) also irradiated to a high dose, allows for an excellent coverage of the GTV. The discrepancies in the differential DVH peaks can be explained by dose map interpolations in the 3 dimensions, binning the data in 1 Gy increments, and smoothing and rounding errors.

The discrepancy between the measured and calculated statistics (51%) and in the DVHs for the left eye could be explained by the fact that this structure had a very small volume and was located near the surface of the mold, where both the gel and TPS were somewhat unreliable.

Corvus IMRT		MR-Measured (Gy)	TPS- Calculated (Gy)	Difference	
				(Gy)	(%)
Brain	Minimum Dose	0.00	0.30	n/a	n/a
	Maximum Dose	24.80	23.61	1.19	5.0%
	Mean Dose	5.30	5.14	0.16	3.2%
PTV	Minimum Dose	16.60	16.49	0.11	0.7%
	Maximum Dose	28.90	27.54	1.04	4.7%
	Mean Dose	22.97	21.93	1.04	4.7%
GTV	Minimum Dose	21.90	21.94	-0.04	-0.2%
	Maximum Dose	30.37	30.26	0.11	0.4%
	Mean Dose	26.96	26.91	0.05	0.2%
Left eye	Minimum Dose	0.00	0.61	n/a	n/a
	Maximum Dose	7.20	5.75	1.45	25.2%
	Mean Dose	1.95	1.29	0.66	51.2%

Table 5.9: Corvus IMRT inverse-planned head phantom statistics.

The acronym n/a (not applicable) refers to cases when the measured MR dose is less than the minimum detectable dose.

This experiment showed an excellent GTV coverage, even in the case of misalignment in the treatment room. It is a perfect example of the usefulness of the PTV, which corresponds to the GTV with sufficient margins to account for patient positioning errors and organ motion.

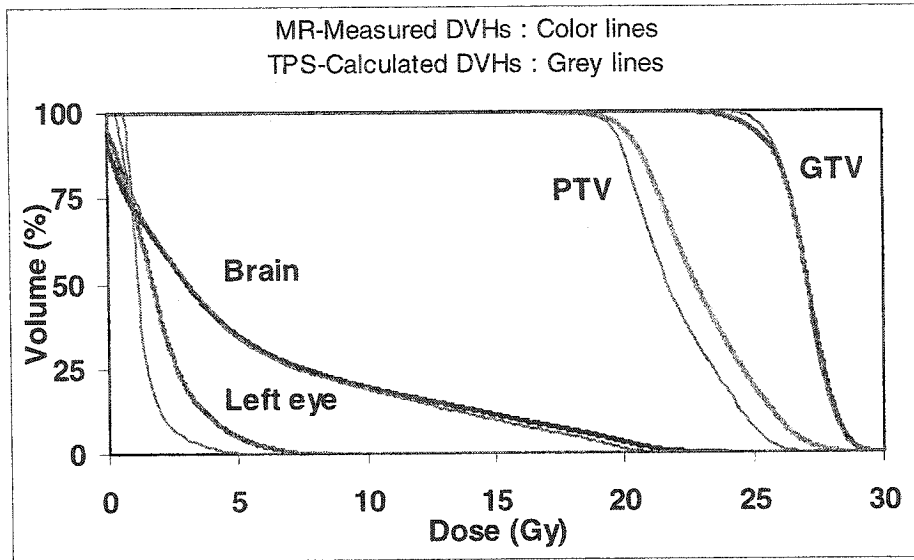


Figure 5.37: Corvus IMRT inverse-planned head phantom cumulative DVHs.

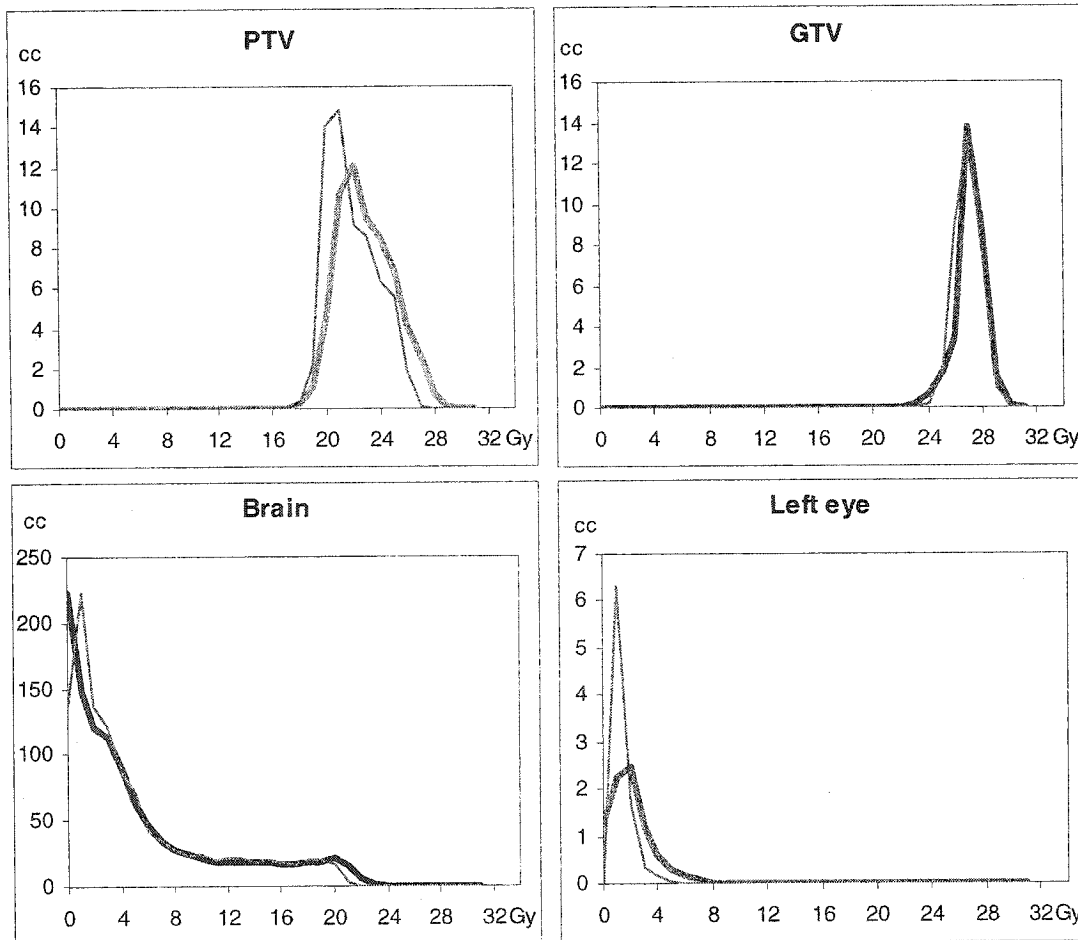


Figure 5.38: Corvus IMRT inverse-planned head phantom differential DVHs. The gel-measured DVHs are in thick color lines, while the TPS-calculated DVHs are represented by thin grey lines. The data was binned with one Gy increments.

Chapter Six

6 Conclusions

The goal of intensity modulated radiation therapy (IMRT) is to deliver a uniform dose to the tumor with minimal margins around the target, in order to increase local control of the disease while reducing secondary effects. The intensity modulations of the IMRT beams are obtained by the superposition of a large number of small fields. The difficulty of validating the dosimetry of these numerous small beams with steep dose gradients defines a need for an integrating, tissue-equivalent, high resolution, and anthropomorphic dosimeter. The use of a ferrous sulphate gel dosimeter in a patient specific quality assurance procedure resolves these issues.

The research performed in this thesis has shown the potential usefulness of the Fricke-gel dosimeter as a quality assurance tool to verify IMRT treatments produced by inverse treatment planning. First, the 3D integrating Fricke-gel dosimeter was successfully compared to an accepted dosimetric tool. It was then used to measure relative 3D dose distributions of simple treatment plans with multiple square or rectangular fields and specific inverse-planned IMRT treatment plans. By combining the CT anatomical information and the plan contours with the gel-measured data, it was possible to display the contours on the measured dose and the measured isodose lines on the CT, in addition to measuring dose-volume histograms (DVH) for the plans. This demonstrated the usefulness of the gel dosimeter as a quality assurance tool for IMRT and inverse planning.

The Fricke-gel dosimeter takes its name from the incorporation of a ferrous sulphate solution, similar to the well-known standard Fricke solution, into a gelatin matrix in order to preserve the spatial distribution of the radiation-induced transformations. The gel is prepared following the methods of Olsson⁵ and Hazle⁶, and is then poured into the selected phantom mold, which has water-equivalent plastic walls. The initial ferrous ions present in the gel and the radiation-induced ferric ions have different paramagnetic properties and so their concentrations influence the longitudinal relaxation constant (T_1) of the gel. Two sets of fast spin echo MR images of the gel with different T_1 weighting are acquired both prior to and after irradiation and the longitudinal relaxation rate (R_1) is calculated pixel by pixel. The background R_1 image is then subtracted from the post-irradiation R_1 image in order to remove magnetic field inhomogeneities.

The longitudinal relaxation rate (R_1) of the gel was shown to be linearly correlated to the irradiation dose in the 0 to 40 Gy dose range. R_1 measurements were reproducible within 2%, using a 95% confidence level. The uncertainty (after subtracting the background image) was less than 1 Gy at both 0 and 20 Gy. The minimum detectable dose (MDD) was on the order of 1 Gy. The system had a signal-to-noise ratio (SNR) of 82.

When PDD curves and off-axis ratios were acquired for an open beam and a 60° wedged beam, the gel dosimeter data demonstrated a good agreement, beyond the buildup region, to ion chamber measurements. For both beams, the mean difference was less than 2% for the PDDs and less than 1% for the profiles at depth. These results show the reliability of the gel dosimeter in measuring relative doses at depths greater than d_{max} . The results also fulfill the 2% or 2 mm ICRU-42⁴⁷ requirement for a quality assurance dosimeter.

The Fricke-gel dosimeter was then used to measure relative 3D dose distributions of typical simple plans and specific inverse-planned IMRT treatment plans. In order to create the treatment plan, the phantom was first scanned on a CT-simulator with fiducial markers determining the reference frame origin in the treatment planning system (TPS), which also corresponded to the target isocenter. The fiducial markers that appear on both the MR and CT images of the gel phantom were used to align the phantom in the linac treatment room

and to register the gel dose information with the TPS data set, which included the CT images, the contours and the calculated dose distribution. One set of data was then fused to the other, allowing the superposition of CT-defined contours on the gel dose image, and the superposition of the actual delivered dose (as measured by gel dosimetry) onto the CT anatomical information. The fused TPS contours and the gel dose distribution were used to generate dose-volume histograms (DVH) for the target, margins, structures "at risk" and whole body. These gel-measured DVHs were then compared to the DVHs computed by the treatment planning software. The mean, minimum and maximum doses for each contour were also calculated and compared to the TPS statistics.

Four experiments were used to illustrate the usefulness of the gel dosimeter in verifying 3D dose distributions. The first consisted of a forward-planned box phantom, which validated not only the dosimeter, but also the image fusion and the production of statistics and DVHs for the 3D volume. The positional accuracy after the image fusion was within 2 mm in x, y and z. All contours showed a mean dose difference less than 0.3 Gy, which corresponded to 1.5% of the prescription dose. The relative difference between the gel-measured and TPS-calculated mean doses were less than 0.5% difference at high dose and less than 10% at low dose regions. The cumulative and differential DVHs for both modalities compared very well.

The second forward-planned experiment more specifically validated the image fusion for the irregularly shaped head phantom. The image fusion produced very good results and the mean dose differences were less than 0.3 Gy (1.5% of the prescription dose) for all structures except the left eye, where it was less than 1 Gy. Both the cumulative and differential DVHs showed a very good agreement between the gel-measured and TPS-calculated dose distributions, except for the eyes and the cord, where there was none the less a general agreement in the differential DVHs.

The next two experiments involved inverse-planned IMRT dose distributions. One plan created a highly irregular dose distribution which was annular in shape and featured numerous spikes. There was an excellent qualitative agreement between the gel-measured and TPS-calculated dose distributions. There was a general correspondence between the

cumulative DVHs of the gel and the TPS, and a very good agreement for the differential DVHs. The lack of sharpness in the cumulative DVHs of the GTV and PTV and dose spreading in the differential DVHs may have been due to diffusion or slight misalignment of the phantom in the treatment position. Another possibility is that the delivery was not exactly as predicted by the TPS. The mean dose difference was less than 0.4 Gy (2% of the isocenter dose) for the PTV, GTV and External-margin contours and less than 1.5 Gy for the smaller cord and eyes structures. This experiment showed that the gel dosimeter is an adequate modality to measure and validate complex 3D IMRT dose distributions with irregularly shaped steep dose gradients.

The goal of the last experiment was to show the validity of this QA technique. It simulated all steps required to validate an actual IMRT case, using a probable treatment plan. It was assumed that the beam was delivered as planned, and no additional QA was performed on the beam prior to irradiation. Of course, plan dosimetry and delivery are checked beforehand for real patients. All gel and TPS statistics were within 5% of each other, except for the eye, located in the buildup region. For the GTV, the absolute dose differences for the minimum, maximum and mean were less than 0.2 Gy or 0.5%. The 1 Gy difference in the PTV mean dose was most probably caused by an alignment error at treatment time, but still provided excellent coverage of the GTV, as shown in the DVH graph. This experiment demonstrated the importance of the PTV concept, which ensures adequate coverage of the GTV by defining sufficient margins to account for patient positioning limitations and anatomical inter-treatment variations.

The analysis of the four 3D experiments demonstrated excellent agreement between the gel-measured and TPS-calculated dose distributions. Although the Fricke-gel system is sensitive to MR noise, the mean dose differences for the GTVs were lower than 0.3 Gy (1.6%) and lower than 1 Gy (5%) for all structures except for the small volume eye and cord structures. For doses between the MDD and 2 Gy, the mean dose differences were less than 10%, but within 0.25 Gy. All structures including the eyes and cord had a gel-measured mean dose within 1.45 Gy of their TPS-measured mean doses. Furthermore, all cumulative and differential dose-volume histograms showed a good to excellent comparison.

References

- 1 National Cancer Institute of Canada, "Canadian Cancer Statistics 2002", Toronto, Canada (2002).
- 2 J. C. Gore, Y. S. Kang, and R. J. Schulz, "Measurement of radiation dose distributions by nuclear magnetic resonance (NMR) imaging", *Physics in Medicine & Biology* **29** (10), 1189-97 (1984).
- 3 J. C. Gore, Y. S. Kang, and R. J. Schulz, "Measurement of radiation dose distributions by NMR imaging", *Magnetic Resonance Imaging* **2**, 244 (1984).
- 4 L. E. Olsson, S. Petersson, L. Ahlgren *et al.*, "Ferrous sulphate gels for determination of absorbed dose distributions using MRI technique: basic studies", *Physics in Medicine & Biology* **34** (1), 43-52 (1989).
- 5 L. E. Olsson, A. Fransson, A. Ericsson *et al.*, "MR imaging of absorbed dose distributions for radiotherapy using ferrous sulphate gels", *Physics in Medicine & Biology* **35** (12), 1623-31 (1990).
- 6 J. D. Hazle, L. Hefner, C. E. Nyerick *et al.*, "Dose-response characteristics of a ferrous-sulphate-doped gelatin system for determining radiation absorbed dose distributions by magnetic resonance imaging (Fe MRI)", *Physics in Medicine & Biology* **36** (8), 1117-25 (1991).
- 7 R. J. Schulz, A. F. deGuzman, D. B. Nguyen *et al.*, "Dose-response curves for Fricke-infused agarose gels as obtained by nuclear magnetic resonance", *Physics in Medicine & Biology* **35** (12), 1611-22 (1990).
- 8 B.M. Keller, "Characterization of the NMR based Fricke-gelatin radiation dosimeter", M.Sc. Thesis, McGill University (1994).
- 9 C. Duzenli, R. Sloboda, and D. Robinson, "A spin-spin relaxation rate investigation of the gelatin ferrous sulphate NMR dosimeter", *Physics in Medicine & Biology* **39**, 1577-92 (1994).
- 10 M. J. Maryanski, R.J. Schulz, G.S. Ibbott *et al.*, "Magnetic resonance imaging of radiation dose distributions using a polymer-gel dosimeter", *Physics in Medicine & Biology* **39**, 1437-55 (1994).
- 11 L. E. Olsson, B.A. Westrin, A. Fransson *et al.*, "Diffusion of ferric ions in agarose dosimeter gels", *Physics in Medicine & Biology* **37** (12), 2243-2252 (1992).
- 12 W.I.D. Rae, C.A. Willemsse, M.G. Lotter *et al.*, "Chelator effect on ion diffusion in ferrous-sulphate-doped gelatin gel dosimeters as analyzed by MRI", *Medical Physics* **23** (1), 15-23 (1996).
- 13 S. A. Back, P. Magnusson, L. E. Olsson *et al.*, "Verification of single beam treatment planning using a ferrous dosimeter gel and MRI (FeMRI)", *Acta Oncologica* **37** (6), 561-6 (1998).
- 14 M. F. Chan and K. Ayyangar, "Verification of water equivalence of FeMRI gels using Monte Carlo simulation", *Medical Physics* **22** (4), 475-8 (1995).
- 15 T. Kron, P. Metcalfe, and J. M. Pope, "Investigation of the tissue equivalence of gels used for NMR dosimetry", *Physics in Medicine & Biology* **38** (1), 139-50 (1993).
- 16 S. Olberg, A. Skretting, O. Bruland *et al.*, "Dose distribution measurements by MRI of a phantom containing lung tissue equivalent compartments made of ferrous sulphate gel", *Physics in Medicine & Biology* **45** (10), 2761-70 (2000).
- 17 W.A. Parker, "Brachytherapy Dosimetry with Fricke-gelatin and MRI", M.Sc., McGill University (1994).
- 18 M. Oldham, M. McJury, I. B. Baustert *et al.*, "Improving calibration accuracy in gel dosimetry", *Physics in Medicine & Biology* **43** (10), 2709-20 (1998).

- 19 M. J. Maryanski, J. C. Gore, R. P. Kennan *et al.*, "NMR relaxation enhancement in gels polymerized and cross-linked by ionizing radiation: a new approach to 3D dosimetry by MRI", *Magnetic Resonance Imaging* **11** (2), 253-8 (1993).
- 20 K. C. Chu, K. J. Jordan, J. J. Battista *et al.*, "Polyvinyl alcohol-Fricke hydrogel and cryogel: two new gel dosimetry systems with low Fe³⁺ diffusion", *Physics in Medicine & Biology* **45** (4), 955-69 (2000).
- 21 M. Bengtsson, T. Furre, J. Rodal *et al.*, "Measurement of dynamic wedge angles and beam profiles by means of MRI ferrous sulphate gel dosimetry", *Physics in Medicine & Biology* **41** (2), 269-77 (1996).
- 22 W. Y. Guo, W. C. Chu, M. C. Wu *et al.*, "An evaluation of the accuracy of magnetic-resonance-guided Gamma Knife surgery", *Stereotactic & Functional Neurosurgery* **66** (Suppl 1), 85-92 (1996).
- 23 B. H. Knutsen, A. Skretting, T. P. Hellebust *et al.*, "Determination of 3D dose distribution from intracavitary brachytherapy of cervical cancer by MRI of irradiated ferrous sulphate gel", *Radiotherapy & Oncology* **43** (2), 219-27 (1997).
- 24 M. McJury, P. D. Tapper, V. P. Cosgrove *et al.*, "Experimental 3D dosimetry around a high-dose-rate clinical ¹⁹²Ir source using a polyacrylamide gel (PAG) dosimeter", *Physics in Medicine & Biology* **44** (10), 2431-44 (1999).
- 25 M. F. Chan and K. M. Ayyangar, "Confirmation of target localization and dosimetry for 3D conformal radiotherapy treatment planning by MR imaging of a ferrous sulfate gel head phantom", *Medical Physics* **22** (7), 1171-5 (1995).
- 26 S. A. Johansson, P. Magnusson, A. Fransson *et al.*, "Dosimeter gel and MR imaging for verification of calculated dose distributions in clinical radiation therapy", *Acta Oncologica* **36** (3), 283-90 (1997).
- 27 A.L. Boyer, L. Xing, and P. Xia, "Beam Shaping and Intensity Modulation", in *The Modern Technology of Radiation Oncology*, edited by Jacob Van Dyk, Medical Physics Publishing, Madison, WI, USA, pp. 437-479 (1999).
- 28 ICRU, Report No. 50, "Prescribing, recording and reporting photon beam therapy" (1993).
- 29 R. Mohan, S.A. Leibel, D. Pizzuto *et al.*, "Three-dimensional Conformal Radiotherapy", in *Treatment Planning in Radiation Oncology*, edited by F. Khan and R.A. Potish, Williams & Wilkins, Baltimore, MD, pp. 147-186 (1998).
- 30 L.J. Verhey, "3D Conformal Planning for Linacs", presented at the 41st Annual Meeting of the American Society for Therapeutic Radiology and Oncology, unpublished (1999).
- 31 R. Mohan, "Intensity Modulated Radiation Therapy - Part I: Planning and Delivery", presented at the 42nd Annual Scientific Meeting of the American Society for Therapeutic Radiology and Radiation Oncology, Boston, MA, USA, unpublished (2000).
- 32 W. De Neve, "Clinical IMRT Planning Using a Mixture of Forward and Inverse Elements", presented at the 41st Annual Meeting of the American Society for Therapeutic Radiology and Oncology, unpublished (1999).
- 33 E. S. Sternick, M. P. Carol, and W. III Grant, "Intensity-modulated Radiotherapy", in *Treatment Planning in Radiation Oncology*, edited by F. Khan and R.A. Potish, Williams & Wilkins, Baltimore, MD, pp. 187-213 (1998).
- 34 J. Van Dyke, "Quality Assurance", in *Treatment Planning in Radiation Oncology*, edited by F. Khan and R.A. Potish, Williams & Wilkins, Baltimore, MD, pp. 123-146 (1998).
- 35 F.H. Attix, *Introduction to Radiological Physics and Radiation Dosimetry*, John Wiley & Sons, New York (1986).
- 36 M. Burton, "Radiation Chemistry", *J. Phys. Colloid Chem.* **51**, 611 (1947).

- 37 H. Fricke and S. Morse, "The chemical action of roentgen rays on dilute ferrosulphate solutions as a measure of dose", *Am. J. Roentgenol. Radium Therapy Nucl. Med* **18**, 430-432 (1927).
- 38 T.J. Hardwick, "The oxidation of ferrous sulphate solutions by g-rays - the absolute yield", *Can. J. Chem.* **30**, 17-22 (1952).
- 39 M. B. Podgorsak and L. J. Schreiner, "Nuclear magnetic relaxation characterization of irradiated Fricke solution", *Medical Physics* **19** (1), 87-95 (1992).
- 40 H. Fricke and J. Hart, "Chemical Dosimetry", in *Radiation Dosimetry Vol. II: Instrumentation*, edited by H. Attix, W. Roesch, and E. Tochilin, Academic Press, London, pp. 167-239 (1966).
- 41 T. Kron, "Dose Measuring Tools", in *The Modern Technology of Radiation Oncology*, edited by Jacob Van Dyk, Medical Physics Publishing, Madison, WN, USA, pp. 753-821 (1999).
- 42 ICRU, Report No. 42, "Use of computers in external beam radiotherapy procedures with high-energy photons and electrons" (1987).
- 43 S. A. Back, P. Magnusson, A. Fransson *et al.*, "Improvements in absorbed dose measurements for external radiation therapy using ferrous dosimeter gel and MR imaging (FeMRI)", *Physics in Medicine & Biology* **43**, 261-76 (1998).
- 44 ICRU, Report No. 22, "Measurement of low-level activity" (1972).
- 45 B. Reichl, D. Matthaei, J. Richter *et al.*, "An automated fast MR-imaging method for localized measurements of dose distributions using NMR-Fricke gel dosimetry. Evaluation of influences on the measurement accuracy", *Strahlentherapie und Onkologie* **172** (6), 312-9 (1996).
- 46 F. M. Khan, *The physics of radiation therapy*, 2nd ed., Williams & Wilkins, Baltimore, MD (1994).
- 47 American Association of Physicists in Medicine Radiation Therapy Task Group 21, "A protocol for determination of absorbed dose from high-energy photon and electron beams", *Medical Physics* **10** (6), 41- 771 (1983).
- 48 A. Abragam, *The Principles of Nuclear Magnetism*, Oxford University Press, London (1961).
- 49 F. Bloch, W. W. Hansen, and M. E. Packard, "Nuclear induction", *Phys. Rev.* **69**, 127 (1946).
- 50 E. M. Purcell, H. C. Torrey, and R. V. Pound, "Resonance absorption by nuclear magnetic moments in a solid", *Phys. Rev.* **69**, 37-38 (1946).
- 51 T.M. Shaw and R.H. Elsken, "Determination of water by nuclear magnetic resonance absorption in potato and apple tissue", *J. Agr. Food Chem.* **4**, 162-164 (1956).
- 52 E. Odeblad, N. B. Bhar, and G. Lindstrom, "Proton magnetic resonance of human red blood cells in heavy water exchange experiments", *Arch. Biochem. Biophys.* **63**, 221-225 (1956).
- 53 R. Damadian, "Apparatus and method for detecting cancer in tissue", Patent no. 3789832, United States (March 17, 1972).
- 54 P.C. Lauterbur, "Image formation by induced local interactions: examples employing nuclear magnetic resonance", *Nature* **242**, 190-191 (1973).
- 55 P. Mansfield and P. K. Grannell, "NMR diffraction in solids", *J. Phys. C: Solid State Phys.* **6**, L422-6 (1973).
- 56 P. Mansfield and A.A. Maudsley, "Planar and line scan spin imaging by NMR", presented at the Magnetic Resonance and Related Phenomena, unpublished (1976).
- 57 R. Damadian, M. Goldsmith, and L. Minkoff, "NMR in cancer: XVI, FONAR image of the live juman body", *Physiol. Chem. Phys.* **9**, 97-100 (1977).

- 58 R.C. Hawkes, G.N. Holland, W.S. Moore *et al.*, "NMR tomography of the brain: a preliminary clinical assessment with demonstration of pathology", *J. Comput. Assist. Tomogr.* **4** (5), 577-86 (1980).
- 59 P. Keller, *Basic Principles of MR Imaging*, GE Medical Systems, Milwaukee, WI (1988).
- 60 M.A. Foster, *Magnetic Resonance in Medicine and Biology*, Pergamon Press, New York, NY (1984).
- 61 D.G. Gadian, *Nuclear magnetic resonance and its applications to living systems*, Oxford University Press, New York (1982).
- 62 M.O. Leach, "Spatially localised nuclear magnetic resonance", in *The Physics of Medical Imaging*, edited by S. Webb, IOP Publishing Ltd, Bristol, England, pp. 389-487 (1988).
- 63 D.G. Nishimura, *Principles of Magnetic Resonance Imaging*, Department of Electrical Engineering, Stanford University (1996).
- 64 L. Wald, "MRI Physics II, Functional Magnetic Resonance Imaging: Data Acquisition and Analysis (HST-583)", MIT & MGH-NMR Center (2001).
- 65 J.P. Hornak, "The Basics of MRI", Center for Imaging Science, Rochester Institute of Technology, Rochester, NY <http://www.cis.rit.edu/htbooks/mri/> (2002).
- 66 H-J. Smith, *A non-mathematical approach to basic MRI*, Medical Physics Publishing Corporation, Madison, Wisconsin (1989).
- 67 P. Magnusson, S. A. Back, and L. E. Olsson, "MRI image plane nonuniformity in evaluation of ferrous sulphate dosimeter gel (FeGel) by means of T1-relaxation time", *Magnetic Resonance Imaging* **17** (9), 1357-70 (1999).
- 68 Y. Bercier, "Image fusion for radiosurgery of arteriovenous malformations", Ph.D. Thesis, McGill University (2002).
- 69 P. Bélanger, "MR based Fricke-gelatin dosimetry: Uncertainty evaluation and computerised analysis of measured dose distributions", M.Sc. Thesis, McGill University (2001).
- 70 American Association of Physicists in Medicine Radiation Therapy Task Group 51, "The AAPM's TG-51 protocol for clinical reference dosimetry of high-energy beams", *Medical Physics* **26** (9), 1847 - 1870 (1999).
- 71 Varian Medical Systems, *CadPlan 6.2.7 External Beam Modelling Physics*, Palo Alto, CA (1999).